Understanding the optoelectronic properties of lead-tin perovskites through experiment and simulation



Florine M. Rombach

Worcester College

University of Oxford

A thesis submitted for the degree of

Doctor of Philosophy

Trinity 2024

Acknowledgements

The completion of this thesis would not have been possible without significant and enduring support from colleagues, friends and family.

I would first like to thank Prof. Henry Snaith for giving me the opportunity to complete this work, and for allowing me to continuously choose its direction. I feel lucky to have had a supervisor who supports such free development of one's personal research interests. He also assembled the excellent group of researchers I have worked alongside, whose comradery made work both entertaining and a place to belong. I look forward to seeing the great things each of them will go on to accomplish.

I would like to thank my collaborators from all over the world, who have directly contributed to this thesis. James, Joel and Shuaifeng, who answered endless questions. Silvia and Daniele, who significantly improved my understanding of defects and their working. Heon, Akash, Jake, Nicky, Xinyi, for doubling motivation and halving shared pain. I feel particularly lucky to have had Heon on my side when battling lead-tin, and Akash when battling python. I want to make out special thanks to Manuel, who not only endlessly discussed fitting with me but also proof-read large parts of this thesis. And of course I would like to thank Clare, who can make people feel calm and pleasant no matter what sort of day they are having.

I am grateful to friends near and far for enquiring about the process of this thesis just enough, and for reminding me of the other joys in life. I thank my mom, dad and sister for their love, unconditional encouragement of my interests, and the care packages from home. Finally, I thank Davis for his infinite support and care.

Abstract

This thesis makes contributions to the understanding of lead-tin perovskite materials, aiming to advance both the fundamental knowledge of their material properties and their potential for use in stable, efficient solar cells. This work addresses key challenges related to material degradation, impurity effects, and the interpretation of photoluminescence measurements, through the integration of experimental characterization with theoretical modelling.

In Chapter 4, the effects of several degradation mechanisms on the performance of lead-tin perovskite solar cells during aging are quantified. This reveals that the commonly used poly(3,4-ethylenedioxythiophene) polystyrene sulfonate (PEDOT:PSS) hole transport layer (HTL) accelerates performance degradation by amplifying mobile-ion-induced field screening during aging. A second, slower degradation pathway is linked to p-doping of the perovskite during aging, which is only exposed when PEDOT:PSS is replaced by an alternative HTL. Longer-term characterization reveals the much slower segregation of a $CsSnI_3$ phase. This deconvolution of degradation mechanisms provides a clear roadmap for improving the stability of lead-tin perovskite solar cells.

Chapter 5 explores the impact of small concentrations of bismuth (Bi^{3+}) and antimony (Sb^{3+}) impurities on the atomic-level defect chemistry of lead-tin perovskites. Films doped with even trace levels of these ions show greatly increased non-radiative recombination. Such behaviour is rationalized by photoluminescence (PL) and density functional theory (DFT) simulations, which suggest that these metal ions introduce deep, recombination-active traps when incorporated into the perovskite lattice. This chapter also suggests and demonstrates a practical pathway for precursor purification to enhance material quality.

In Chapter 6, a novel approach to the extraction of relevant material parameters from PL characterization data is introduced. Bayesian inference and nested sampling are used to

quantitatively compare recombination models for the interpretation of time-resolved photoluminescence (TRPL) and photoluminescence quantum efficiency (PLQE) data. This method identifies the most appropriate model for the dataset and simultaneously extracts critical recombination parameters from it. The proof of concept presented in this chapter demonstrates the importance of rigorous model evaluation when analysing new material systems.

Overall, the results presented in this thesis demonstrates the value of combining a wide range of characterization methods with physical simulations for the investigation of novel materials. This enables a deeper understanding of degradation mechanisms, impurity effects, and recombination behaviour in lead-tin perovskites, all of which are crucial for advancing their stability and performance in solar cells. The findings of this research contribute to the ongoing development of all-perovskite multi-junction photovoltaics.

List of Publications

(1)
Rombach, F. M.; Dasgupta, A.; Kober-Czerny, M.; Jin, H.; Ball, J.; Smith, J.; Farrar, M.; Snaith, H. Disentangling degradation pathways of narrow bandgap lead-tin perovskite material and photovoltaic devices. *Nat. Commun*. **2025**, 16, 5450.

(2)
Rombach, F. M.; Gregori, L.; Sidler, A.; Whitworth, J.; Zeiske, S.; Jin, H.; Hung, E.; Motti, S.; Caprioglio, P.; Armin, A.; Lenz, M.; Meggiolaro, D.; De Angelis, F.; Snaith, H. J. Effects of Bi and Sb ion incorporation on the optoelectronic properties of mixed lead–tin perovskites. *J. Mater. Chem. C* **2025**, 13, 5161-5171.

(3)
Dong, Y.; **Rombach, F. M.**; Min, G.; Snaith, H. J.; Lin, C-T.; Haque, S. A.; Macdonald, T. J. Dopant-induced interactions in spiro-OMeTAD: Advancing hole transport for perovskite solar cells. *Materials Science and Engineering: R: Reports* **2025,** 162, 100875.

(4)
Hu, S.; Wang, J.; Zhao, P.; Pascual, J.; Wang, J.; **Rombach, F. M.**; Dasgupta, A.; Liu, W.; Truong, M. A.; Zhu, H.; Kober-Czerny, M.; Drysdale, J. N.; Smith, J. A.; Yuan, Z.; Aalbers, G. J. W.; Schipper, N. R. M.; Yao, J.; Nakano, K.; Turren-Cruz, S.-H.; Dallmann, A.; Christoforo, M. G.; Ball, J. M.; McMeekin, D. P.; Zaininger, K.-A.; Liu, Z.; Noel, N. K.; Tajima, K.; Chen, W.; Ehara, M.; Janssen, R. A. J.; Wakamiya, A.; Snaith, H. J.. Steering perovskite precursor solutions for multijunction photovoltaics. *Nature* **2024**, 639, 93–101.

(5)
Kober-Czerny, M.; Dasgupta, A.; Seo, S.; **Rombach, F. M.**; McMeekin, D. P.; Jin, H.; Snaith, H. J. Determining Parameters of Metal-Halide Perovskites Using Photoluminescence with Bayesian Inference. *PRX Energy* **2025**, *4* (1), 013001.

(6)
Jin, H.; Farrar, M. D.; Ball, J. M.; Dasgupta, A.; Caprioglio, P.; Narayanan, S.; Oliver, R. D. J.; **Rombach, F. M**.; Putland, B. W. J.; Johnston, M. B.; Snaith, H. J. Alumina Nanoparticle Interfacial Buffer Layer for Low-Bandgap Lead-Tin Perovskite Solar Cells. *Adv Funct Materials* **2023**, *33* (35), 2303012.

(7)
Rombach, F. **M**.; Haque, S. A.; Macdonald, T. J. Lessons Learned from Spiro-OMeTAD and PTAA in Perovskite Solar Cells. *Energy Environ. Sci.* **2021**, *14* (10), 5161–5190.

List of Abbreviations

BCP	bathocuproine
BF	Bayes Factor
CB	conduction band
CBM	conduction band minimum
CTL	charge transport layer
DFT	density functional theory
DMF	N,N-dimethylformamide
DMSO	dimethyl sulfoxide
EDA	ethylenediammonium
EDX	energy-dispersive X-ray spectroscopy
E_F	Fermi level
EQE	external quantum efficiency
ETL	electron transport layer
FA	formamidinium
FET	field effect transistor
FF	fill factor
FWHM	full width at half maximum
HOMO	highest occupied molecular orbital
HTL	hole transport layer
ICP-MS	Inductively coupled plasma mass spectrometry
IPA	isopropyl alcohol
ISOS	International Summit on Organic PV stability
ITO	indium tin oxide
J-V	current density-voltage
KS	Kohn-Sham
LM	Levenberg-Marquadt
LUMO	lowest unoccupied molecular orbital
MA	methylammonium
MCMC	Markov chain Monte Carlo
MHP	metal halide perovskite
MPP	maximum power point

MPPT	maximum power point tracking
MSE	mean square error
NIR	near-infrared
NP	nanoparticles
ODE	ordinary differential equation
OM	optical microscope
PBE	Perdew-Burke-Ernzherof
PCBM	phenyl-C61-butyric acid methyl ester
PCE	power conversion efficiency
PEDOT:PSS	poly(3,4-ethylenedioxythiophene) polystyrene sulfonate
PL	photoluminescence
PLQE	photoluminescence quantum efficiency
PSC	perovskite solar cell
PTAA	poly(bis(4-phenyl)(2,4,6-trimethylphenyl)amine)
PV	photovoltaic
QFLS	quasi-Fermi level splitting
SEM	secondary electron microscope
SHGO	simplicial homology global optimization
SOC	spin-orbit coupling
SRV	surface recombination velocity
TAS	transient absorption
TCSPC	time-correlated single photon counting
TPC	time-resolved photoconductivity
TRMC	time-resolved microwave conductivity
TRPL	time-resolved photoluminescence
VB	valence band
VBM	valence band maximum
XRD	X-ray diffraction

Table of Contents

1 INTRODUCTION 6

2 BACKGROUND 10

2.1 Photovoltaic materials & devices 10

2.2 Stability of perovskite materials 14

2.3 Doping perovskite materials 21

2.4 Modelling recombination in perovskite materials 26

2.5 Works cited 36

3 METHODS 44

3.1 Sample fabrication 44

3.2 Photovoltaic device characterization 48

3.3 Structural & chemical material characterization 50

3.4 Optical & electronic material characterization 53

3.5 Simulations & Fitting 57

3.6 Works Cited 62

4 STABILITY OF LEAD-TIN PEROVSKITES 64

4.1 Overview 64

4.2 Structural and morphological changes during aging 65

4.3 Opto-electronic changes during aging 72

4.4 Device performance 84

4.5 Impact of mobile ions on device performance during aging 89

4.6 Impact of electronic changes on device performance during aging 103

4.7 Conclusion & outlook on lead-tin perovskite stability 108

4.8 Works cited 111

5 EXTRINSIC DOPING OF LEAD-TIN PEROVSKITES 115

5.1 Overview 115

5.2 Optoelectronic quality of Bi^{3+} and Sb^{3+}-doped lead-tin perovskite films 117

5.3 DFT & PL simulations 122

5.4 Bi^{3+} impurities in perovskite precursor chemicals 133

5.5 Conclusion & outlook on perovskite doping 137

5.6 Works cited 138

6 MODELLING RECOMBINATION IN LEAD-TIN PEROVSKITES 140

6.1 Overview 140

6.2 Current state of PL measurement interpretation 141

6.3 PLQE & TRPL simulations 145

6.4 Bayesian Inference & Model Selection 155

6.5 Conclusion & outlook on modelling recombination in perovskites 160

6.6 Works Cited 161

7 OUTLOOK 164

8 APPENDIX 166

A.1 Material parameters used for simulations 166

1 Introduction

In an era of rapid population growth and expanding economies, global energy demand is projected to double by 2050.[1] Concurrently, however, the escalating impacts of global warming on both human security and global ecosystems necessitate an urgent reduction in carbon dioxide emissions.[2] Solar energy presents a promising solution, as the amount of sunlight reaching Earth in a single hour contains more energy than humanity consumes in an entire year.[3] This abundance has spurred worldwide research into photovoltaic (PV) energy conversion technologies.

The photovoltaic effect—the ability of materials to convert light into electricity—was first discovered in 1839 by Edmond Becquerel. He immersed plates of platinum in an acidic electrolyte and upon illuminating them, detected the generation of electricity.[4] Decades later, C. Fritts created the first solid-state thin-film photovoltaic device by depositing layers of selenium and gold on a metal plate, finding that illumination of this device produced a current.[5] These discoveries laid the foundation for the diverse range of photovoltaic devices in use today. The capacity to rapidly and cost-effectively expand solar power generation will be crucial for a successful global transition to renewable energy sources.[6]

Over the last decades, crystalline silicon (c-Si) solar cells have dominated the PV market. Although the cost of electricity production from c-Si declined by 76% between 2010-2018, fossil fuels still account for over 70% of global electricity generation.[3] To make solar power economically attractive and accelerate the transition to renewable energy, further improvements in efficiency to reduce balance of system costs are crucial. While c-Si PV remains the most cost-effective method for solar electricity production, these modules are approaching their theoretical maximum efficiency. Recent years have seen only minor improvements,[7] and their fabrication is based on non-trivial, high-temperature processes.[8]

In the last ten years, perovskite solar cells (PSCs) have emerged as a new type of third-generation solar cell, whose fabrication is low-cost, solution processed, compatible with flexible materials and has the potential to achieve higher efficiencies than c-Si solar cells. These organic-inorganic metal halide perovskites (MHPs) have an ABX_3 composition, where A^+ is a large organic cation such as methylammonium (MA) or formamidinium (FA), B^{2+} is an inorganic cation such as Pb^{2+} or Sn^{2+}, and X^- is a halide ion such as I^- (shown in Figure 1.1). The first PSC was constructed in 2009 by Kojima et al,[9] who replaced the dye in a typical dye-sensitized solar cell architecture[10] with the perovskite absorber methylammonium lead iodide ($MAPbI_3$).

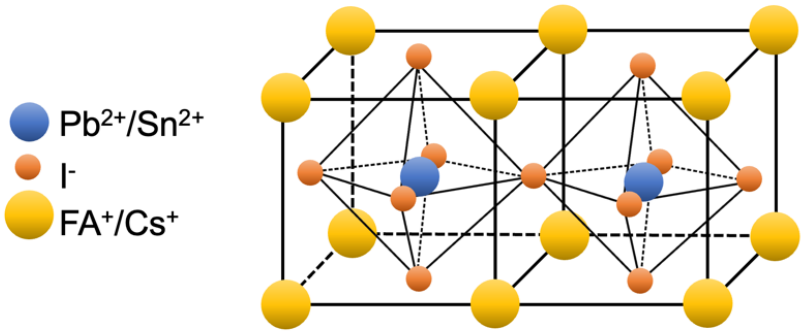


Figure 1.1. Diagram of the structure of the hybrid organic-inorganic 3D cubic perovskite used in this thesis.

Moving from a liquid electrolyte to a solid-state hole conductor later raised efficiencies from 3.8 % to 9.7 %, simultaneously resulting in greatly improved solar cell stability.[511] The demonstration that perovskite had a high absorption coefficient,[12,13] could independently conduct both electrons[14] and holes[15], and showed exceptionally long electron and hole diffusion lengths[16,17] as well as spontaneous exciton dissociation[18] set the pace for the next decade of PSC research. These early fundamental studies enabled the further exploration of both mesoporous[19] and planar[20,21] device architectures, as well as novel processing techniques enabling higher quality perovskite films.[22,23,24]

One of the most promising aspects of perovskites is their highly tuneable bandgap, which can be adjusted by varying the material composition.[25] This tunability enables the development of perovskites with bandgaps well-suited for multi-junction architectures. All-perovskite multijunction solar cells have emerged as a promising technology due to their potential for high efficiencies (feasibly 33.8% for double junctions or 36.6% for triple junctions),[26] ease of processing, and promise of lower embodied energy in manufacturing as compared to silicon-based single-junction or tandem cells.[27]

The lowest bandgap (~1.25 eV) perovskites can be achieved by alloying Pb and Sn,[28,29] making lead-tin perovskites an ideal material for the low energy absorber in such tandems. Consequently, the development of efficient, reproducible, and stable lead-tin perovskite absorber layers and device stacks is essential for the realization of field-deployable all-perovskite tandems. Efficiencies of lead-tin perovskite-based devices now exceed 23% in single junction devices,[30] 28.5% in all-perovskite double junctions,[31] and 24.3% in triple junctions.[32] Despite the rapid progress in improving device efficiencies that has been made in this field, several challenges remain to be addressed to both complete scientific understanding of MHP materials and realize commercial adoption of PSCs. One of the primary concerns is the long-term stability of perovskite materials, which are susceptible to degradation under operating conditions. Another is understanding challenges related to the reproducibility of the perovskite absorber. Finally, the dominant physical mechanisms governing the behaviour of charge carriers with perovskite films and devices are not yet fully understood, which can make the interpretation of opto-electronic measurements challenging.

This thesis focuses on understanding the properties of narrow bandgap lead-tin perovskites with respect to these challenges. **Chapter 2** provides an overview of the current understanding of the degradation, doping and recombination dynamics in MHP and in lead-tin perovskites specifically. **Chapter 3** explains the experimental and simulation methods

used. **Chapter 4** investigates the causes of the rapid degradation of lead-tin PSCs under light and heat stressing. It is revealed that an increasing impact of the bias-induced accumulation of rapid-moving ions is the major cause of early-time performance degradation for devices using poly(3,4-ethylenedioxythiophene) polystyrene sulfonate (PEDOT:PSS). Crucially, the dominant degradation modes are observed to vary strongly when a different HTL is used and ascribe this to a difference in iodine vacancy generation rate. Quantifying the impact of these changes on device performance defines a clear direction for future stability improvements. **Chapter 5** explores the effect of Bi^{3+} and Sb^{3+} doping in lead-tin perovskites. Films doped with small amounts of BiI_3 and SbI_3 show greatly increased non-radiative recombination at very low precursor doping. Such behaviour is rationalized by simulations, showing that these metal ions can be incorporated in the perovskite crystal by introducing deep trap levels in the band gap. In response, a facile method for removing Bi^{3+} impurities from a perovskite ink is introduced. **Chapter 6** critically evaluates the interpretation of photoluminescence (PL) data in the perovskite field. Simulations are used to demonstrate that existing models used to extract recombination parameters from these measurements are not sufficient. Such inappropriate models may still produce good fits to the data and is hence not easily noticeable without explicit statistical model comparison. Bayes factors are calculated for each model, and these are used to identify the model most suitable to for the lead-tin perovskite samples investigated. **Chapter 7** summarizes the results and provides an outlook on future research directions.

2 Background

2.1 Photovoltaic materials & devices

Photovoltaic effect and devices

Figure 2.1 illustrates the basic steps involved in the functioning of photovoltaic devices. When light is incident upon a solid-state photoactive semiconductor, electrons are excited from their ground state in the valence band (VB) to the conduction band (CB), leaving behind a net positive charge, which is referred to as a 'hole' in the VB. Initially, the electron and hole exist as a bound pair referred to as an 'exciton', which is dissociated to free charge carriers if the 'exciton binding energy' is overcome. To produce a current, the resulting free charge carriers must then be extracted at electrodes on opposing sides of the photovoltaic device. Different solar cell architectures have different approaches to the optimization of these charge generation, separation and extraction processes, depending on the properties of the light absorbing material.

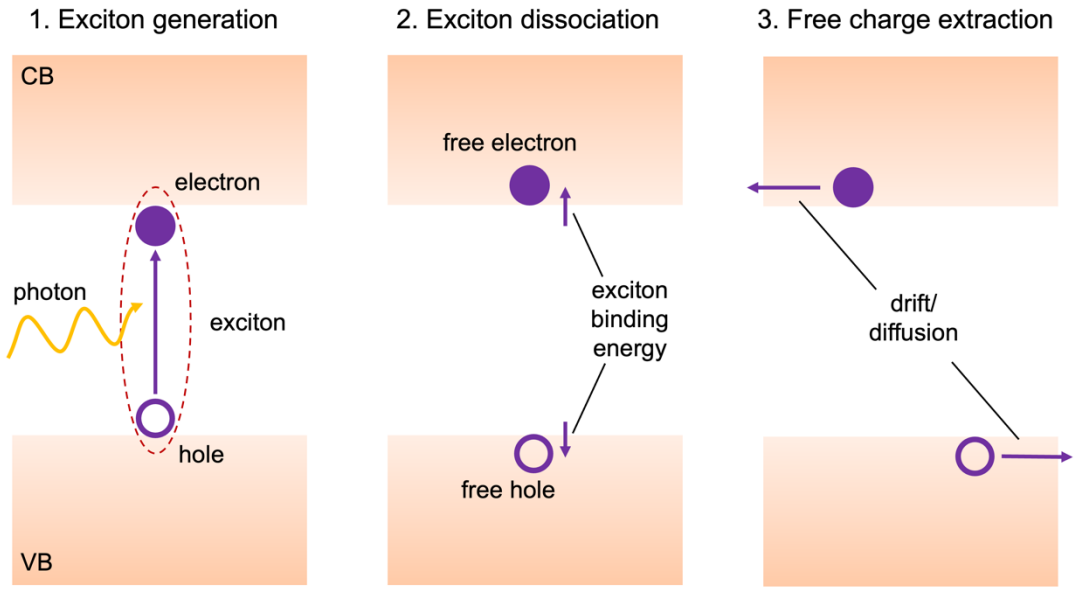


Figure 2.1. Diagram showing processes of excitation generation, dissociation and free charge extraction in a photovoltaic semiconductor.

Incident light with a lower energy than the absorber material's bandgap is not absorbed, whilst electrons excited by incident light with a higher energy than the bandgap thermalize to the CB edge before being extracted. Energy is hence lost from both below- and above-bandgap illumination in the solar spectrum. A theoretically more efficient solar cell can be made by stacking absorbers with multiple different bandgaps as shown in Figure 2.2, to make a multi-junction solar cell. The maximum theoretical power conversion efficiency (PCE) based on the detailed balance limit of a photovoltaic device using a single absorber is 33.7%,[33] but is increased to 68.7% for a device with an infinite number of absorber layers with continuously narrowing bandgaps.[34]

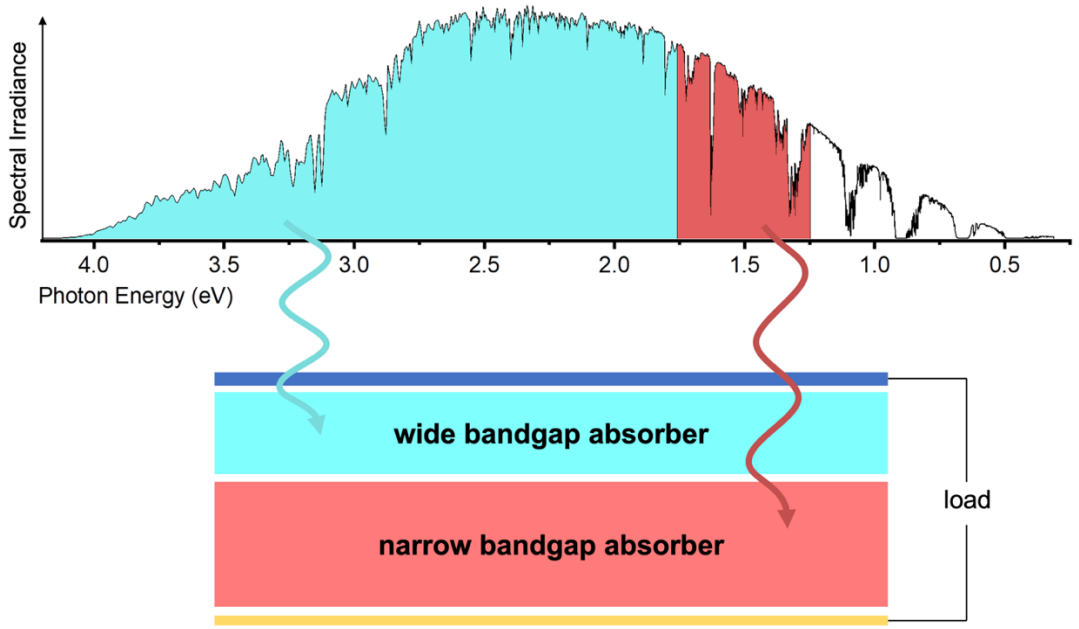


Figure 2.2. Plot of AM1.5 solar irradiation spectrum and diagram of all-perovskite tandem solar cell, illustrating portion of solar irradiation spectrum absorbed by each subcell.

Metal halide perovskite solar cells

MHPs are an emergent class of photovoltaic materials.[9,35] In their photoactive cubic phase, most MHPs have been measured to have exciton binding energies below the thermal energy (approx. 26 meV), which means that excitons are spontaneously dissociated into free charge carriers at operating temperatures.[36] Charge generation in these materials is benefitted by a high absorption coefficient.[12] Additionally, the bandgap of this family of perovskite materials is highly tuneable by varying the material composition,[25] enabling the development of perovskites with bandgaps ranging from 1.2 eV – 2 eV.

Another property which distinguishes perovskites from conventional semiconductors is that they can be processed by low-energy methods (such as solution processing) and still maintain long charge carrier diffusion lengths.[37] Whether this property can be ascribed to low defect densities or the low recombination-activity of defects remains an open discussion in the field.[38] Much of the work on perovskite solar cells in the past decade has focused on further reducing of non-radiative recombination rates, both in the perovskite bulk and at interfaces in a photovoltaic device.[39]

Unlike many conventional semiconductors, most MHP are considered intrinsic materials with low background electron and hole densities. Photogenerated charges are hence separated by a n-i-p or p-i-n device architecture (shown in Figure 2.3), in which the perovskite absorber is layered in between thin layers of a n-type (the electron transport layer or ETL) and a p-type material (the hole transport layer or HTL). Electrically connecting the electrodes creates an electric field across the absorber layer, which causes free charge carriers to drift towards opposite sides to be collected at the electrodes. The alignment of the CB/VB of the perovskite with the highest occupied molecular orbital (HOMO) of the HTL and lowest unoccupied molecular orbital (LUMO) of the ETL must be carefully tuned to both maximize the built-in voltage of the device and ensure rapid free charge carrier transfer into the charge

transport layers (CTLs). In addition to this, both CTLs must be sufficiently conductive and cause minimal recombination of the opposite charge carrier at the perovskite/CTL interface. Finally, the entirety of the MHP solar cell architecture should cause minimal parasitic light absorption to ensure a high charge carrier generation and hence a high current can be reached.

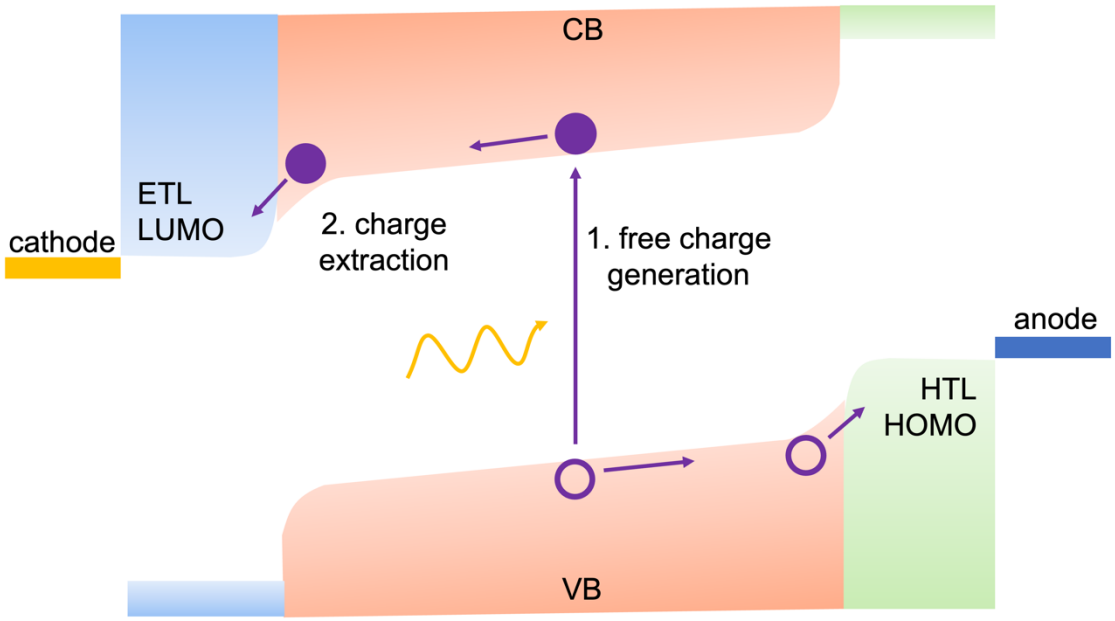


Figure 2.3. Diagram of band alignment in a p-i-n perovskite solar cell during transient operation, showing free charge carrier generation and extraction.

The bandgap tuneability of perovskites makes them especially useful for applications in multi-junction photovoltaic devices. Whilst perovskites can be used to create multi-junction devices when combined with established photovoltaic materials such as silicon, so called 'all-perovskite' tandem solar cells are especially attractive due to their promise of lower embodied energy in manufacturing as compared to silicon-based single-junction or tandem cells,[27] and conservative estimate of maximum reachable efficiencies are 33.8% for double junctions or 36.6% for triple junctions.[26] Current record efficiencies are 28.5% in all-perovskite double junctions,[31] and 24.3% in triple junctions.[32]

Narrow bandgap lead-tin perovskites

One way in which the perovskite bandgap can be tuned is by partially replacing Pb with Sn at the B-site of the perovskite structure. A substitution ratio of 50-60% Sn results in the narrowest bandgap of ~1.25 eV, an ideal bandgap to form a double junction with a ~1.75 eV wide bandgap perovskite. Throughout this thesis, 'lead-tin perovskite' is used to refer to the 50:50 lead:tin composition. As the only perovskite composition to achieve a bandgap this narrow, lead-tin perovskites are essential to achieving efficient all-perovskite multi-junction solar cells. The first single-junction 50:50 lead-tin perovskite device in 2014 had an efficiency of 7.27%,[40] and within just 10 years efficiencies have grown to now exceed 23% in single junction devices.[30] However, the stability of lead-tin perovskite solar cells under operating conditions lags far behind that of its neat-Pb counterparts, with significant performance losses during the first tens to hundreds of hours of aging under light exposure at elevated temperatures.[41] Hence, improving the stability of lead-tin perovskite solar cells is one of the most essential hurdles to overcome towards the commercialization of all-perovskite multi-junction solar cells.

2.2 Stability of perovskite materials

Device stressing conditions

The stability of MHP solar cells is currently far inferior to established photovoltaic technologies (like silicon), which represents the main barrier to commercialization. Modules aim to pass commercial qualifications standards which include stressing complete devices under elevated temperature, illumination, humidity, bias, and outdoor weather conditions.

There remain major challenges to achieve good stability of research-level devices under such conditions. Even for the most stable devices, the time taken for device efficiency to decrease to 80% of its original value (t_{80}) under operating conditions (illumination, bias and elevated temperatures) rarely exceeds 1000 hours.[42]

Advances in encapsulation technology are increasingly able to keep oxygen and moisture away from devices during stressing. On a research scale, the stability of perovskite solar cells is therefore often tested by stressing under 1 sun illumination and elevated temperatures, at maximum power point (MPP) or open circuit conditions. Whilst this does not perfectly emulate field conditions (with cyclic illumination, partial shading and temperature variation), it has been found to successfully uncover module-relevant degradation modes at an accelerated rate.[43]

The efficiency of perovskite solar cells may decrease under stressing due to a number of different degradation mechanisms, which are summarized in Figure 2.4 and discussed in the subsequent sections. When investigating why perovskite solar cells fail under stressing, it is useful to separately investigate the stability of each component and material interaction making up the device.

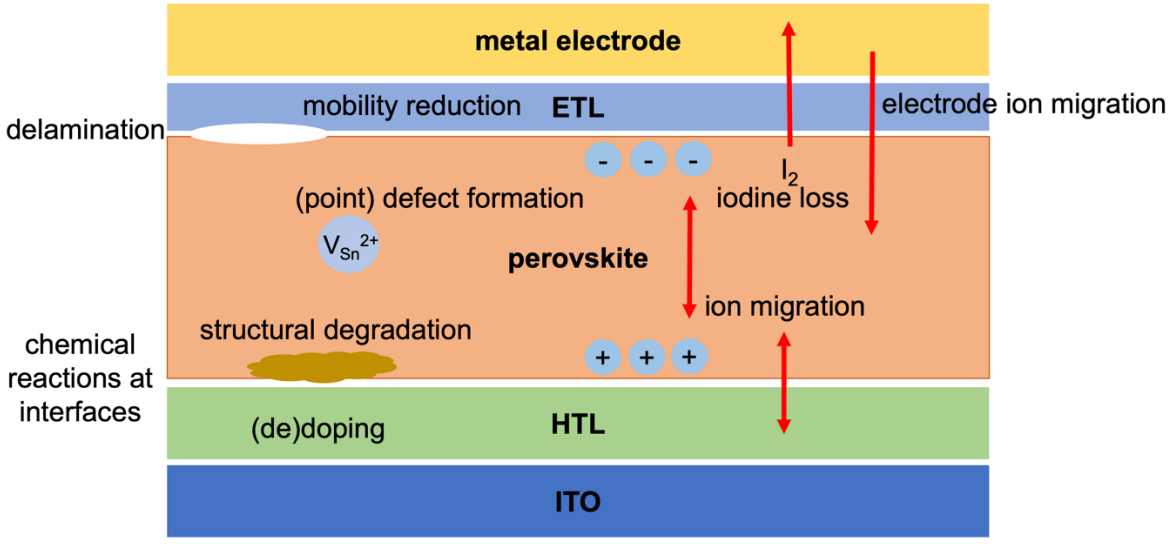


Figure 2.4. Overview of some relevant degradation modes in perovskite solar cells.

Degradation of the perovskite phase

Larger-scale structural degradation of the perovskite phase can result in decreased light absorption, pinhole formation (enabling shunt formation by metal electrode migration) and delamination at surfaces (causing reduced charge extraction). The thermodynamic stability of the halide perovskites in their desired photoactive cubic phase depends on their composition. As crystallization kinetics strongly influence phase growth in halide perovskites, metastable phases can be created.[44] A common way to improve stability of the cubic phase is mixing at the A-cation site (and sometimes also the B-cation and halide sites), which is now ubiquitously employed in perovskite solar cells.[44] However, this can lead to phase separation as a degradation pathway, depending on the stability of the unmixed phases.

Even if the perovskite can be stabilized in the cubic phase at operational temperatures, chemical reactions with residual solvents,[45] CTL components,[46] or electrode materials[47] may still break down the perovskite phase. These reactions can be catalysed by light exposure.[42] Recently, attention has increasingly focused on the role of iodine chemistry in degradation of the perovskite phase. I^- interstitials can become oxidized to I_2 and/or travel into CTLs or electrodes in MHP solar cells, resulting in iodine loss from the perovskite bulk.[48]

Phase changes may be measured by X-ray diffraction (XRD), which can track changes in crystallinity and detect the appearance of crystalline degradation products. Scanning electron microscopy (SEM) (top-down and cross-sectional) and energy dispersive X-ray-SEM (EDX-SEM) can track additional changes in morphology and surface composition that may appear along with phase degradation. Changes in light absorbance and conversion as a result of perovskite degradation can also be tracked by absorbance and external quantum efficiency (EQE) measurements. Additionally, phase changes may result in a change in perovskite bandgap, which can be reflected in a different position of the

absorbance and EQE onset, or in a different energy of emitted light resulting in a shift in the position of the photoluminescence peak.

Defect formation

Even if the perovskite phase is largely stable, smaller-scale structural degradation can already significantly affect device performance by increasing the density of point defects such as vacancies and interstitials in the perovskite layer. The types of defects present in the bulk and at the surfaces of MHPs are illustrated in Figure 2.5. These defects may accelerate non-radiative recombination, change the E_F of the perovskite, and decrease mobility.[49,50] Defects created at interfaces can slowly migrate into the perovskite bulk, and high local densities of defects may further promote specific degradation reactions.[51,52] The effect of changes in the density of a point defect on recombination, mobility of E_F in the perovskite material varies widely per defect and perovskite composition. Point defect densities around 10^{15} cm^{-3}, corresponding to 10^{-5} % of the lattice sites, can already significantly increase non-radiative recombination in the perovskite if defects are highly recombination-active.

Changes in defect chemistry and their effects on the properties of the perovskite material may be quantitatively investigated by probing the transient charge carrier density after light excitation, to extract recombination rates. Charge carrier densities affect both the photoluminescence (stemming from radiative recombination) and the conductivity of the perovskite. Hence, changes in charge carrier density over time after excitation can be tracked by time-resolved photoluminescence (TRPL) or time-resolved photoconductivity (TPC). Another popular characterization method is determination of the photoluminescence quantum efficiency (PLQE), which reflects the ratio of band-to-band radiative recombination to total recombination. Interpretation of these measurements can be complex in the case of multiple

dominant recombination mechanisms, and may benefit from supplementation by recombination simulations (further discussed in section 2.4).

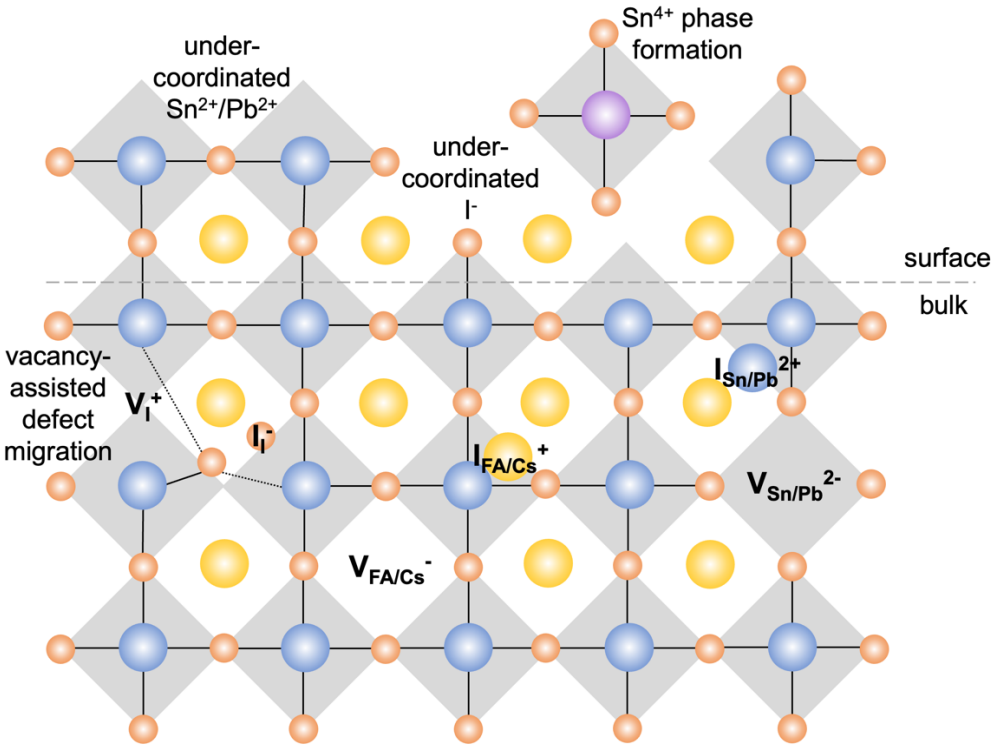


Figure 2.5. Diagram presenting atomic-scale defects and degradation of perovskite material.

Charge transport layer degradation

For optimal perovskite solar cell performance, CTLs ideally require high charge carrier conductivities, appropriate HOMO/LUMO and Fermi levels for efficient hole or electron transfer from perovskite to the CTL, and good morphological contact with the perovskite.[53] Each of these properties may change under illumination and elevated temperatures by structural changes to the CTL material,[54] chemical interaction and/or ion exchange between the CTL and the perovskite,[55,56,57] or interfacial strain.[58] Hence, chemically inert CTLs with good mechanical and structural stability and ion-blocking properties are desirable for best stability.

Ion migration & field screening

The perovskite structure is made up of ionic species, some of which are sufficiently mobile to migrate through the device in response to an applied bias. Both halide and A-cations have been predicted to be able to diffuse through the perovskite on timescales of milliseconds to hours by vacancy assisted hopping.[59,60] Ionic species stemming from other device components, such as electrode metals, may also be able to migrate into other layers of the device structure.[47] As aforementioned, one effect of such migration is undesirable chemical interaction between device components, such as the reaction of iodide species from the perovskite with an Ag electrode.[61]

A second effect of rapid bias-induced ion migration is the accumulation of mobile ions such as iodide vacancies at the CTL interfaces of the perovskite absorber during device operation, as illustrated in Figure 2.6. There, the bias-induced accumulation of ionic species can localize the electric field to a thin region at the interface, resulting in screening of the electric field across the bulk of the absorber layer. This reduces device performance by hindering charge extraction.[62,63,64]

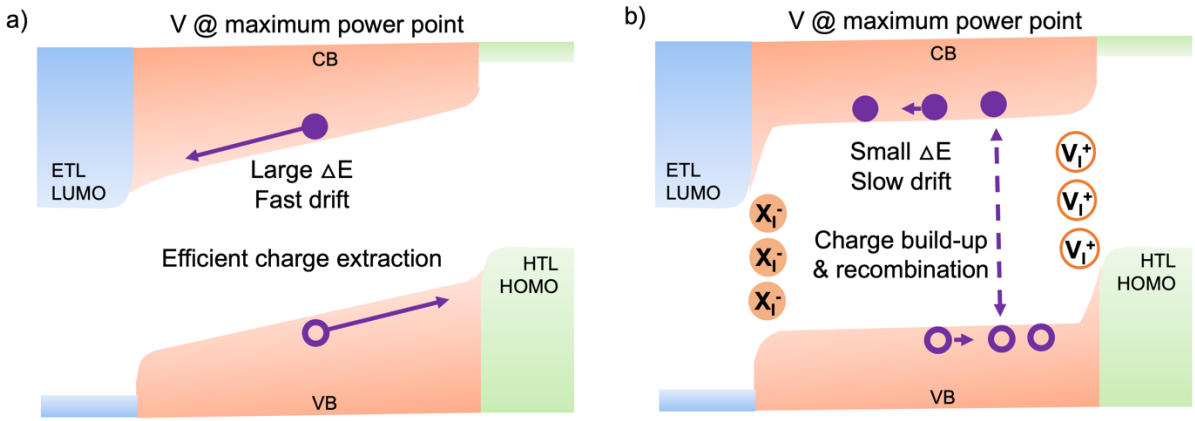


Figure 2.6. Diagrams of energetic band alignment in perovskite solar cell, a) without accumulation of mobile ions at interfaces, and b) with mobile ions accumulated at interfaces.

Effect of tin substitution on perovskite stability

Thus far, stability issues affecting all perovskite compositions have been discussed. For lead-tin perovskites specifically, the use of Sn^{2+} can have an additional two-fold detrimental effect on stability. First, Sn-containing perovskites are expected to have a different defect chemistry compared to neat Pb perovskites, mainly as a consequence of the higher CB and VB energies. One effect of this different defect chemistry is increased p-doping in the as-grown lead-tin MHPs, [51] which can affect recombination dynamics as well as energetic alignment at interfaces within photovoltaic devices. Defects also have different formation energies – unlike neat-Pb perovskites, oxidized iodine interstitials (I_i^+) are not expected to be stable in the lead-tin perovskites.[51] These factors may affect the prevalence of certain degradation reactions. Second, the facile oxidation of Sn^{2+} to Sn^{4+} can break down the original perovskite phase and form recombination centers.[51,65] As Sn^{2+} oxidation is likely initiated at surfaces, surface degradation can significantly affect device performance even if the bulk remains intact.[65,66] Encouragingly, Sn^{2+} oxidation has been suggested to proceed slower in 50:50 lead-tin compared to neat tin perovskites.[67]

As Sn^{2+} oxidation is assisted by oxygen,[68] it is expected to be slowed down with advances in air-free device packaging.[69] Indeed, multiple studies have reported an improvement in the stability and performance of lead-tin perovskite-based devices through the use of protective capping layers that block atmospheric oxygen and moisture such as sputtered indium-doped tin oxide (ITO),[70] indium-doped zinc oxide[71] or atomic-layer-deposition tin oxide.[72] Further interventions found to improve the stability of lead-tin perovskite based solar cells under encapsulated or air-free conditions have been the inclusion of a discontinuous Al_2O_3-nanoparticle 'buffer' layer between the perovskite and electron transport layer,[73] the increase of polycrystalline perovskite grain size[71] and the removal of the

poly(3,4-ethylenedioxythiophene) polystyrene sulfonate (PEDOT:PSS) hole transport layer (HTL).[71,74] Notable examples of unusually stable lead-tin perovskite devices are the achievement of 1000 hours of stable maximum power point (MPP) operation in N_2 of a HTL-free single junction lead-tin device,[71] as well as the good operational stability over hundreds of hours of some all-perovskite tandems employing lead-tin perovskites under ISOS-L1[75] aging conditions.[72,76]

Despite these promising advances, the consensus in the field remains that lead-tin perovskite solar cells tend to have significantly inferior stability compared to their neat-lead counterparts. The most efficient lead-tin perovskite solar cells suffer from significant performance losses during the first tens to hundreds of hours of aging under light exposure at elevated temperatures, even when encapsulated.[41] It remains unclear which factors ultimately limit the long-term device stability, and whether these are inherent to the lead-tin perovskite material itself or stem from another aspect of the device. These questions are investigated in Chapter 4.

2.3 Doping perovskite materials

Doping semiconductors

Manipulation of the Fermi energy level (E_F) position has been critical to the development of many optoelectronic devices, including Si photovoltaics. This is usually accomplished by the introduction of impurity elements in the semiconductor lattice. For example, B^+ substituted into the Si lattice stably traps a free electron, permanently leaving an extra hole behind in the valence band. In contrast to Si, halide perovskites have a more varied and potentially larger population of native lattice defects,[38,50] which is expected to affect doping.

In halide perovskites, manipulation of the position of E_F has been found to be surprisingly challenging compared to other semiconductor materials.[77] Theoretical investigation suggests that this is mainly due to the facile formation of compensatory intrinsic defects in perovskite in response to doping, and the difficulty in finding dopants with formation energies much smaller than the most stable structural defect.[78] Hence, the impact of impurity dopants on E_F in halide perovskites depends not only the position of their trapping or 'bonding' energy levels in the perovskite bandgap, but also on their effect on the formation energies of native perovskite defects.

The doping levels of halide perovskites are challenging to measure, as background charge carrier densities are generally low. Hall effect measurements are normally used in conventional and organic semiconductors, but the background carrier density/conductivity of most halide perovskite composition is so low that these measurements are challenging even with the most sensitive methods.[79]

Intrinsic perovskite doping via stoichiometry control

The position of E_F in halide perovskite materials is determined by the as-grown population of charged native lattice defects. Figure 2.7a shows an example of the formation energies of multiple difference perovskite defects, which depend on E_F. The E_F is pinned at the crossing of the lowest-formation energy (highest density) acceptor and donor defects.[77,78] There still exists significant argument in the community about whether certain halide perovskite compositions can be considered intrinsic, p-type or n-type.[77] This is likely because small differences in perovskite stoichiometry and growth conditions can lead to significant variation in defect formation energies, which subsequently pin E_F in a different position.[51]

Attempts have been made to shift E_F by adjustment of the formation energy/density of defects in the as-grown perovskite. This is normally achieved by purposefully introducing an

over- or under-stoichiometry of the perovskite precursor materials. For example, iodide-poor growth conditions result in an increased density of iodide vacancies and a reduced density of iodide interstitial, causing a shift in E_F towards the VB (Figure 2.7a). Such shifts have been demonstrated in both $MAPbI_3$ and $FAPbI_3$.[78]

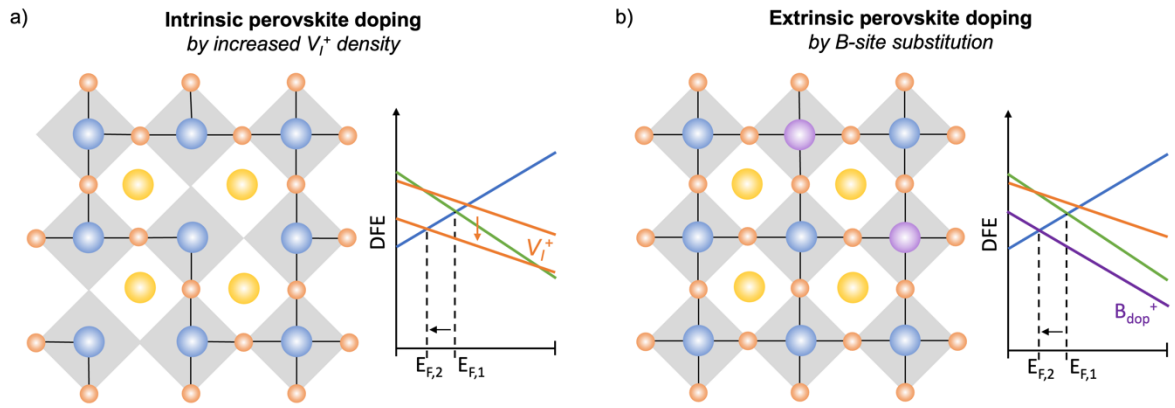


Figure 2.7. Diagrams showing a) a shift in E_F when the density of iodide vacancies in the perovskite lattice is increased, for example by stoichiometry control, and b) a shift in in E_F upon the introduction of an extrinsic lattice impurity (purple line). Defect formation energy positions are loosely adapted from DFT simulation results of $MAPb_{0.5}Sn_{0.5}I_3$ performed by Meggiolaro et. al.[51]

Extrinsic perovskite doping via substitution

An alternative doping strategy is the introduction of extrinsic lattice impurities, illustrated in Figure 2.7b. Here, an impurity ion substitutes the B-site cation and so creates a new defect state. If the formation energy of this state is sufficiently low, it can induce a shift in E_F. Unlike in Si, the doping induced by the impurity is almost always partially compensated by an increase in the density of some native defect resulting from the induced E_F shift.

The most popular class of extrinsic perovskite dopants have been metal ions with a +1, +2 or +3 oxidation state, which are thought to incorporate at the B-cation site. A wide range of metal ions including alkali metals (Na^+, K^+, Rb^+, Cs^+),[80,81] trivalent metals (Ga^{3+}, In^{3+}, Sb^{3+},

Bi^{3+}),[82,83,83–85] and transition metals (Ag^{+}, $Cu^{+/2+}$, Zn^{2+})[86–88] have been used to dope hybrid halide perovskites of various compositions. There have also been previous experimental indications that the background carrier density of perovskites was indeed modulated through doping, e.g. by Ga^{3+} in lead-tin perovskites,[85] and Bi^{3+} in neat lead perovskites.[82] However, the aim of this doping is not always to shift E_F - sometimes the change in native point defect formation energies caused by these dopants is more desirable, to reduce recombination or increase stability in the perovskite material. In theory, the ability to control both the defect chemistry and E_F position hence makes these metal dopants highly promising additives for perovskite solar cells.

Secondary effects of doping in perovskites

In practice, the doping of metal ions into the perovskite lattice is also associated with significant challenges. The incorporation and stability of dopants within the perovskite lattice depends strongly on ionic radius. Metal ions much smaller or larger than Sn^{2+}/Pb^{2+} are unlikely to be incorporated in the lattice at significant densities,[82,89] be incorporated preferentially at interfaces,[85] or even migrate out of the perovskite structure over time, reversing the effects of doping.[81]

In addition to this, the charge imbalance introduced by the incorporation of heterovalent dopants is expected to be partially compensated by the formation of negatively charged defects such as Pb^{2+} vacancies, A-cation vacancies or I^{-} interstitials,[82,85] which will not only decrease doping efficiency but may also negatively impact optoelectronic properties. As the density of defects expected to form is related to their formation energy by e^{-E_F/k_BT} (where k_B is the Boltzmann constant and T the growth temperature), a 10-fold change in defect density can be caused by a relatively minor change in defect formation energy.[90] Experiments have indeed indicated that the incorporation of extrinsic dopants with a 3+

charge at the B^{2+}-site in neat-lead halide perovskites is compensated by the formation of negatively charged defects such as Pb^{2+} vacancies, A-cation vacancies or I^- interstitials.[82,85]

Doping tin-containing perovskites

The ability to control E_F, and consequently the background charge carrier density, is especially desirable for tin-containing perovskites. Neat tin and mixed lead-tin perovskites have been found to grow intrinsically p-type due to due to a shift in the energy of the perovskite VB maximum towards the vacuum level, inducing a stabilization of the acceptor defects in the material.[51] In perovskite compositions with a 50:50 lead-tin ratio, background hole densities in the range 10^{14} – 10^{17} cm^{-3} have been reported,[91,92,93] whilst in neat-Sn perovskites background hole density is thought to exceed 10^{18} cm^{-3}.[94] Such a wide range of reported values can be explained by variations in processing conditions between labs, particularly the extent of oxygen exposure before and during film deposition, which can strongly affect the density of Sn^{2+} vacancies. This background carrier density is expected to negatively affect the energetic alignment within devices when it is larger than $\sim 10^{15}$ cm^{-3},[95] and to accelerate recombination kinetics when it is larger than the photoexcited carrier density (10^{14}-10^{15} cm^{-3} at 1 sun illumination). Hence, there is significant interest in reducing background carrier density in these materials by shifting E_F towards mid-gap, and ensuring this shift is maintained during material aging/stressing.

Existing strategies include the use of SnF_2 and Sn metal additives, which have already been shown to successfully limit tin oxidation during perovskite film deposition.[93,94,96] However, the magnitude by which these strategies can reduce self-p-doping in Sn-based perovskites has been indicated to be limited.[94] There is hence a need to improve our understanding of the effects of extrinsic dopants in such systems and this is explored in Chapter 5.

2.4 Modelling recombination in perovskite materials

Recombination processes

Figure 2.8 illustrates a selection of recombination processes that may collectively form a comprehensive recombination model. In thin film 3D MHPs, physical models of recombination typically include radiative band-to-band recombination and phonon-assisted trap-assisted recombination. At higher carrier densities, both band-to-band recombination and trapping processes can also occur via Auger processes, in which excess energy is transferred to other free carriers rather than being emitted by photons or phonon. In Sn-containing perovskites, an elevated background hole density can further influence the recombination dynamics for all of these mechanisms, particularly when it surpasses the density of photogenerated electrons. Mathematical formulations for these physical mechanisms are detailed in the sections below.

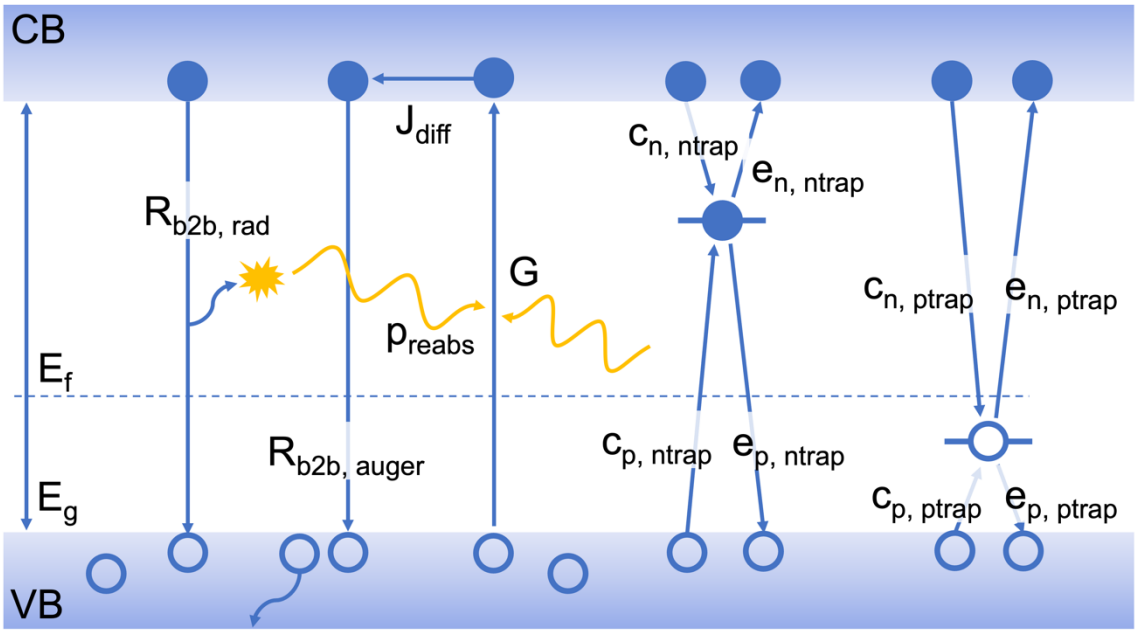


Figure 2.8. Diagram representing various recombination modes in a photoactive semiconducting material.

Background carrier density

Some background density of electrons and holes is present in the semiconductor under dark conditions due to thermal excitation. The balance between these electron and hole populations depends on the E_F of the material. The background carrier densities, n_0 and p_0, are described by equations 2.1-3. Here, m_{eff} refers to the effective mass of the electrons/holes, E_{CB}/E_{VB} to the conduction and valence band energies, and $\Delta n/p$ to the photoexcited free electron and hole densities. In neat-lead perovskites, E_F is usually predicted to lie in the middle of the bandgap,[77] such that n_0 and p_0 are of a similar (small) magnitude.

$$n_0 = 2\left(\frac{m_{\mathrm{eff,n}} ekT}{2\pi\hbar^2}\right)^{\frac{3}{2}} e^{\frac{-(E_{\mathrm{CB}}-E_{\mathrm{F}})}{kT}} \quad (2.1)$$

$$p_0 = 2\left(\frac{m_{\mathrm{eff,p}} ekT}{2\pi\hbar^2}\right)^{\frac{3}{2}} e^{\frac{-(E_{\mathrm{F}}-E_{\mathrm{VB}})}{kT}} \quad (2.2)$$

$$n = n_0 + \Delta n, \qquad p = p_0 + \Delta p \quad (2.3)$$

Free carrier generation & diffusion

In addition to the background charge carriers, free charge carriers can be added by injection or by generation from absorbed photons. Due to the aforementioned low exciton binding energies in perovskites, it can be assumed that every absorbed photon generates a free electron and a free hole.[97] The generation profile of electrons and holes after photoexcitation is given by equation 2.4, where P_{exc} refers to the density of absorbed photons, and α is the absorption coefficient.

$$G(x) = P_{exc} \cdot e^{-\alpha x} \quad (2.4)$$

Depending on the absorption coefficient at the excitation wavelength, photogenerated carriers may be distributed more towards the illuminated side of the film. This necessitates

the use of a model that is spatially resolved in the cross-sectional dimension and simulates 1D diffusion of charge carriers in addition to recombination processes. In this thesis, drift of charge carriers in response to an electric field across the absorber is neglected, limiting the modelling to isolated perovskite films.

To solve the diffusion equation 2.5, we divide the absorber into some number of segments with mid-points x_i at which a carrier density is defined. We then use a finite-difference scheme to discretize the change in free charge carriers n_i per segment, as illustrated in Figure 2.9. This scheme uses the assumption that the current between two adjacent points x_i is constant. This results in the expression for diffusion given in equation 2.7.

$$\frac{dn}{dt}_{\text{diff}} = D_{\text{n}} \frac{d^2 n}{dx^2} \tag{2.5}$$

$$D_{\text{n}} = \frac{\mu_{\text{n}} k_{\text{B}} T}{q} \tag{2.6}$$

$$\frac{dn_i}{dt}_{diff} = D_n \frac{\frac{n_{i-1} - n_i}{x_i - x_{i-1}} - \frac{n_i - n_{i+1}}{x_{i+1} - x_i}}{\frac{(x_{i+1} - x_{i-1})}{2}} \tag{2.7}$$

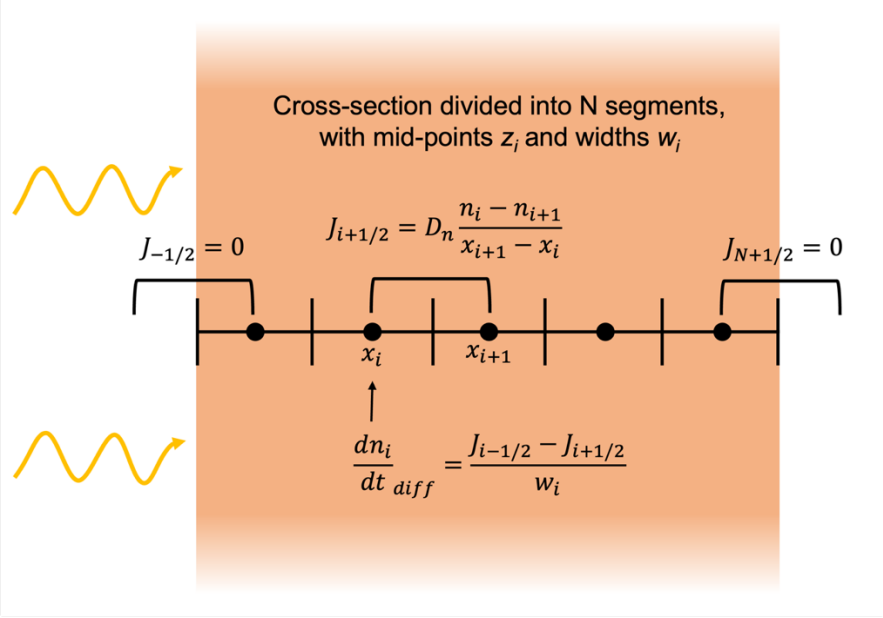


Figure 2.9. Diagram of scheme used to discretize diffusion equation.

Radiative & Auger band-to-band recombination

The two dominant band-to-band recombination processes in perovskites occur radiatively and via a non-radiative Auger mechanism.[98] They are described in equations 2.8 and 2.9 for the rates of Auger (R_{aug}) and radiative (R_{rad}) recombination, which contain the Auger coefficients $k_{aug,n}$ and $k_{aug,p}$ and the internal radiative recombination coefficient $k_{rad,\,int}$. For MHPs, Auger coefficients in the range of 10^{-29}-10^{-27} cm^6 s^{-1} have been reported, in good agreement with theoretical prediction of 7 x 10^{-29} cm^6 s^{-1}.[99] When radiative recombination emits a photon inside the material, there is a probability that it will be reabsorbed (p_r). Hence, there exist and internal and externally measured radiative recombination rate. Multiplying the internal radiative recombination coefficient by the probability of photon emission hence gives the external radiative recombination coefficient $k_{rad,ext}$. In MHPs, external radiative recombination coefficients in the range of 10^{-11}-10^{-10} cm^3 s^{-1} have been reported, corresponding to internal radiative recombination coefficients of 5 x 10^{-11}-9 x 10^{-10} cm^3 s^{-1} when assuming a 75-97% probability of reabsorption.[100] This is also in good agreement with first principles simulations, which predict an internal radiative recombination coefficient of ~10^{-10} cm^3 s^{-1}.

$$R_{aug} = (k_{aug,n}n + k_{aug,p}p)\,(np - n_0p_0) \qquad (2.8)$$

$$R_{rad} = k_{rad,ext}(np - n_0p_0) \qquad (2.9)$$

Trap-assisted recombination

In perovskites, defects in the crystal structure can trap free electrons (or holes), and the trapped carrier can consequently recombine with holes (or electrons) in the VB (CB). Such trapping processes conventionally release energy by phonon emission (non-radiative), but trapping may in some cases also take place by photon emission (radiative),[101] or by a

bimolecular Auger process in which energy is transferred to another free electron or hole (non-radiative).[102] However, in most 3D MHP thin film materials phonon-assisted trapping is expected to dominate.[103,102]

The statistics of trap-assisted nonradiative recombination were first described by Hall,[104] Shockley, and Read.[105] The net rate at which trapping occurs depends on the density of free electrons/holes (n/p), the density of trapped carriers (n_t/p_t), the electron/hole capture coefficients ($\beta_{n/p}$), the density of unoccupied trap states (N_T), the distance of the trap energy level from the CB/VB (E_T), and the density of states at the CB/VB (N_C/N_V). The rates of hole and electron trapping into an electron trap are given in equations 2.10 and 2.11, and the same processes for a hole trap are given in equations 2.12 and 2.13. A recombination model may include multiple traps.

$$R_{ntrap,\ n} = \beta_n n(N_t - n_t) - \beta_n \left(N_C e^{\frac{E_T - E_{CB}}{kT}}\right) n_t \tag{2.10}$$

$$R_{ntrap,\ p} = \beta_p p n_t - \beta_p \left(N_V e^{\frac{E_{VB} - E_T}{kT}}\right) (N_t - n_t) \tag{2.11}$$

$$R_{ptrap,\ p} = \beta_p p(N_t - p_t) - \beta_p \left(N_C e^{\frac{E_{VB} - E_T}{kT}}\right) p_t \tag{2.12}$$

$$R_{ptrap,\ n} = \beta_n n p_t - \beta_n \left(N_V e^{\frac{E_T - E_{CB}}{kT}}\right) (N_t - p_t) \tag{2.13}$$

This system of equations is often simplified with the assumption that the fraction of occupied trap sites remains negligibly small throughout the entire modelled recombination process, resulting in equation 2.14 for the rate of non-radiative trap-assisted recombination. The resulting recombination rate can then be quantified by a free charge carrier lifetime τ, equal to $(\beta N_t)^{-1}$. This holds true if the net hole and electron trapping rates trapping rates are approximately equal.

$$R_{recomb,\ ntrap} = (\beta_n N_t)n = \frac{n}{\tau_n} \tag{2.14}$$

Complete system of equations for TRPL & PLQE calculation

The processes described above can be combined into one model, which results in the following system of ordinary differential equations (ODEs) to describe the change in the population of free and trapped charge carriers, resolved in space and time (equations 2.15-18).

$$\frac{dn}{dt}(x,t) = G(x,t) - D_n \frac{d^2n}{dx^2}(x,t) - R_{aug}(x,t) - R_{rad}(x,t) - \Sigma_i R_{trap\ i,\ n}(x,t) \tag{2.15}$$

$$\frac{dp}{dt}(x,t) = G(x,t) - D_p \frac{d^2p}{dx^2}(x,t) - R_{aug}(x,t) - R_{rad}(x,t) - \Sigma_i R_{trap\ i,\ p}(x,t) \tag{2.16}$$

$$\frac{dn_{ntrap\ i}}{dt}(x,t) = R_{ntrap\ i,\ n}(x,t) - R_{ntrap\ i,\ p}(x,t) \tag{2.17}$$

$$\frac{dp_{ptrap\ i}}{dt}(x,t) = R_{ptrap\ i,\ p}(x,t) - R_{ptrap\ i,\ n}(x,t) \tag{2.18}$$

Inferring model parameters from experimental data

Parameters such as trap density or recombination coefficients may be inferred from experimental data by comparing it to the recombination model thus far constructed. This requires finding the set of parameters for which the modelled TRPL/PLQE is as close as possible to the experimental data. ‘Fitting’ a model to data in such a way normally involves the formulation of a ‘loss function’, which expresses how different the modelled data is from

the experimental data for a given set of parameters. Classically, the 'mean square error' shown in equation 2.23 is used for this, where y_{exp} is the experimental data and y_{model} is the modelled data for the set of parameters P. Errors are weighted by the measurement uncertainty of the experimental data, σ_{exp}.

$$MSE(P) = \frac{1}{N}\sum_{i=1}^{N} \frac{1}{\sigma_{exp,i}} \left(y_{\mathrm{exp,i}} - y_{\mathrm{model,i}}\,(P) \right)^2 \qquad (2.19)$$

From an initial set of parameters, an algorithm is used to sequentially choose a next set of parameters until the local or global minimum of the MSE is found. The Levenberg–Marquardt (LM) algorithm is a suitable choice for local optimization of non-linear functions,[106,107] whereas the Simplicial Homology Global Optimisation (SHGO) algorithm is useful when multiple local minima are expected.[108] An example of an optimization process for a loss function is shown in Figure 2.10. Depending on the algorithm, bounds based on previous knowledge of the probable range of values for each parameter can be provided to constrain parameter selection. Uncertainties of the output parameters can be estimated using the covariance matrix calculated by taking the inverse of the 'Hessian matrix', containing the second derivative of the MSE function for each variable parameter. These uncertainties represent how much information the data provides about each parameter, given the model used.[109]

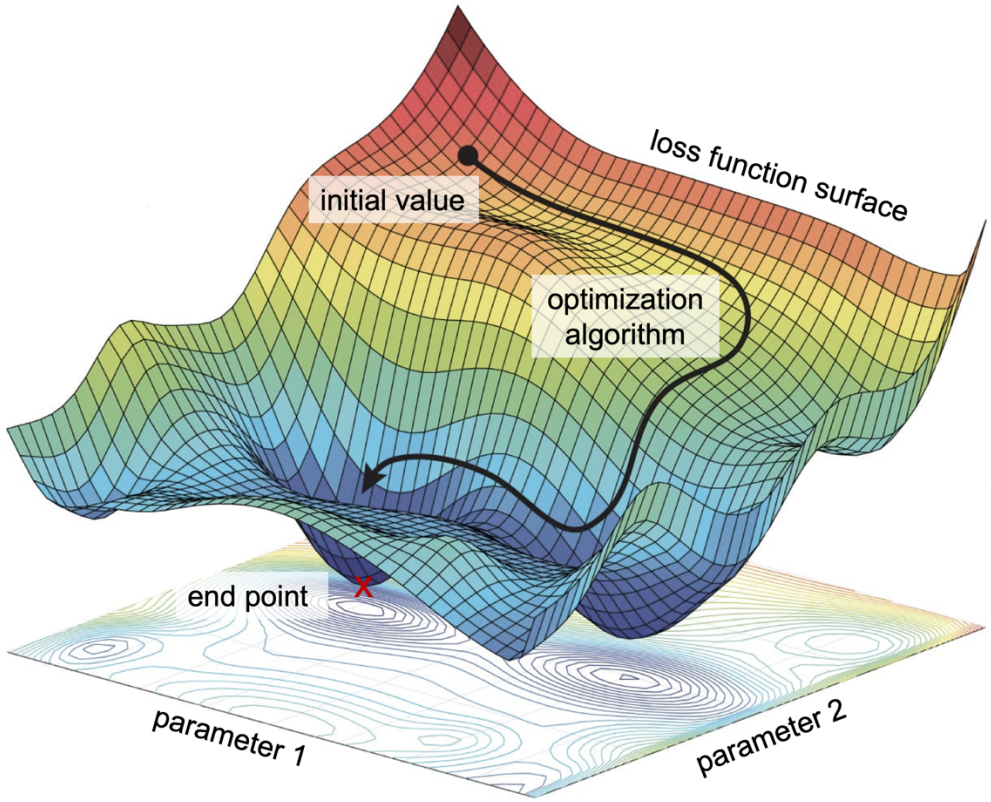


Figure 2.10. Diagram of a loss function of two parameters with multiple local minima. Black arrow represents path of optimization algorithm to find the minimum of the loss functions within the constraints of the parameter space. Figure adapted from Amini et al.[110]

Bayesian inference

Bayesian inference is an alternative, probabilistic approach to extracting parameters from the fitting of a model to experimental data. This approach views parameters as probability distributions. Instead of providing bounds for fitting parameters, a 'prior' probability distribution (which does not have to be a normal distribution) is provided for each parameter to encode initial knowledge about it. Bayes' rule is then used to calculate 'posterior' probability distributions for each parameter given the prior distributions, the experimental data, and the model used (equation 2.24). In this expression, *P*(param | model)

is the prior distributions and *P*(data | param, model) is the cost function named the 'likelihood', the log of which is optimized and given in equation 2.25.

$$P(\text{param}|\text{data}, \text{model}) = \frac{P(\text{data}|\text{param}, \text{model}) \cdot P(\text{param}|\text{model})}{P(\text{data}|\text{model})} \quad (2.20)$$

$$P(\text{data}|\text{param}, \text{model}) \quad (2.21)$$

$$= \frac{1}{N} \sum_{i}^{N} -\frac{1}{2}\left(\frac{\left(y_{\text{exp,i}} - y_{\text{model,i}}\,(P) \right)^2}{{\sigma_{exp,i}}^2} + \log\left(2\pi {\sigma_{exp,i}}^2\right) \right)$$

P(data | model), often termed the 'evidence', acts as a normalization factor for the posterior distributions. It can also be used to evaluate the model choice, which is discussed further in the next section. The output posterior distributions obtained for each fitting parameter reflects the knowledge we have about these parameters given the data, model and prior knowledge provided. Bayesian inference provides a simple way to both encode prior knowledge and describe uncertainty in the output parameters of fits, making it increasingly popular for data interpretation across the sciences.[111]

As the evaluation of expression 2.24 normally involves an integral over all parameter dimension, it can rarely be solved analytically. Instead, computational approaches are used to estimate the posterior distributions and/or the evidence.[112] Often, this involves 'sampling' the probabilities in expression 2.24 for certain sets of parameters to construct distributions. The points at which the function is evaluated are selected by some algorithm. One popular option, the Markov Chain Monte Carlo (MCMC) algorithm,[113,114] avoids computation of the complex evidence term P(data | model) by sampling from a normalized posterior distribution which is proportional to the actual posterior. However, as mentioned, computing the evidence is useful for model comparison, and this can be done with the Nested Sampling algorithm.[115]

Bayesian model selection

As outlined in the previous sections, various recombination mechanisms can contribute to charge carrier kinetics within perovskite materials and devices. This means that inferring model parameters from experimental data always necessitates a choice of a certain recombination model, which will affect the inferred material properties (such as trap density). Such a choice can be substantiated by a quantitative approach to model selection, during which multiple models can be compared.

One approach to quantitative model comparison within the Bayesian framework is the 'Bayes factor', introduced by Jeffreys as a framework to make decisions about which model should be used to describe data.[116] The Bayes Factor is the ratio of the probabilities of two different models, given the same set of data (equation 2.26). The probability *P*(model | data, priors) is given by the product of the aforementioned 'evidence', *P*(data, priors | model), and the prior knowledge about the probability of the model, P(model). When there is no prior reason to prefer one model over another, the second term in equation 2.26 simplifies to 1. The choice of a different set of priors can strongly affect the value of the Bayes factor. Hence, when the aim is direct comparison between two models, the same set of priors is normally used. Recommendations for the interpretation of Bayes Factors were made by Kass & Raftery and are reproduced in Table 2.1.[117]

$$BF = \frac{P(model_1|data, priors)}{P(model_2|data, priors)} = \frac{P(data, priors|model_1)}{P(data, priors|model_2)} \cdot \frac{P(model_1)}{P(model_2)} \qquad (2.22)$$

Table 2.1. Interpretation of Bayes Factor for two competing models suggested by Kass & Raftery.[117]

$\log_{10}$ (BF)	Evidence against model 1
0 - 0.5	Not worth more than a bare mention
0.5 - 1	Substantial
1 - 2	Strong
>2	Decisive

Computation of the evidence P(data, priors | model) can be done by the Nested Sampling algorithm for Bayesian inference, developed by Skilling et al.[115] This approach directly computes both the posterior distributions of parameters and the evidence for a given model. Repeating such computation for several different models allows for quantitative comparison between models.

In Chapter 6, this approach is used to evaluate a range of recombination models for inference on TRPL and PLQE data in lead-halide perovskites. The recombination model outlined here is also used to simulate the effect of certain parameter changes to evaluate their importance in these materials.

2.5 Works cited

1. European Union. *World Energy Technology Outlook - 2050*. (2012).
2. V. Masson-Delmotte, P. Zhai, H. O. Pörtner, D. Roberts, J. Skea, P.R. Shukla, A. Pirani, W., Moufouma-Okia, C. Péan, R. Pidcock, S. Connors, J. B. R. Matthews, Y. Chen, X. Zhou, M. I. Gomis, E. Lonnoy, & T. Maycock, M. Tignor, T. Waterfield (eds.)]. *IPCC, 2018: Global Warming of 1.5°C. An IPCC Special Report on the Impacts of Global Warming of 1.5°C above Pre-Industrial Levels and Related Global Greenhouse Gas Emission Pathways, in the Context of Strengthening the Global Response to the Threat of Climate Change, Sustainable Development, and Efforts to Eradicate Poverty*.
3. Shih, C. F., Zhang, T., Li, J. & Bai, C. Powering the Future with Liquid Sunshine. *Joule* **2**, 1925–1949 (2018).
4. Becquerel, A. E. Recherches sur les effets de la radiation chimique de la lumiere solaire au moyen des courants electriques. *Comptes Rendus de L'Academie des Sciences* **9**, 145–149 (1839).

5. Fritts, C. E. On a New Form of Selenium Photocell. *American J. of Science* **26**, 465 (1883).
6. International Energy Agency. *World Energy Outlook 2022*. (2022).
7. Polman, A., Knight, M., Garnett, E. C., Ehrler, B. & Sinke, W. C. Photovoltaic materials: Present efficiencies and future challenges. *Science* **352**, aad4424–aad4424 (2016).
8. Yan, J. & Saunders, B. R. Third-generation solar cells: a review and comparison of polymer:fullerene, hybrid polymer and perovskite solar cells. *RSC Adv.* **4**, 43286–43314 (2014).
9. Kojima, A., Teshima, K., Shirai, Y. & Miyasaka, T. Organometal Halide Perovskites as Visible-Light Sensitizers for Photovoltaic Cells. *J. Am. Chem. Soc.* **131**, 6050–6051 (2009).
10. O'Regan, B. & Gratzel, M. A low-cost, high-efficiency solar cell based on dye-sensitized colloidal Ti02 films. *Nature* **353**, 737–740 (1991).
11. Kim, H.-S. *et al.* Lead Iodide Perovskite Sensitized All-Solid-State Submicron Thin Film Mesoscopic Solar Cell with Efficiency Exceeding 9%. *Sci Rep* **2**, 591 (2012).
12. Lin, Q., Armin, A., Nagiri, R. C. R., Burn, P. L. & Meredith, P. Electro-optics of perovskite solar cells. *Nature Photon* **9**, 106–112 (2015).
13. Park, N.-G. Perovskite solar cells: an emerging photovoltaic technology. *Materials Today* **18**, 65–72 (2015).
14. Lee, M. M., Teuscher, J., Miyasaka, T., Murakami, T. N. & Snaith, H. J. Efficient Hybrid Solar Cells Based on Meso-Superstructured Organometal Halide Perovskites. *Science* **338**, 643–647 (2012).
15. Etgar, L. *et al.* Mesoscopic $CH_3NH_3PbI_3/TiO_2$ Heterojunction Solar Cells. *J. Am. Chem. Soc.* **134**, 17396–17399 (2012).
16. Stranks, S. D. *et al.* Electron-Hole Diffusion Lengths Exceeding 1 Micrometer in an Organometal Trihalide Perovskite Absorber. *Science* **342**, 341–344 (2013).
17. Xing, G. *et al.* Long-Range Balanced Electron- and Hole-Transport Lengths in Organic-Inorganic CH3NH3PbI3. *Science* **342**, 344–347 (2013).
18. Ponseca, C. S. *et al.* Organometal Halide Perovskite Solar Cell Materials Rationalized: Ultrafast Charge Generation, High and Microsecond-Long Balanced Mobilities, and Slow Recombination. *J. Am. Chem. Soc.* **136**, 5189–5192 (2014).
19. Ball, J. M., Lee, M. M., Hey, A. & Snaith, H. J. Low-temperature processed meso-superstructured to thin-film perovskite solar cells. *Energy Environ. Sci.* **6**, 1739 (2013).
20. Liu, M., Johnston, M. B. & Snaith, H. J. Efficient planar heterojunction perovskite solar cells by vapour deposition. *Nature* **501**, 395–398 (2013).
21. Jeng, J.-Y. *et al.* $CH_3NH_3PbI_3$ Perovskite/Fullerene Planar-Heterojunction Hybrid Solar Cells. *Adv. Mater.* **25**, 3727–3732 (2013).
22. Burschka, J. *et al.* Sequential deposition as a route to high-performance perovskite-sensitized solar cells. *Nature* **499**, 316–319 (2013).
23. Xiao, Z. *et al.* Solvent Annealing of Perovskite-Induced Crystal Growth for Photovoltaic-Device Efficiency Enhancement. *Adv. Mater.* **26**, 6503–6509 (2014).
24. Jeon, N. J. *et al.* Compositional engineering of perovskite materials for high-performance solar cells. *Nature* **517**, 476–480 (2015).

25. Saliba, M., Correa-Baena, J.-P., Grätzel, M., Hagfeldt, A. & Abate, A. Perovskite Solar Cells: From the Atomic Level to Film Quality and Device Performance. *Angew. Chem. Int. Ed.* **57**, 2554–2569 (2018).
26. Hörantner, M. T. *et al.* The Potential of Multijunction Perovskite Solar Cells. *ACS Energy Lett.* **2**, 2506–2513 (2017).
27. Tian, X., Stranks, S. D. & You, F. Life cycle energy use and environmental implications of high-performance perovskite tandem solar cells. *Sci. Adv.* **6**, eabb0055 (2020).
28. Klug, M. T. *et al.* Metal composition influences optoelectronic quality in mixed-metal lead–tin triiodide perovskite solar absorbers. *Energy Environ. Sci.* **13**, 1776–1787 (2020).
29. Savill, K. J., Ulatowski, A. M. & Herz, L. M. Optoelectronic Properties of Tin–Lead Halide Perovskites. *ACS Energy Lett.* **6**, 2413–2426 (2021).
30. Hu, S. *et al. Optimized Carrier Extraction at Interfaces for 23.6% Efficient Tin–Lead Perovskite Solar Cells*. (2021).
31. Lin, R. *et al.* All-perovskite tandem solar cells with 3D/3D bilayer perovskite heterojunction. *Nature* (2023) doi:10.1038/s41586-023-06278-z.
32. Wang, Z. *et al.* Suppressed phase segregation for triple-junction perovskite solar cells. *Nature* **618**, 74–79 (2023).
33. Shockley, W. & Queisser, H. J. Detailed Balance Limit of Efficiency of *p-n* Junction Solar Cells. *Journal of Applied Physics* **32**, 510–519 (1961).
34. De Vos, A. & Pauwels, H. On the thermodynamic limit of photovoltaic energy conversion. *Appl. Phys.* **25**, 119–125 (1981).
35. Lee, M. M., Teuscher, J., Miyasaka, T., Murakami, T. N. & Snaith, H. J. Efficient Hybrid Solar Cells Based on Meso-Superstructured Organometal Halide Perovskites. *Science* **338**, 643–647 (2012).
36. Ponseca, C. S. *et al.* Organometal Halide Perovskite Solar Cell Materials Rationalized: Ultrafast Charge Generation, High and Microsecond-Long Balanced Mobilities, and Slow Recombination. *J. Am. Chem. Soc.* **136**, 5189–5192 (2014).
37. Stranks, S. D. *et al.* Electron-Hole Diffusion Lengths Exceeding 1 Micrometer in an Organometal Trihalide Perovskite Absorber. *Science* **342**, 341–344 (2013).
38. Zhang, X., Turiansky, M. E., Shen, J.-X. & Van De Walle, C. G. Defect tolerance in halide perovskites: A first-principles perspective. *Journal of Applied Physics* **131**, 090901 (2022).
39. Guo, Z., Jena, A. K., Kim, G. M. & Miyasaka, T. The high open-circuit voltage of perovskite solar cells: a review. *Energy Environ. Sci.* **15**, 3171–3222 (2022).
40. Hao, F., Stoumpos, C. C., Chang, R. P. H. & Kanatzidis, M. G. Anomalous Band Gap Behavior in Mixed Sn and Pb Perovskites Enables Broadening of Absorption Spectrum in Solar Cells. *J. Am. Chem. Soc.* **136**, 8094–8099 (2014).
41. Lv, S. *et al.* Stability of Sn-Pb mixed organic–inorganic halide perovskite solar cells: Progress, challenges, and perspectives. *Journal of Energy Chemistry* **65**, 371–404 (2022).
42. Zhu, H. Long-term operating stability in perovskite photovoltaics. *Nature Reviews Materials* **8**, (2023).
43. Tirawat, R. *et al.* Measuring metal halide perovskite single cell degradation consistent with module-based conditions. *Sustainable Energy Fuels* **8**, 546–553 (2024).

44. Simenas, M., Gagor, A., Banys, J. & Maczka, M. Phase Transitions and Dynamics in Mixed Three- and Low-Dimensional Lead Halide Perovskites. *Chem. Rev.* **124**, 2281–2326 (2024).
45. Gallant, B. M. *et al.* A green solvent system for precursor phase-engineered sequential deposition of stable formamidinium lead triiodide for perovskite solar cells.
46. Elnaggar, M. *et al.* Decoupling Contributions of Charge-Transport Interlayers to Light-Induced Degradation of p-i-n Perovskite Solar Cells. *Solar RRL* **4**, 2000191 (2020).
47. Domanski, K. *et al.* Not All That Glitters Is Gold: Metal-Migration-Induced Degradation in Perovskite Solar Cells. *ACS Nano* **10**, 6306–6314 (2016).
48. Bitton, S. & Tessler, N. Perovskite ionics – elucidating degradation mechanisms in perovskite solar cells *via* device modelling and iodine chemistry. *Energy Environ. Sci.* **16**, 2621–2628 (2023).
49. Li, C., Guerrero, A., Huettner, S. & Bisquert, J. Unravelling the role of vacancies in lead halide perovskite through electrical switching of photoluminescence. *Nat Commun* **9**, 5113 (2018).
50. Ball, J. M. & Petrozza, A. Defects in perovskite-halides and their effects in solar cells. *Nat Energy* **1**, 16149 (2016).
51. Meggiolaro, D., Ricciarelli, D., Alasmari, A. A., Alasmary, F. A. S. & De Angelis, F. Tin versus Lead Redox Chemistry Modulates Charge Trapping and Self-Doping in Tin/Lead Iodide Perovskites. *J. Phys. Chem. Lett.* **11**, 3546–3556 (2020).
52. Aristidou, N. *et al.* Fast oxygen diffusion and iodide defects mediate oxygen-induced degradation of perovskite solar cells. *Nat Commun* **8**, 15218 (2017).
53. Rombach, F. M., Haque, S. A. & Macdonald, T. J. Lessons learned from spiro-OMeTAD and PTAA in perovskite solar cells. *Energy Environ. Sci.* **14**, 5161–5190 (2021).
54. Malinauskas, T. *et al.* Enhancing Thermal Stability and Lifetime of Solid-State Dye-Sensitized Solar Cells via Molecular Engineering of the Hole-Transporting Material Spiro-OMeTAD. *ACS Appl. Mater. Interfaces* **7**, 11107–11116 (2015).
55. Luo, J. *et al.* Toward high-efficiency, hysteresis-less, stable perovskite solar cells: unusual doping of a hole-transporting material using a fluorine-containing hydrophobic Lewis acid. *Energy Environ. Sci.* **11**, 2035–2045 (2018).
56. Kerner, R. A. *et al.* Organic Hole Transport Material Ionization Potential Dictates Diffusion Kinetics of Iodine Species in Halide Perovskite Devices. *ACS Energy Lett.* **6**, 501–508 (2021).
57. Ke, Q. B., Wu, J.-R., Lin, C.-C. & Chang, S. H. Understanding the PEDOT:PSS, PTAA and P3CT-X Hole-Transport-Layer-Based Inverted Perovskite Solar Cells. *Polymers* **14**, 823 (2022).
58. Yang, W., Zhong, D., Shi, M., Qu, S. & Chen, H. Toward Highly Thermal Stable Perovskite Solar Cells by Rational Design of Interfacial Layer. *iScience* **22**, 534–543 (2019).
59. Eames, C. *et al.* Ionic transport in hybrid lead iodide perovskite solar cells. *Nat Commun* **6**, 7497 (2015).
60. Pering, S. R. & Cameron, P. J. The effect of multiple ion substitutions on halide ion migration in perovskite solar cells. *Mater. Adv.* **3**, 7918–7924 (2022).

61. Svanström, S. *et al.* Degradation Mechanism of Silver Metal Deposited on Lead Halide Perovskites. *ACS Appl. Mater. Interfaces* **12**, 7212–7221 (2020).
62. Tress, W. *et al.* Understanding the rate-dependent J–V hysteresis, slow time component, and aging in CH $_3$ NH $_3$ PbI $_3$ perovskite solar cells: the role of a compensated electric field. *Energy Environ. Sci.* **8**, 995–1004 (2015).
63. Thiesbrummel, J. *et al.* Ion-induced field screening as a dominant factor in perovskite solar cell operational stability. *Nat Energy* (2024).
64. Zhang, X. *et al.* Rapid degradation behavior of encapsulated perovskite solar cells under light, bias voltage or heat fields. *Nanoscale Adv.* **3**, 6128–6137 (2021).
65. Mundt, L. E. *et al.* Surface-Activated Corrosion in Tin–Lead Halide Perovskite Solar Cells. *ACS Energy Lett.* **5**, 3344–3351 (2020).
66. Hu, S., Smith, J. A., Snaith, H. J. & Wakamiya, A. Prospects for Tin-Containing Halide Perovskite Photovoltaics. *Precision Chemistry* **1**, 69–82 (2023).
67. Leijtens, T., Prasanna, R., Gold-Parker, A., Toney, M. F. & McGehee, M. D. Mechanism of Tin Oxidation and Stabilization by Lead Substitution in Tin Halide Perovskites. *ACS Energy Lett.* **2**, 2159–2165 (2017).
68. Lanzetta, L. *et al.* Degradation mechanism of hybrid tin-based perovskite solar cells and the critical role of tin (IV) iodide. *Nat Commun* **12**, 2853 (2021).
69. Domanski, K., Alharbi, E. A., Hagfeldt, A., Grätzel, M. & Tress, W. Systematic investigation of the impact of operation conditions on the degradation behaviour of perovskite solar cells. *Nat Energy* **3**, 61–67 (2018).
70. Leijtens, T. *et al.* Tin–lead halide perovskites with improved thermal and air stability for efficient all-perovskite tandem solar cells. *Sustainable Energy Fuels* **2**, 2450–2459 (2018).
71. Prasanna, R. *et al.* Design of low bandgap tin–lead halide perovskite solar cells to achieve thermal, atmospheric and operational stability. *Nat Energy* **4**, 939–947 (2019).
72. Xiao, K. *et al.* All-perovskite tandem solar cells with 24.2% certified efficiency and area over 1 cm2 using surface-anchoring zwitterionic antioxidant. *Nat Energy* **5**, 870–880 (2020).
73. Jin, H. *et al.* Alumina Nanoparticle Interfacial Buffer Layer for Low-Bandgap Lead-Tin Perovskite Solar Cells. *Adv Funct Materials* 2303012 (2023).
74. Wu, P. *et al.* Efficient and Thermally Stable All-Perovskite Tandem Solar Cells Using All-FA Narrow-Bandgap Perovskite and Metal-oxide-based Tunnel Junction. *Advanced Energy Materials* **12**, 2202948 (2022).
75. Khenkin, M. V. *et al.* Consensus statement for stability assessment and reporting for perovskite photovoltaics based on ISOS procedures. *Nat Energy* **5**, 35–49 (2020).
76. Lin, R. *et al.* All-perovskite tandem solar cells with improved grain surface passivation. *Nature* **603**, 73–78 (2022).
77. Euvrard, J., Yan, Y. & Mitzi, D. B. Electrical doping in halide perovskites. *Nat Rev Mater* **6**, 531–549 (2021).
78. Sabino, F. P., Zunger, A. & Dalpian, G. M. Intrinsic doping limitations in inorganic lead halide perovskites. *Mater. Horiz.* **9**, 791–803 (2022).
79. Chen, Y. *et al.* Extended carrier lifetimes and diffusion in hybrid perovskites revealed by Hall effect and photoconductivity measurements. *Nat Commun* **7**, 12253 (2016).

80. Shi, R. & Long, R. Atomic Model for Alkali Metal-Doped Tin–Lead Mixed Perovskites: Insight from Quantum Dynamics. *J. Phys. Chem. Lett.* **14**, 2878–2885 (2023).
81. Liu, F. *et al.* Near-Infrared Emission from Tin–Lead (Sn–Pb) Alloyed Perovskite Quantum Dots by Sodium Doping. *Angew Chem Int Ed* **59**, 8421–8424 (2020).
82. Abdelhady, A. L. *et al.* Heterovalent Dopant Incorporation for Bandgap and Type Engineering of Perovskite Crystals. *J. Phys. Chem. Lett.* **7**, 295–301 (2016).
83. Hasegawa, H., Kobayashi, K., Takahashi, Y., Harada, J. & Inabe, T. Effective band gap tuning by foreign metal doping in hybrid tin iodide perovskites. *J. Mater. Chem. C* **5**, 4048–4052 (2017).
84. Ulatowski, A. M. *et al.* Charge-Carrier Trapping Dynamics in Bismuth-Doped Thin Films of $MAPbBr_3$ Perovskite. *J. Phys. Chem. Lett.* **11**, 3681–3688 (2020).
85. Chang, Z. *et al.* Designing Heterovalent Substitution with Antioxidant Attribute for High-Performance Sn-Pb Alloyed Perovskite Solar Cells. *Adv Funct Materials* **33**, 2214983 (2023).
86. Park, C., Choi, J., Min, J. & Cho, K. Suppression of Oxidative Degradation of Tin–Lead Hybrid Organometal Halide Perovskite Solar Cells by Ag Doping. *ACS Energy Lett.* **5**, 3285–3294 (2020).
87. Bowman, A. R. *et al.* Microsecond Carrier Lifetimes, Controlled p-Doping, and Enhanced Air Stability in Low-Bandgap Metal Halide Perovskites. *ACS Energy Lett.* **4**, 2301–2307 (2019).
88. Li, M. *et al.* Pb-Sn-Cu Ternary Organometallic Halide Perovskite Solar Cells. *Adv. Mater.* **30**, 1800258 (2018).
89. Kobayashi, K., Hasegawa, H., Takahashi, Y., Harada, J. & Inabe, T. Electronic properties of tin iodide hybrid perovskites: effect of indium doping. *Mater. Chem. Front.* **2**, 1291–1295 (2018).
90. Zhang, X., Shen, J.-X., Turiansky, M. E. & Van De Walle, C. G. Hidden role of Bi incorporation in nonradiative recombination in methylammonium lead iodide. *J. Mater. Chem. A* **8**, 12964–12967 (2020).
91. Stoumpos, C. C., Malliakas, C. D. & Kanatzidis, M. G. Semiconducting Tin and Lead Iodide Perovskites with Organic Cations: Phase Transitions, High Mobilities, and Near-Infrared Photoluminescent Properties. *Inorg. Chem.* **52**, 9019–9038 (2013).
92. Thiesbrummel, J. *et al.* Universal Current Losses in Perovskite Solar Cells Due to Mobile Ions. *Adv. Energy Mater.* 2101447 (2021).
93. Savill, K. J. *et al.* Impact of Tin Fluoride Additive on the Properties of Mixed Tin-Lead Iodide Perovskite Semiconductors. *Adv. Funct. Mater.* **30**, 2005594 (2020).
94. Milot, R. L. *et al.* The Effects of Doping Density and Temperature on the Optoelectronic Properties of Formamidinium Tin Triiodide Thin Films. *Advanced Materials* **30**, 1804506 (2018).
95. Pena-Camargo, F. *et al.* Revealing the doping density in perovskite solar cells and its impact on device performance. *Applied Physics Reviews* (2022).
96. Lin, R. *et al.* Monolithic all-perovskite tandem solar cells with 24.8% efficiency exploiting comproportionation to suppress Sn(ii) oxidation in precursor ink. *Nat Energy* **4**, 864–873 (2019).

97. Baranowski, M. & Plochocka, P. Excitons in Metal-Halide Perovskites. *Advanced Energy Materials* **10**, 1903659 (2020).
98. Auger, P. Sur les rayons β secondaires produits dans un gaz par des rayons X. *C.R.A.S* **177**, 169–171 (1923).
99. Shen, J., Zhang, X., Das, S., Kioupakis, E. & Van De Walle, C. G. Unexpectedly Strong Auger Recombination in Halide Perovskites. *Advanced Energy Materials* **8**, 1801027 (2018).
100. Kirchartz, T., Márquez, J. A., Stolterfoht, M. & Unold, T. Photoluminescence-Based Characterization of Halide Perovskites for Photovoltaics. *Adv. Energy Mater.* **10**, 1904134 (2020).
101. Motti, S. G. *et al.* Photoinduced Emissive Trap States in Lead Halide Perovskite Semiconductors. *ACS Energy Lett.* **1**, 726–730 (2016).
102. Staub, F., Rau, U. & Kirchartz, T. Statistics of the Auger Recombination of Electrons and Holes via Defect Levels in the Band Gap—Application to Lead-Halide Perovskites. *ACS Omega* **3**, 8009–8016 (2018).
103. Das, B., Aguilera, I., Rau, U. & Kirchartz, T. What is a deep defect? Combining Shockley-Read-Hall statistics with multiphonon recombination theory. *Phys. Rev. Materials* **4**, 024602 (2020).
104. Hall, R. N. Electron-Hole Recombination in Germanium. *Phys. Rev.* **87**, 387–387 (1952).
105. Shockley, W. & Read, W. T. Statistics of the Recombinations of Holes and Electrons. *Phys. Rev.* **87**, 835–842 (1952).
106. Levenberg, K. A method for the solution of certain non-linear problems in least squares. *Quart. Appl. Math.* **2**, 164–168 (1944).
107. Marquardt, D. W. An Algorithm for Least-Squares Estimation of Nonlinear Parameters. *Journal of the Society for Industrial and Applied Mathematics* **11**, 431–441 (1963).
108. Endres, S. C., Sandrock, C. & Focke, W. W. shgo: Simplicial homology global optimisation.
109. Thacker, W. C. The role of the Hessian matrix in fitting models to measurements. *J. Geophys. Res.* **94**, 6177–6196 (1989).
110. Amini, A., Soleimany, A., Karaman, S. & Rus, D. Spatial Uncertainty Sampling for End-to-End Control (2019).
111. K. Hackenberger, B. Bayes or not Bayes, is this the question? *Croat Med J* **60**, 50–52 (2019).
112. Chopin, N. & Ridgway, J. Leave Pima Indians Alone: Binary Regression as a Benchmark for Bayesian Computation. *Statist. Sci.* **32**, (2017).
113. Metropolis, N., Rosenbluth, A. W., Rosenbluth, M. N., Teller, A. H. & Teller, E. Equation of State Calculations by Fast Computing Machines. *The Journal of Chemical Physics* **21**, 1087–1092 (1953).
114. Hastings, W. K. Monte Carlo Sampling Methods Using Markov Chains and Their Applications.
115. Skilling, J. Nested sampling for general Bayesian computation. *Bayesian Anal.* **1**, (2006).

116. Jeffreys, H. Some Tests of Significance, Treated by the Theory of Probability. *Math. Proc. Camb. Phil. Soc.* **31**, 203–222 (1935).
117. Kass, R. E. & Raftery, A. E. Bayes Factors. *Journal of the American Statistical Association* **90**, 773–795 (1995).

3 Methods

3.1 Sample fabrication

Preparation of perovskite precursor

In Chapters 4 and 5 of this thesis, a 'methylammonium (MA)-free' perovskite composition based on formamidinium (FA) is used, $FA_{0.83}Cs_{0.17}Pb_{0.5}Sn_{0.5}I_3$. Although MA-containing lead-tin perovskites are responsible for most record device efficiencies, they have been shown to be significantly less thermally stable than MA-free devices.[1] SnF_2 salt and Sn^0 powder additives are used to reduce Sn^{4+} species in the precursor solution and Sn^{2+} vacancies in the fresh films.[2,3] In Chapter 6 of this thesis, a MA-containing composition of $MA_{0.3}FA_{0.6}Cs_{0.1}Pb_{0.5}Sn_{0.5}I_3$ was used instead, synthesized by Dr. Shuaifeng Hu. Its synthesis is described in previous work.[4]

To make a 1.8M $FA_{0.83}Cs_{0.17}Pb_{0.5}Sn_{0.5}I_3$ perovskite precursor, FAI (1.49 mmol, Greatcellsolar), CsI (0.31 mmol, Alfa Aesar, 99.9%), PbI_2 (0.90 mmol, Thermo Fisher Scientific, ultra dry 99.999%), SnI_2 (0.90 mmol, Thermo Fisher Scientific, ultra dry 99.999%), SnF_2 (0.09 mmol, Aldrich, 99%), and metallic Sn powder (10 mg, Aldrich, 99.5%) were stirred in N,N-dimethylformamide (DMF) (0.800 ml, Sigma Aldrich, anhydrous) and dimethyl sulfoxide (DMSO) (0.200 ml, Sigma Aldrich, anhydrous) for 4 days at room temperature in a glovebox. Solutions were filtered with a 0.45 μm PTFE filter shortly before spincoating.

For the doping investigations in Chapter 5, BiI_3 (Thermo Fisher Scientific, Puratronic, 99.999%) and SbI_3 (Thermo Fisher Scientific, ultra dry 99.998%) dopants were dissolved in 4:1 DMSO:DMF to make stock solutions, which were added to the perovskite precursor 60 minutes before spincoating. The undoped control precursor was appropriately diluted with an

equal volume of DMF:DMSO to ensure concentrations of all precursor inks remained the same. For small concentrations of BiI_3 and SbI_3 doping, successive dilutions of doped precursor ink with undoped precursor ink were carried out. Solutions were filtered with a 0.45 μm PTFE filter shortly before spincoating.

Fabrication of films and devices

The samples used in Chapter 6 were fabricated by Shuaifeng Hu, and some of the samples used in Chapters 4 and 5 were fabricated by Heon Jin.

Glass or ITO substrates (Biotain, 10-15 Ω cm^{-2}) were cleaned by scrubbing with dishwashing soap, then sonicated for 10 min in 1 vol% Decon90 in DI water. Substrates were then rinsed with DI water and sonicated in DI water for 10 minutes, then sonicated in acetone and isopropyl alcohol (IPA) for 5 minutes each. Substrates were dried with N_2 and exposed to UV ozone for 10 minutes immediately before further processing.

For films deposited on glass or PTAA, a layer of Al_2O_3 nanoparticles was added to the substrate to improve wetting. Al_2O_3 nanoparticle suspension (90 μl, Sigma Aldrich, <50 nm, 20 wt% in IPA, diluted 1:150 in IPA) was deposited on the substrate by dynamic dropping during spinning at 5000 rpm for 30 s and subsequently dried for 2 minutes at 100 °C.

PEDOT:PSS (Heraeus, AL3083) was mixed with IPA in a 1:2 ratio and filtered with a 0.40 μm PVDF filter shortly before spin-coating. PEDOT:PSS solution (250 μl) was statically dropped and spread onto the ITO substrate, then spin-coated at 4000 rpm and 1333 acc for 30 s. Films were then annealed at 150 °C for 15 minutes in air, and a further 15 minutes in a nitrogen-filled glovebox. PTAA (Xi'an Polymer Light Corp, M_w 10,000-100,000 g mol^{-1}) in toluene (1.5 mg ml^{-1}) was stirred overnight to dissolve, then filtered with a 0.45 μm PTFE filter. PTAA was spin-coated onto ITO substrates in a nitrogen glovebox by dynamically dripping 150 μl solution onto the substrate at the start of a 6000 rpm, 1000 acc,

30 s spin-coating cycle. Films were then annealed at 100 °C for 10 min. To improve wetting on the PTAA surface, once the substrates had cooled Al_2O_3 nanoparticles were deposited as described above.

To deposit perovskite films, perovskite precursor (80 µl) was statically dropped and spread onto the substrate, then spun at 5000 rpm and 1000 acc for 60 s. Anisole (200 ul, anhydrous, Sigma-Aldrich) antisolvent was dropped onto the substrate after 30 s. The substrates were then annealed at 100 °C for 15 minutes.

For full device fabrication, the perovskite film was passivated with ethylenediammonium diiodide ($EDAI_2$). $EDAI_2$ (0.5 mg ml^{-1}, Merck) was stirred in 1:1 toluene:IPA for 4 days and subsequently filtered with a 0.45 µm PTFE filter. 80 µl of this solution was dropped onto the perovskite surface, and once the solution had spread to the edges of the film it was spun at 5000 rpm and 5000 acc for 20 seconds and annealed at 100 °C for 1 minute.

Phenyl-C61-butyric acid methyl ester (PCBM) (20 mg ml^{-1}, Ossila) was dissolved in 1:3 chlorobenzene:dichlorobenzene by stirring overnight, and filtered with a 0.45 µm PTFE filter. PCBM solution (80 µl) was dynamically deposited on the perovskite whilst spinning at 2000 rpm for 20 s and subsequently annealed at 100 °C for 3 minutes. Bathocuproine (BCP) (0.5 mg ml^{-1}, Xi'an Polymer Light Technology Corp) was dissolved in IPA by stirring for 4 days and filtered with a 0.45 µm PTFE filter. BCP solution (80 µl) was dynamically deposited on the perovskite whilst spinning at 5000 rpm for 30 s and subsequently annealed at 100 °C for 1 minute.

Finally, 3.5 nm Cr and 100 nm Au were sequentially thermally deposited onto the device (initial rate 0.02 nm s^{-1}, $\sim 10^{-7}$ Pa vacuum). Films and devices were not exposed to air at any point during the fabrication process. A complete device is shown in Figure 3.1.

Aging

Samples were encapsulated with a glass slide attached to the substrate with UV-activated epoxy which was cured for 3 minutes (Everlight Eversolar AB-341). For films, a recessed cavity glass with epoxy only deposited at the encapsulation edge was used to allow for optical measurements, and for devices the active area was fully covered by the epoxy. Before encapsulation, perovskite material was removed at the epoxy edge for optimal adhesion. Samples were aged in an ambient, illuminated aging chamber (Atlas Suntest XLS+) at 65 °C and simulated full spectrum sun light (76 mW cm^{-2}) irradiance under open circuit conditions. Before any measurement was performed, samples were removed from the aging environment and allowed to come to room temperate without direct illumination for 20 minutes. For XRD and SEM measurements of aged samples, the glass edges of the sample were cut to remove the encapsulation glass and epoxy. Films were removed from aging conditions 20 minutes before each measurement and allowed to cool to room temperature in dark conditions.

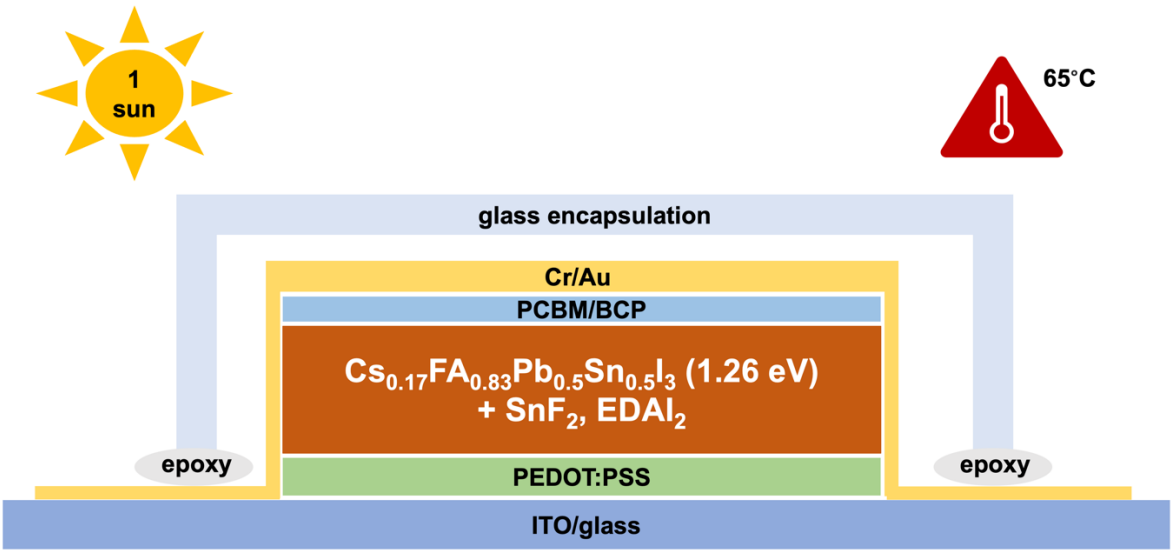


Figure 3.1. Schematic of a complete lead-tin MHP solar cell during stressing.

3.2 Photovoltaic device characterization

J-V measurements

The J-V characteristics of devices were measured under AM1.5G illumination (WaveLabs Sinus-220 solar simulator) with 100 mW cm^{-2} equivalent irradiance (certified by KG3-filtered Si reference photodiode). Voltage was swept from 0.9 V to - 0.2 V and back at a rate of 0.61 V s^{-1}. The device areas were defined by shadow masks, and each substrate contained 3 devices with an area of 0.25 cm^2 and one device with an area of 1.00 cm^2. For steady-state V_{oc} and J_{sc} measurements, devices were held at 0 V or V_{oc} for 30 s. For steady-state PCE measurements, an MPP tracker based on a gradient descent algorithm was employed to measure the maximum power for 60 s. A quasi-steady-state FF was calculated by dividing the product of V and J at the max power measured by the steady-state PCE measurement by the product of steady-state V_{oc} and J_{sc}.

External quantum efficiency measurements

The external quantum efficiency of our devices was determined using Fourier transform photocurrent spectroscopy. The custom-built set up is based on a Bruker Vertex 80 v Fourier transform interferometer. The solar cells were masked with a metal aperture such that the whole active area was illuminated by a tungsten halogen lamp. To determine the EQE, the photocurrent spectrum of the device under test was divided by that of a calibrated Si reference cell (Newport) of a known EQE. The acquisition time for each photocurrent spectrum was ~60 s.

To determine the equivalent short-circuit current density under 1 sun irradiance from the EQE measurements, the overlap integral of the AM1.5 photon flux ($\varphi_{AM1.5}$) spectrum with

the EQE was calculated. Explicitly, this is given by equation 3.1, where q is the elementary charge and λ is the wavelength.

$$J_{sc} = q\int_0^{\infty} d\lambda\, EQE(\lambda)\varphi_{AM1.5}(\lambda) \qquad (3.1)$$

Bandgaps were determined from EQE by plotting (E*EQE)^2 against E, then finding the point at which a linear fit to the EQE onset goes to 0.[5]

Variable rate J-V scanning/fast hysteresis measurements

To investigate the transient impact of mobile ions our devices, an in-house-built fast JV setup was used, shown in Figure 3.2. Akash Dasgupta assisted with these measurements.

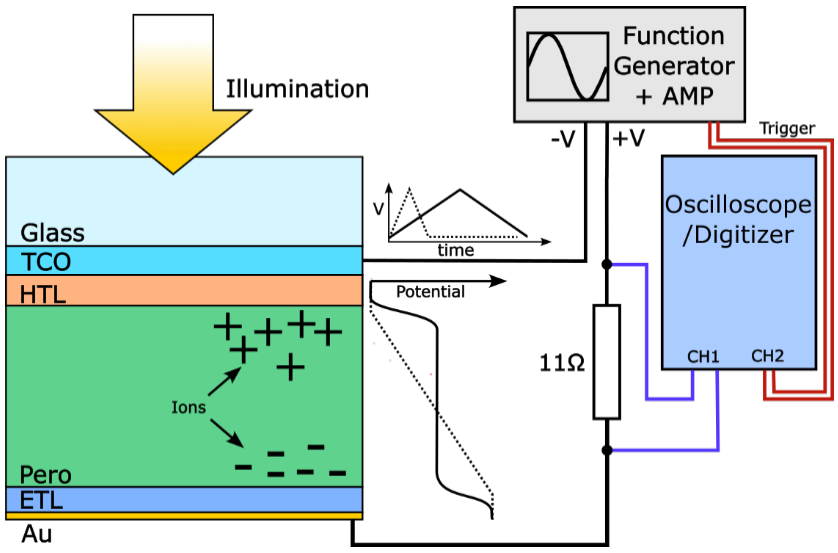


Figure 3.2. Schematic of fast J-V scan setup used. This figure was created by Akash Dasgupta.

The solar cell device was placed under 1 sum equivalent illumination provided by a Newport Class ABA LED Solar Simulator. The device was connected to a function generator (RSDG 1032X) coupled to a generic operational amplifier, with a 10 ohm resistor placed in series. The current was measured by measuring the potential drop across the resistor in series using a digitizer (Picoscope 204A). J-V curves were performed at scan rates between 0.2 ms -

7s s scan^{-1}. Devices were pre-biased at 1.1 V for 5 s, before scanning to – 0.2 V and back to 1.1 V at the specified rate. To reduce noise, 10 repeats for each scan rate were averaged, and the J-V curves were fit with a spline, from which J-V parameters (V_{oc}, J_{sc}, FF, PCE) were then extracted.

3.3 Structural & chemical material characterization

Optical microscope imaging

Samples were imaged in an optical microscope (Nikon Eclipse LV100ND) using a 20x objective in bright-field mode. Samples were illuminated from the bottom.

SEM and EDX measurements

SEM images were obtained with a FEI Quanta 600 FEG SEM using an accelerating voltage of 2, 5 or 20 kV as specified in the main text. Images were always collected on fresh areas to avoid degradation under to the electron beam. EDX-SEM maps were acquired with the same FEI Quanta 600 FEG SEM, operating at an accelerating voltage of 20 kV at a working distance of 10 mm. The total acquisition time was 7 minutes to minimise beam damage. Dr. Joel Smith assisted with the EDX measurements.

X-ray diffraction measurements

XRD measurements were performed on a Panalytical X'pert Pro XRD diffractometer using a Cu-k(alpha) radiation source with a wavelength of 1.54 eV and a generator voltage of 40 V and current of 40 mA. To track any effects related to oxidation during measurements, several successive scans were performed on each sample. During the 2.5-hour measurement

duration we in most cases did not observe formation of additional peaks, but did observe a very slight (< 0.1°) peak shift of the perovskite phase to lower angles, which can be explained by the formation of a slightly more FA- and Pb-rich primary phase as small amounts of Cs_2SnI_6 or δ-$CsSnI_3$ evolve from the initial perovskite composition (see section 4.2 for further detail).

Inductively Coupled Plasma Mass Spectrometry

Inductively coupled plasma mass spectrometry (ICP-MS) was carried out by two different labs, to enable measurement of all samples.

For FAI, CsI and PbI_2:

These measurements were carried out by collaborators Anika Sidler and Dr. Markus Lenz at the Institute for Ecopreneurship of the University of Applied Sciences and Arts Northwestern Switzerland. Concentration of impurities (Sb and Bi) in precursors was determined via triple-quadrupole inductively coupled plasma mass spectrometry (QqQ-ICP-MS). Briefly, FAI and CsI samples were dissolved in 3% HNO_3 (semiconductor grade). PbI_2 samples were dissolved in 3% HNO_3 (semiconductor grade), sonicated and then centrifuged and filtered (0.45 µm syringe filter; Infochroma AG, Goldau, Switzerland). Triplicates were used for each precursor. $^{115}In^+$, $^{121}Sb^+$ and $^{209}Bi^+$ were measured via 8800 QqQ-ICP-MS (Agilent, Basel, Switzerland) using general-purpose operational settings and helium as a collision gas (5 mL/min). Quantification was performed by external calibration from multi-element standard prepared in 3% HNO_3 from 0-50 µg/L and was considered appropriate if R^2>0.995. $^{103}Rh^+$ was monitored as an internal standard to account for possible matrix effects. The concentration of the analytes was further verified by external standard addition.

For SnI_2 A, SnI_2 B, Sn, SnF_2:

These measurements were carried out by collaborator Jayne Whitworth from the Materials Innovation Factory at the University of Liverpool. The concentration of impurities (Sb and Bi) in precursors was determined via inductively coupled plasma mass spectrometry (ICP-MS, Perkin Elmer NexION 2000). SnI_2 A, SnI_2 B, SnF_2, and Sn samples were dissolved in 2% HNO_3. Digestion was performed according to the parameters outlined in Table 3.1. As some solids persisted in the samples, digestion was performed again, after which any remaining solids (deemed insoluble in HNO_3) were filtered out. Triplicates were used for each precursor.

Table 3.1. Parameters used for sample digestion.

	T (°C)	p (bar)	Ramp	Hold	Power (%)
1	160	30	5	5	50
2	190	30	3	45	40
3	50	30	1	15	0

$^{121}Sb^+$ and $^{209}Bi^+$ were measured via Perkin Elmer NexION 2000 using helium as a collision gas. Quantification was performed by external calibration from multi-element standard prepared in 2% HNO_3 from 10-200 ppb and was considered appropriate if $R^2 >$ 0.995. A 2% HNO_3 blank sample was periodically analyzed, and no carry over was detected in these blanks. The blank raw intensities (0.000 ppm for Sb and 0.008 ppm for Bi) fell below the intensity of the lowest calibration point. Data which fell below the raw intensities of the lowest calibration point (10ppb) was discounted and displayed as “not detected”.

3.4 Optical & electronic material characterization

UV-vis absorption measurements

The total transmittance and total reflectance of encapsulated samples were measured in a Cary 5000 spectrophotometer using an internal diffuse reflectance accessory. Absorbance was calculated according to $A = -\ln(1 - T - R)$.

Photoluminescence Quantum Efficiency

Photoluminescence quantum efficiency (PLQE) of samples was determined according to the method of de Mello et al.[6] Samples were placed inside an integrating sphere and excited from the substrate side with a 657 nm continuous wave laser excitation source (Thorlabs) at 70.9 mW cm–2 (equivalent to one sun for a 1.25 eV bandgap) with a large spot size of 0.15 cm^2. The resulting PL signal was collected via a fibre bundle (Ocean Optics QR600 7 SR125BX) coupled with a spectrometer (QE Pro, Ocean Optics). Multiple different spots were normally measured on each substrate, as specified in the text. QFLS was calculated with the following equation, where $QFLS_{rad}$ is the radiative limit of QFLS when no non-radiative recombination takes place, k_B is the Boltzmann constant, and T the temperature.[7]

$$QFLS = QFLS_{rad} + k_B T\, ln(PLQE) \qquad (3.2)$$

A stray light correction was applied to recorded PL spectra by subtracting the spectrum of the excitation laser (attenuated to the correct intensity according to the fraction of laser absorbed by the sample for the highest excitation fluence used). Uncertainties were calculated by taking into account the noise floor of the detector, the Poisson noise from photon counting, and the uncertainty added by the stray light correction. Photoluminescence

emission spectra with a signal-to-noise ratio below 2 were not used, which corresponded to a noise floor of ~0.03% PLQE at a 1 sun illumination intensity. Additionally, the detector used was not able to effectively detect PL above 1050 nm, which means that for the 1.25 eV bandgap samples used here, we were only able to map slightly more than half of the PL emission peak. To correct this, we fit the PL measurements to a Gaussian function and used the resulting peaks to calculate PLQE (fits were only used if R^2 >0.8 was achieved).

Time-resolved Photoluminescence

Time-resolved photoluminescence (TRPL) measurements were collected by exciting samples from the substrate side with a 630 nm laser head (LDH-635, PicoQuant GmbH) with a spot size of 2.4 x 10^{-3} cm^2, pulsed at frequencies between 1-1000 kHz with fluences between 1-10 nJ cm^{-2} $pulse^{-1}$ (as specified in the text). The TRPL signal was collected from the same side with a time-correlated single photon counting (TCSPC) setup (FluoTime 300, PicoQuant GmbH using a TimeHarp260 for photon counting). Uncertainties were calculated by considering the noise floor of the detector and the Poisson noise from photon counting.

Where given, the monoexponential lifetimes were extracted as follows: The resulting data was normalized, and the tails of the resulting decays (>200 ns) were fit with a stretched mono-exponential decay. Fits were performed from 200 ns until the point in the decay where the signal-to-noise ratio fell below 2. For decays with lifetimes shorter than 200 ns, fits were performed on the 50 ns before the point in the decay where the signal-to-noise ratio fell below 2.

Where given, the differential lifetime was calculated by first smoothing data with a 5^{th}-order weighted polynomial spline. The differential lifetime was then calculated according to equation 3.3.[8]

$$\tau_{diff} = \left(-\frac{1}{2} \frac{dln(PL)}{dt} \right)^{-1} \qquad (3.3)$$

Time-resolved photoconductivity measurements

These measurements were performed by Dr. Manuel Kober-Czerny. Films were removed from aging conditions 20 minutes before each measurement and allowed to cool to room temperature in dark conditions. The method is detailed in recent work by Lim et al.[9] A Nd:YAG laser (Ekspla NT342A) excitation source tuned to a wavelength of 600 nm and pumped at 10 Hz with 3.74 ns pulses (full-width-half-maximum, FWHM) was used, attenuated by an optical density filter to achieve a range of fluences. This pulsed light illuminated the entire sample area of 0.25 cm^2 to uniformly excite the film from the substrate side. A photodetector (Thorlabs, FDS015) was used to detect the pulse source for the optical trigger for transient measurements using a digital oscilloscope. A small DC bias (<5 mV μm^{-1}, which is three orders of magnitude smaller than that for solar cell characterization, ~3 V μm^{-1}) was applied across the in-plane (lateral) electrodes, while the current was monitored by an oscilloscope. As the contact resistance between the perovskite film and Au electrode is fairly small compared to the sample resistance, we employed a two-wire conductivity measurement. A fixed resistor was put in series with the sample in the circuit to be <1% of the sample resistance. The voltage drop across the variable series resistor was monitored through a parallel oscilloscope (1 MΩ input impedance) to determine the potential drop across the two in-plane Au electrodes on the sample. The measured photo-conductivity value was obtained after 1 min illumination to minimize the time-dependent photo-doping (total measurement time for one sample is <5 minutes). Transient conductivity (σ) was calculated by the equation 3.4, where V_R is the monitored voltage drop through the

fixed resistor, R_R, V_{app} is the applied bias voltage, l is the channel-to-channel length, w is the channel width, and t is the film thickness. The dark conductivity was determined by taking the mean conductivity measured during the 320 ns before the light pulse.

$$\sigma = \frac{V_R}{R_R(V_{app} - V_R)} \cdot \frac{l}{wt} \qquad (3.4)$$

Significant recombination of photogenerated charges is expected to already take place during the length of the light pulse (3.74 ns). This was partially corrected for by fitting the photoconductivity decay to a mono-exponential decay and extrapolating this back to the beginning of the pulse (t_0) to determine the maximum photoconductivity reached. However, higher-order recombination as well as diffusion- and trap filling-related processes are also expected to take place during the pulse duration, which was not corrected for here. Hence the photoconductivity and the sum of mobilities determined should be understood as lower bounds.

Ultra-sensitive External Quantum Efficiency

Ultra-sensitive external quantum efficiency (EQE) measurements were conducted by collaborators Dr. Stefan Zeiske and Dr. Ardalan Armin at Swansea University, on non-encapsulated perovskite films on glass with various densities of Bi^{3+} doping. To enable electrical measurements, gold photoresistor electrodes were evaporated on top of the samples. A spectrophotometer (Perkin Elmer, Lambda 950) was used as a light source. The probe light was physically chopped at 273 Hz (Thorlabs MC2000B) and guided on the device under test (DUT) using different optical components. Prior analyzing the DUT response with a lock-in amplifier, the photocurrent was fedged through a current pre-amplifier with variable gain and low-noise voltage source (Femto, DLPCA-200). Details to the EQE setup are provided elsewhere.[10] The DUTs were mounted in an electrically shielded (Faraday cage-like) sample

holder from Linkam; the DUTs in the sample holder were kept under dry nitrogen-circulation. EQE measurements were conducted at -10 V applied bias voltage using the Femto current pre-amplifier; an electrical bandwidth of 1 mHz was used. Furthermore, a 975 nm optical density (OD) 4.0 longpass filter was placed into the light path for low-photon energy (i.e., at photon energies well below the bandgap) measurements to further reduce the (optical) noise.

3.5 Simulations & Fitting

J-V scan simulations

J-V curve simulations were carried out using both the IonMonger[11] and the SCAPS-1D (v 3310)[12] drift diffusion packages. The full list of the parameters used (when not varied) is given in the Appendix. The generation profile used was calculated using a transfer matrix optical model, adjusted to match the short circuit current measured.

DFT calculations

DFT calculations were carried out by collaborators Dr. Daniele Meggiolario at the Istituto CNR di Scienze e Tecnologie Chimiche (SCITEC-CNR) in Perugia, and Dr. Luca Gregori at the University of Perugia. They have been conducted in the 2x2x2 supercell of the tetragonal $MAPb_{0.5}Sn_{0.5}I_3$ phase by using the Quantum Espresso software package.[13] The equilibrium structure of defects have been found by relaxing the lattice by using the Perdew-Burke-Ernzherof (PBE) functional and by including DFT-D3 dispersion corrections,[14] keeping cell parameters fixed to the experimental values.[15] DFT calculations in supercells have been carried out at the Γ point in the Brillouin zone by using norm-conserving

pseudopotentials[16,17] with a cutoff on the wavefunctions of 60 Ry. Defect quantities have been refined by using the PBE0 functional[18,19] with a decreased fraction of exact exchange α = 0.20, by including spin-orbit coupling corrections (SOC) and DFT-D3 dispersions. By using the PBE0 functional (α = 0.20) and including SOC a band gap of 1.29 eV has been obtained for the $MAPb_{0.5}Sn_{0.5}I_3$ phase, nicely matching the experimental value. Hybrid-SOC calculations have been conducted by using the same methodology employed for PBE calculations, by reducing exact exchange cutoff to 60 Ry to reduce the computational effort. Defect formation energies and thermodynamic ionization levels $\boldsymbol{\varepsilon}$ have been calculated according to the following equations, where $E(X^q)$ is the energy of the supercell containing defect X, E(perf) is the energy of the non-defective system, n and μ are, respectively, the number and the chemical potentials of the species added or subtracted to the non-defective system to form a defect; q is the charge of the defect.[20]

$$DFE\ [X^q] = E[X^q] - E[perf] - \sum_i n_i\mu_i + q(\varepsilon_{VB} + \varepsilon_F) + E^q_{corr} \qquad (3.5)$$

$$\varepsilon(q/q') = \frac{E[X^q] - E[X^{q'}]}{q' - q} + \frac{E^q_{corr} - E^{q'}_{corr}}{q' - q} - \varepsilon_{VB} \qquad (3.6)$$

Long-range electrostatic interactions E^q_{corr} have been corrected through the Makov-Payne scheme by using the ionic dielectric permittivity of $MAPbI_3$ (ε=25).

The chemical potentials of the atomic species have been set in order to simulate I-rich, I-medium, and I-poor conditions of growth, under the constraint of the thermodynamic stability of the $MAPb_{0.5}Sn_{0.5}I_3$ phase. In I-rich conditions the following values of the chemical potentials have been used $\mu(I) = (\mu(SnI_4) - \mu(SnI_2))/2$ = -0.17 eV *vs* I_2^{solid} ; $\mu(Sn) = \mu(SnI_2) - 2\mu(I)$ = -1.40 eV *vs* $\mu(Sn_{bulk})$; $\mu(Pb) = \mu(PbI_2) - 2\mu(I)$ = -1.58 eV *vs* $\mu(Pb_{bulk})$. In I-poor conditions $\mu(I) = (\mu(SnI_2) - \mu(Sn_{bulk}))/2$ = -0.87 eV *vs* I_2^{solid} ; $\mu(Sn) = \mu(Sn_{bulk})$ = 0.0 eV *vs*

$\mu(Sn_{bulk})$; $\mu(Pb) = \mu(PbI_2) - 2\mu(I) = -0.18$ eV *vs* $\mu(Pb_{bulk})$. For I-medium conditions intermediate chemical potentials between I-rich and I-poor have been used. The chemical potentials of the Bi and Sb dopants have been calculated by considering the stability limit of the respective trivalent Bi/SbI_3 salts, i.e. μ (Bi/Sb) = μ (Bi/SbI_3) – 3 μ (I). The energy of the phases has been evaluated at the experimental crystal structures.[11]

TRPL and PLQE modelling

Changes in carrier density in space and over time after illumination were simulated using the system of equations given in section 2.4, where these processes are also explained in detail. The processes of 1D diffusion, Auger recombination, bimolecular radiative recombination, and trap-assisted non-radiative recombination were simulated. Simulations were performed with up to two traps, with a separate ODE for each trap occupancy. Numba was used to speed up computation. When spatial resolution was used, 20 slices were used in the model.

To simulate a TRPL decay, the system of ODEs was solved using the LSODA solver with initial carrier densities n_0, p_0 and all traps unpopulated. If some free or trapped charge carrier densities were found to not decay to their original values at the end of the TRPL measurement window, the ODEs were solved again with the new initial carrier condition given by the carrier densities at the end of the decay. The TRPL decay was simulated with the obtained electron and hole densities (equation 3.7).

$$TRPL\ (t) = \Sigma_x\ k_{rad,ext} n(x,t) p(x,t) \qquad (3.7)$$

To simulate PLQE, the simultaneous system of equations 3.8 was solved for steady-state carrier densities n(x) and p(x). The trap-assisted non-radiative recombination rate and external PLQE were then calculated as in equations 3.9, 3.10.

$$\frac{dn}{dt}(x,t) = 0 \qquad n - n_0 + n_{trapped} = p - p_0 + p_{trapped} \tag{3.8}$$

$$R_{SRH} = \Sigma_i \frac{N_{t,i}\beta_{n,i}\beta_{p,i}(np - n_0p_0)}{(n + N_C e^{\frac{E_{T,i}-E_{CB}}{kT}})\beta_{n,i} + (p + N_V e^{\frac{E_{CB}-E_{T,i}}{kT}})\beta_{p,i}} \tag{3.9}$$

$$PLQE = \frac{\Sigma_x R_{rad}(x)}{\Sigma_x R_{aug}(x) + R_{rad}(x) + R_{SRH}(x)} \tag{3.10}$$

Table 3.2. Parameter names and values used in simulations, when not varied.

Parameter	**Symbol**	**Units**	**Value**
Fermi level	E_F	eV	0.25
Conduction band/valence band energy	E_{CB}, E_{VB}	eV	0, 1.25
Conduction band/valence band density of states	N_C, N_V	cm^{-3}	6.98×10^{18}, 2.49×10^{18}
Effective mass of electron/hole	m_e, m_h	-	0.2, 0.2
Excitation fluence	P_{exc}	cm^{-3}	var
Absorbance coefficient at laser wavelength	α	cm	6.4×10^6
Electron/hole mobility	$\mu_{n/p}$	$cm^2V^{-1}s^{-1}$	1
Auger recombination coefficient	$k_{aug,n/p}$	cm^6s^{-1}	1×10^{-28}
Internal radiative band-to-band recombination coefficient	$k_{rad,int}$	cm^3s^{-1}	1×10^{-10}
Probability of reabsorption	p_r	-	0.95

In Chapter 5, TRPL and PLQE measurements of control films were replicated with a single electron trap with an energy level 0.3 eV from the CB, a density of 1.6 x 10^{15} cm^{-3}, and symmetrical electron and hole capture coefficients of 10^{-9} cm^3s^{-1}.

Bayesian inference by dynamic nested sampling

The 'dynesty' package developed by Speagle and Koposov[21,22] in Python was used to perform Nested Sampling for Bayesian inference and evidence estimation (developed by Skilling).[23,24] This package further allows for 'Dynamic Nested Sampling', in which samples are added after the completion of nested sampling to improve the accuracy of posterior determination.[25] The random slice sampling algorithm was used to select the next set of parameters at which to sample.[26–28] Multiple ellipsoid bounding was used to condition this sampling method.[29] This bounding allows for the resolution of multimodal posterior distributions, if these are present. 518 live points were 'active' at every time during nested sampling, which set the resolution with which the algorithm integrates over the parameter space. Nested sampling was stopped when the change in the ln of the evidence (dlnZ) fell below 0.5. Dynamic sampling was stopped according to dynesty's default stopped function. Parallelization was used to speed up computation.

3.6 Works Cited

1. Wu, P. *et al.* Efficient and Thermally Stable All-Perovskite Tandem Solar Cells Using All-FA Narrow-Bandgap Perovskite and Metal-oxide-based Tunnel Junction. *Advanced Energy Materials* **12**, 2202948 (2022).
2. Pascual, J. *et al.* Fluoride Chemistry in Tin Halide Perovskites. *Angew. Chem. Int. Ed.* anie.202107599 (2021).
3. Lin, R. *et al.* Monolithic all-perovskite tandem solar cells with 24.8% efficiency exploiting comproportionation to suppress Sn(ii) oxidation in precursor ink. *Nat Energy* **4**, 864–873 (2019).
4. Hu, S. *et al.* Optimized carrier extraction at interfaces for 23.6% efficient tin–lead perovskite solar cells. *Energy Environ. Sci.* **15**, 2096–2107 (2022).
5. Carron, R. *et al.* Bandgap of thin film solar cell absorbers: A comparison of various determination methods. *Thin Solid Films* **669**, 482–486 (2019).
6. de Mello, J. C., Wittmann, H. F. & Friend, R. H. An improved experimental determination of external photoluminescence quantum efficiency. *Adv. Mater.* **9**, 230–232 (1997).
7. Caprioglio, P. *et al.* On the Relation between the Open-Circuit Voltage and Quasi-Fermi Level Splitting in Efficient Perovskite Solar Cells. *Adv. Energy Mater.* **9**, 1901631 (2019).
8. Krückemeier, L., Krogmeier, B., Liu, Z., Rau, U. & Kirchartz, T. Understanding Transient Photoluminescence in Halide Perovskite Layer Stacks and Solar Cells. *Advanced Energy Materials* **11**, 2003489 (2021).
9. Lim, J. *et al.* Long-range charge carrier mobility in metal halide perovskite thin-films and single crystals via transient photo-conductivity. *Nat Commun* **13**, 4201 (2022).
10. Zeiske, S., Kaiser, C., Meredith, P. & Armin, A. Sensitivity of Sub-Bandgap External Quantum Efficiency Measurements of Solar Cells under Electrical and Light Bias. *ACS Photonics* **7**, 256–264 (2020).
11. Courtier, N. E., Cave, J. M., Walker, A. B., Richardson, G. & Foster, J. M. IonMonger: a free and fast planar perovskite solar cell simulator with coupled ion vacancy and charge carrier dynamics. *J Comput Electron* **18**, 1435–1449 (2019).
12. Burgelman, M., Nollet, P. & Degrave, S. Modelling polycrystalline semiconductor solar cells. *Thin Solid Films* **361–362**, 527–532 (2000).
13. Giannozzi, P. *et al.* QUANTUM ESPRESSO: a modular and open-source software project for quantum simulations of materials. *J. Phys.: Condens. Matter* **21**, 395502 (2009).
14. Grimme, S., Antony, J., Ehrlich, S. & Krieg, H. A consistent and accurate *ab initio* parametrization of density functional dispersion correction (DFT-D) for the 94 elements H-Pu. *The Journal of Chemical Physics* **132**, 154104 (2010).
15. Stoumpos, C. C., Malliakas, C. D. & Kanatzidis, M. G. Semiconducting Tin and Lead Iodide Perovskites with Organic Cations: Phase Transitions, High Mobilities, and Near-Infrared Photoluminescent Properties. *Inorg. Chem.* **52**, 9019–9038 (2013).

16. Hamann, D. R., Schlüter, M. & Chiang, C. Norm-Conserving Pseudopotentials. *Phys. Rev. Lett.* **43**, 1494–1497 (1979).
17. Van Setten, M. J. *et al.* The PseudoDojo: Training and grading a 85 element optimized norm-conserving pseudopotential table. *Computer Physics Communications* **226**, 39–54 (2018).
18. Adamo, C. & Barone, V. Toward reliable density functional methods without adjustable parameters: The PBE0 model. *The Journal of Chemical Physics* **110**, 6158–6170 (1999).
19. Perdew, J. P., Ernzerhof, M. & Burke, K. Rationale for mixing exact exchange with density functional approximations. *The Journal of Chemical Physics* **105**, 9982–9985 (1996).
20. Van De Walle, C. G. & Neugebauer, J. First-principles calculations for defects and impurities: Applications to III-nitrides. *Journal of Applied Physics* **95**, 3851–3879 (2004).
21. Speagle, J. S. dynesty: a dynamic nested sampling package for estimating Bayesian posteriors and evidences. *Monthly Notices of the Royal Astronomical Society* **493**, 3132–3158 (2020).
22. Sergey Koposov *et al.* joshspeagle/dynesty: v2.1.4. Zenodo (2024).
23. Skilling, J. Nested Sampling. in *AIP Conference Proceedings* vol. 735 395–405 (AIP, Garching (Germany), 2004).
24. Skilling, J. Nested sampling for general Bayesian computation. *Bayesian Anal.* **1**, (2006).
25. Higson, E., Handley, W., Hobson, M. & Lasenby, A. Dynamic nested sampling: an improved algorithm for parameter estimation and evidence calculation. *Stat Comput* **29**, 891–913 (2019).
26. Neal, R. M. Slice sampling. *Ann. Statist.* **31**, (2003).
27. Handley, W. J., Hobson, M. P. & Lasenby, A. N. POLYCHORD : nested sampling for cosmology. *Monthly Notices of the Royal Astronomical Society: Letters* **450**, L61–L65 (2015).
28. Handley, W. J., Hobson, M. P. & Lasenby, A. N. polychord: next-generation nested sampling. *Mon. Not. R. Astron. Soc.* **453**, 4385–4399 (2015).
29. Feroz, F., Hobson, M. P. & Bridges, M. MultiNest: an efficient and robust Bayesian inference tool for cosmology and particle physics. *Monthly Notices of the Royal Astronomical Society* **398**, 1601–1614 (2009).

4 Stability of lead-tin perovskites

4.1 Overview

Efficiencies of lead-tin perovskite-based devices now exceed 23% in single junction devices,[1] 28.5% in all-perovskite double junctions,[2] and 24.3% in triple junctions,[3] but reports of high stability under operating conditions remain rare. The development of more stable lead-tin perovskite absorber layers and device stacks is hence essential for the realization of field-deployable all-perovskite tandems.

It remains unclear which factors ultimately limit device stability, and whether these are inherent to the lead-tin perovskite material itself or stem from another aspect of the device. In this chapter, this question is addressed by disentangling the degradation occurring in various components in the device stack as well as in fully fabricated solar cells. The evolving properties of lead-tin perovskite films and devices are investigated during encapsulated aging under combined light and thermal stressing.

In the case of the isolated lead-tin perovskite absorber layer, changes in morphology and phase purity only become significant after thousands of hours of aging under simulated sun light at 65 °C. While the absorber layer is found to be structurally stable over hundreds of hours of aging, the corresponding photocurrent generated from solar cells degrades significantly during this time. This rapid device degradation is attributed to largely be the result of increased losses induced by the bias-induced accumulation of rapid-moving ions at interfaces during device operation, highlighting an important future focus for research aiming to enable long-term stable lead-tin perovskite solar cells. Whilst the magnitude of this mobile ion-induced loss can be greatly reduced by selecting an alternative HTL to PEDOT:PSS, replacing PEDOT:PSS induces new losses during aging which stem from increased self-p-doping. These differences are explained by considering the chemical interaction between

PEDOT:PSS and the perovskite. The impact of each of these factors on device performance over time is quantified, revealing the most relevant degradation pathways for each architecture. Based on this, recommendations for future stability optimization are made.

4.2 Structural and morphological changes during aging

First, structural changes that occur in the bulk perovskite absorber layers during aging when deposited either on glass or in 'half-stacks' of ITO/HTL/perovskite were investigated. Films and devices were encapsulated with UV-cured epoxy and glass cover slips and aged at elevated temperatures (65 °C) and illumination (0.76 suns equivalent from a AM1.5 xenon lamp aging box) in an ambient environment (ISOS L-2 conditions[4]). Throughout this chapter, these stressing conditions are referred to simply as 'aging' for simplicity.

To characterize crystallographic changes in the films during aging, X-ray diffraction (XRD) measurements were performed on lead-tin perovskite films on glass or HTLs (Figure 4.1). All XRD patterns can be fit to a pseudo-cubic perovskite structure, both before and after 2000 hours of aging. New XRD peaks emerge in the aged films and can be assigned to a single degradation product, which can be identified as the orthorhombic yellow δ-$CsSnI_3$ or δ-$CsPbI_3$ phase.[5,6] This phase appears in perovskite aged on glass (unencapsulated, aged in N_2), on ITO/PEDOT:PSS and on ITO/poly(bis(4-phenyl)(2,4,6-trimethylphenyl)amine) (PTAA) half-stacks (encapsulated, aged in ambient conditions) (Figure 4.1).

When the perovskite films are not encapsulated and rather exposed directly to ambient conditions, we instead detect Cs_2SnI_6 after only a few hours of air exposure, even without exposure to light and heat (Figure 4.1). Cs_2SnI_6 has been previously observed by others in lead-tin perovskites exposed to air,[7] and can be spontaneously formed from δ-$CsSnI_3$ under ambient conditions at room temperature.[8] Since Cs_2SnI_6 was not detected in any of the aged,

encapsulated samples, it can be inferred that the encapsulation successfully inhibits the formation of large amounts of Sn^{4+} within these films during prolonged aging.

XRD measurements were then performed on complete devices with an ITO/PEDOT:PSS/ $FA_{0.83}Cs_{0.17}Pb_{0.5}Sn_{0.5}I_3$/ethylenediammonium diiodide ($EDAI_2$)/phenyl-C61-butyric acid methyl ester (PCBM)/bathocuproine (BCP)/Cr/Au architecture which had been aged for 627 hours, to check whether the perovskite absorber layers in devices degrade in the same way as the films on glass and half-stacks on HTLs (Figure 4.1a). New peaks appearing at 2θ values of 12.8° and 53.5° can be ascribed to PbI_2, and other new peaks at 13.2° and 26.5° can be ascribed to either δ-$CsSnI_3$/δ-$CsPbI_3$ or Cs_2SnI_6. Despite the appearance of these degradation products, the relative peak intensity and width of the original perovskite phase does not change significantly, indicating that the perovskite bulk is left largely intact during 600+ hours of device aging. However, the data does show a slight expansion in the cubic lattice volume of the main perovskite phase during aging, for films on glass, HTLs and complete devices (Table 4.1). This would be consistent with the formation of a slightly more FA- and Pb-rich primary phase as δ-$CsSnI_3$ or Cs_2SnI_6 evolve from the initial perovskite composition.

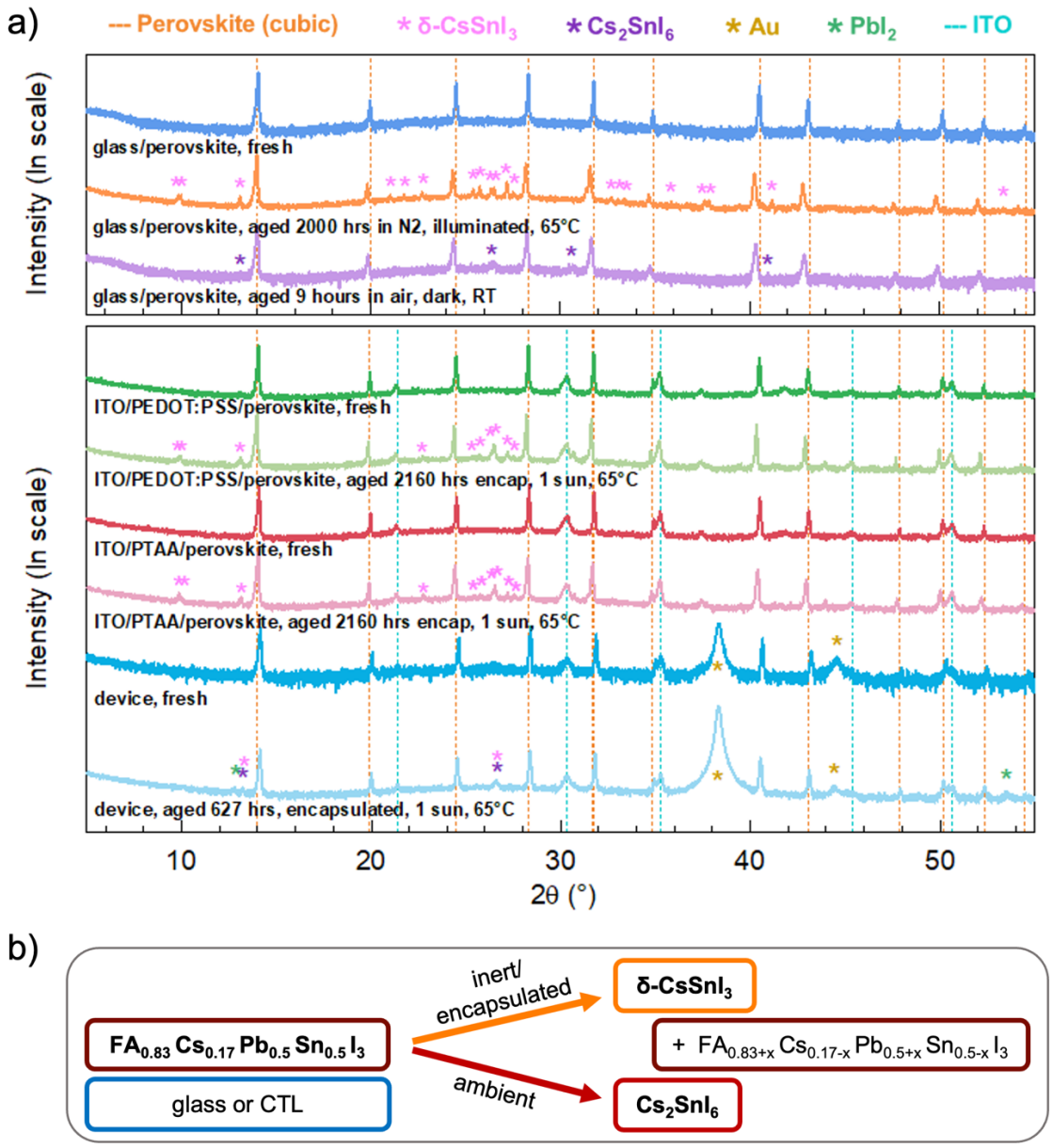


Figure 4.1. XRD measurements of $FA_{0.83}Cs_{0.17}Pb_{0.5}Sn_{0.5}I_3$ films deposited on glass or ITO/HTLs, and ITO/PEDOT:PSS/$FA_{0.83}Cs_{0.17}Pb_{0.5}Sn_{0.5}I_3$/PCBM/BCP/Cr/Au devices, aged at 65 °C and simulated full spectrum sun light (76 mW cm^{-2}) irradiance for various periods of time under ambient, ambient encapsulated, or N_2 conditions at open circuit. Films that were encapsulated during aging were measured by cutting the glass edges of the sample to remove the encapsulation glass and epoxy. b) Schematic of degradation phase formation observed in $FA_{0.83}Cs_{0.17}Pb_{0.5}Sn_{0.5}I_3$ upon aging in inert and ambient atmospheres.

Table 4.1. Unit cell volume of the cubic perovskite cell fitted to PbSn-perovskite films and device before and after aging at 65 °C and simulated full spectrum sun light (76 mW cm^{-2}) irradiance from XRD measurements shown in Figure 4.1a.

Stack *(aging condition)*	**Unit cell volume before aging [Å^3]**	**Unit cell volume after aging (aging time) [Å^3]**
ITO/PEDOT:PSS/ $FA_{0.83}Cs_{0.17}Pb_{0.5}Sn_{0.5}I_3$/PCBM/BCP/Cr/Au *(encapsulated, 65°C, 0.76 suns)*	**248.76**	**250.28** (627 hours)
ITO/PEDOT:PSS/ $FA_{0.83}Cs_{0.17}Pb_{0.5}Sn_{0.5}I_3$ *(encapsulated, 65°C, 0.76 suns)*	**250.18**	**252.58** (2160 hours)
ITO/PTAA/Al_2O_3 NPs/ $FA_{0.83}Cs_{0.17}Pb_{0.5}Sn_{0.5}I_3$ *(encapsulated, 65°C, 0.76 suns)*	**250.39**	**252.23** (2160 hours)
Glass/Al_2O_3 NPs/ $FA_{0.83}Cs_{0.17}Pb_{0.5}Sn_{0.5}I_3$ *(unencapsulated ambient, room temperature)*	**250.16**	**253.05** (9 hours in air)
Glass/Al_2O_3 NPs/ $FA_{0.83}Cs_{0.17}Pb_{0.5}Sn_{0.5}I_3$ *(unencapsulated in N_2, 65°C, 0.76 suns)*	**250.39**	**254.39** (2000 hours)

Next, the morphological qualities of films of lead-tin perovskite deposited on glass and on HTLs were examined during aging. Fresh films appear smooth and homogenous in both optical microscope (OM) and scanning electron microscope (SEM) images. However, after long periods of aging (2000+ hours) one can observe by OM bright yellow regions a few micrometers in size (Figure 4.2a). SEM images reveal that the polycrystalline form of the perovskite has changed in these regions, being composed of smaller crystalline domains than the remaining perovskite bulk. These new crystallites start to become visible on the surface of perovskite films after ~1000 hours of aging (Figure 4.2b), although it is possible that small regions begin to form away from the surface of the film before this time. The emergence of these features is also observed in OM images of aged lead-tin perovskite films deposited on

ITO/PEDOT:PSS and ITO/PTAA after ~1000 hours of aging, where the regions appear larger when PEDOT:PSS is used as the underlying layer (Figure 4.2c).

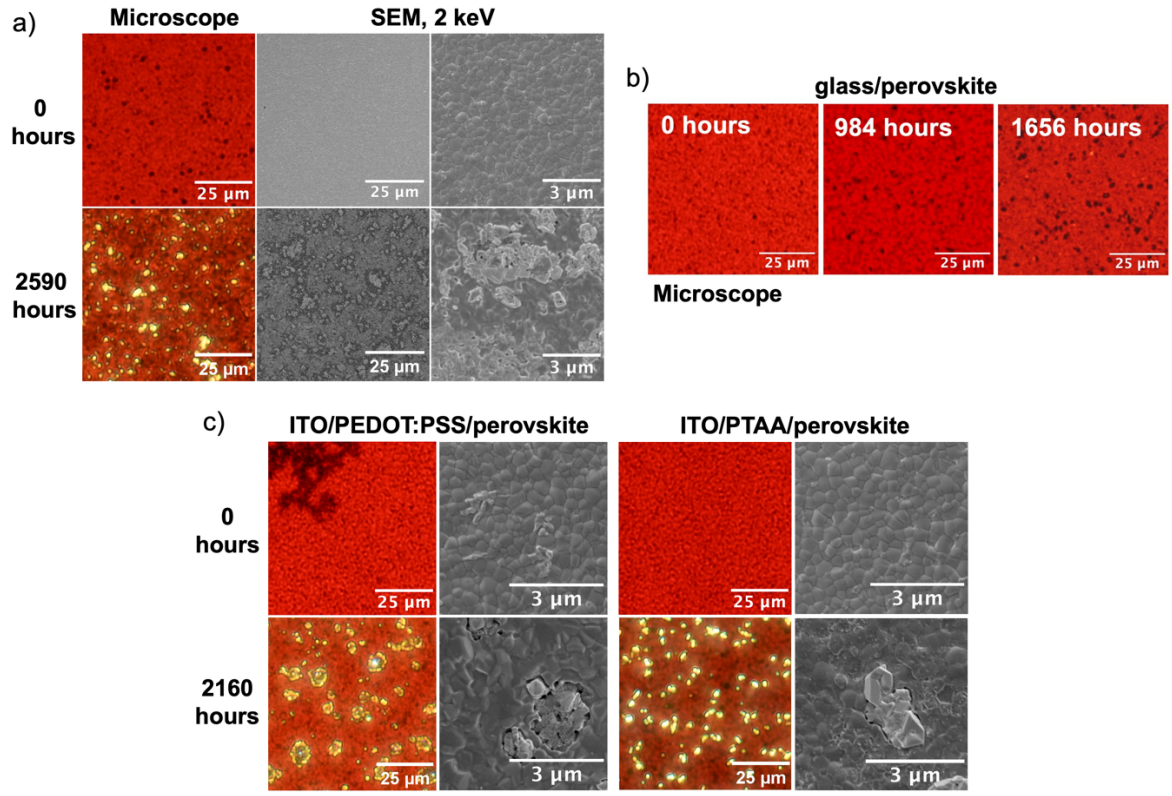


Figure 4.2. Optical microscope (OM) or scanning electron microscope (SEM) images of the surface of lead-tin perovskite films deposited on a), b) glass and c) ITO/PEDOT:PSS or ITO/PTAA/Al2O3 NPs. Images show evolution at various times during encapsulated aging under 65 °C and simulated full spectrum sun light (76 mW cm-2) irradiance. OM images were taken with diascopic illumination and SEM images were acquired with a 2 kV accelerating voltage.

To confirm the chemical identity of these regions, spatially resolved energy-disperse X-ray scanning electron microscopy (EDX-SEM) imaging was performed, and the resulting elemental maps are shown in Figure 4.3. EDX indicates that a higher density of Cs and Sn is present within the new crystallites as compared to the rest of the film, whilst the Pb density is similar between the crystallites and the background (Figure 4.3g). Identifying these regions as δ-$CsSnI_3$ would also be consistent with the observations of increased transmittance of light through these regions made by OM, as δ-$CsSnI_3$ has a very wide optical bandgap of 2.55 eV,[6]

whilst δ-$CsPbI_3$ has a bandgap of 1.7 eV.[9] Hence, there is significant evidence that the observed new crystallites are the δ-$CsSnI_3$ phase detected by XRD measurements.

The strongest contrast between the bulk and the new crystallites was observed at a low imaging voltage of 2 keV. Significant Z-contrast between $FA_{0.83}Cs_{0.17}Pb_{0.5}Sn_{0.5}I_3$ and δ-$CsSnI_3$ is not expected at normal accelerating voltages of 5-20 keV due to similar electron backscattering coefficients (η = 0.433 and 0.423, respectively, calculated as in Goldstein et al.[10]). The stronger contrast between the bulk and the new crystallites observed at the lower voltage of 2 keV may hence be due to topography or local compositional differences on the surface.[10] The darker appearance of the perovskite around these grains in SEM images under low accelerating voltages could suggest a difference in surface composition or roughness.

The new crystallites also contain a slightly increased density of iodine. It is possible that some other degradation products such as I_2, SnI_2 or SnI_4 also form in these regions, but any crystalline domains of these other possible impurities are too small to be detected by XRD.

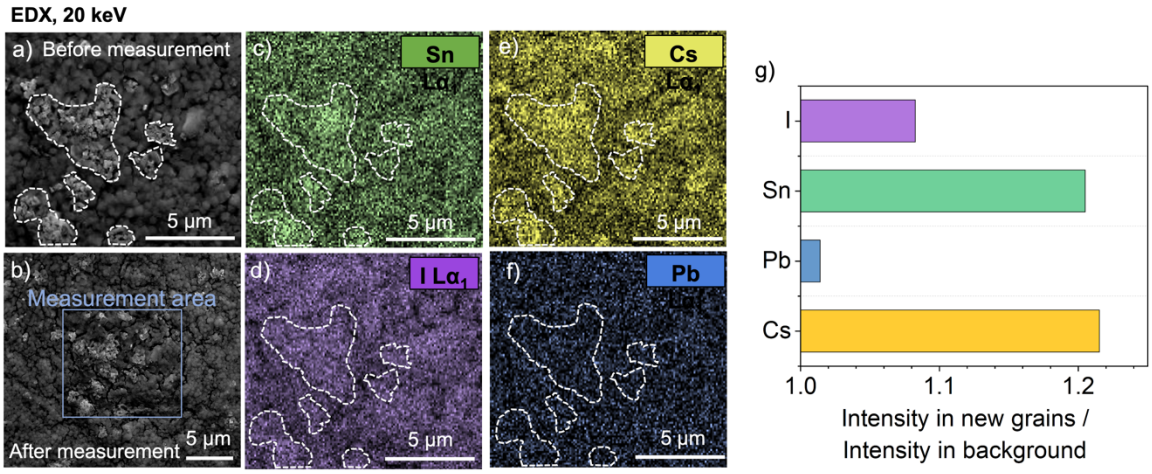


Figure 4.3. Energy-dispersive X-ray scanning electron microscopy (EDX-SEM) analysis of the surface of lead-tin perovskite films on glass, after 2592 hours of encapsulated aging under 65 °C and simulated full spectrum sun light (76 mW cm^{-2}) irradiance. a) SEM image of the area prior to measurement (new crystallites are marked with white dashed lines) and b) after 7 minutes of measurement, showing some grain boundary decomposition but no heavy degradation. Elemental maps

using the Lα1 spectral line for c) Sn, d) I, e) Cs and f) Pb, with a 5 µm scalebar. g) Ratio of mean EDX signal intensity measured within new crystallites (yellow lines) to mean signal intensity in background.

Additionally, since δ-$CsSnI_3$ has a significantly higher density (4.82 g cm^{-3})[6] than the lead-tin perovskite (3.87 g cm^{-3} for $MAPb_{0.54}Sn_{0.46}I_3$),[11] its formation within the film is expected to be accompanied by significant strain leading to void formation. SEM imaging of cross-sections of aged devices confirms this – after 627 hours of aging, we observe voids filled with smaller crystallites in the active layer of aged devices (Figure 4.4), which are not observed in fresh devices.

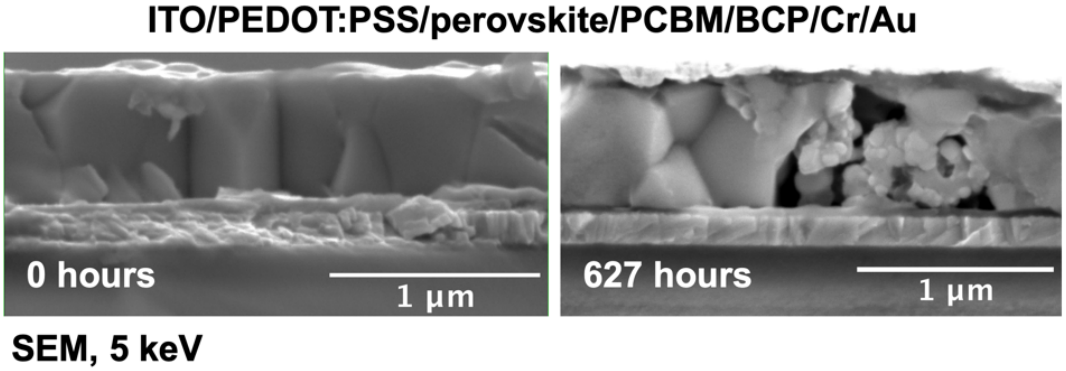


Figure 4.4. SEM image of a cross-section of the lead-tin perovskite absorber layer inside a device, fresh and after encapsulated aging under 65 °C and simulated full spectrum sun light (76 mW cm^{-2}) irradiance for 627 hours. Image was acquired with a 5 kV accelerating voltage.

Despite the slow evolution of these degradation products, the original lead-tin perovskite phase remains stable over long periods of light stressing at elevated temperature, even in half-stacks with HTLs or in complete devices. In agreement with this, the EQE of aged devices showed no significant change in photovoltaic bandgap during the first ~300 hours of aging (Figure 4.5a,b) and the absorption onset of films on glass changes only very slightly over hundreds to thousands of hours of aging (Figure 4.5c). However, as

smaller-scale degradation processes could be occurring on faster timescales, I next investigate how the optoelectronic properties of the perovskite change during aging.

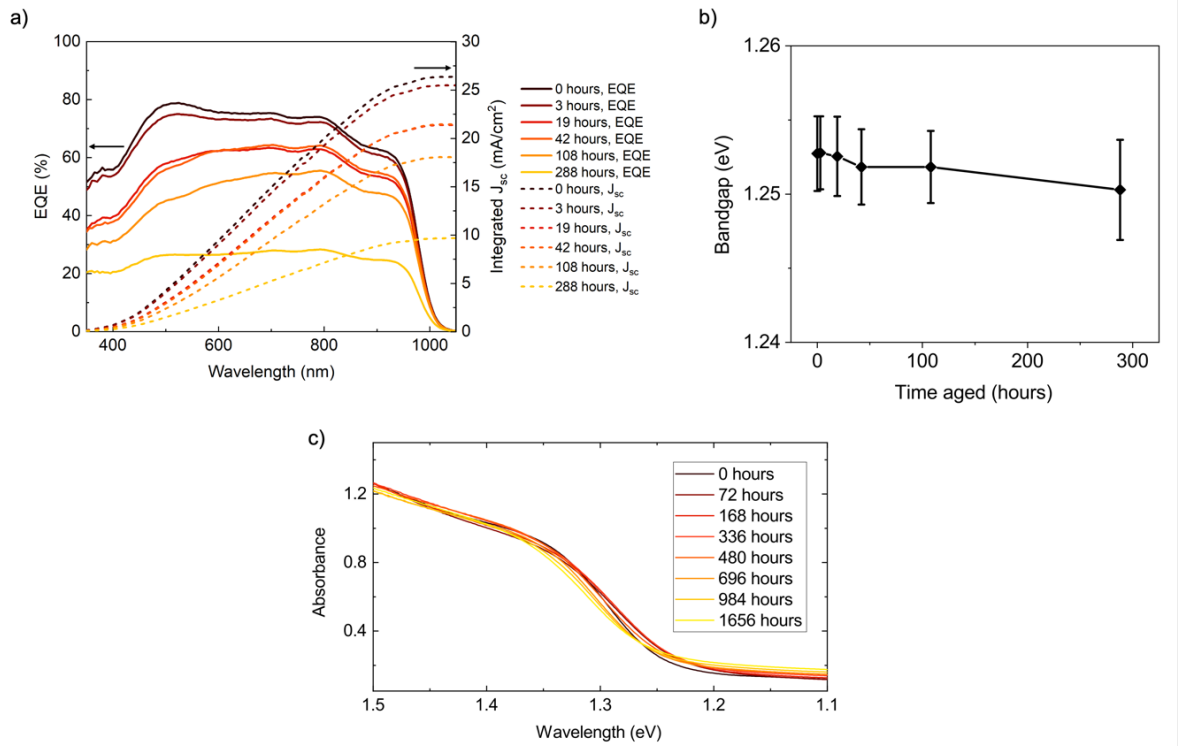


*Figure 4.5. a) External quantum efficiency (EQE) measurements of a typical ITO/PEDOT:PSS/$FA_{0.83}Cs_{0.17}Pb_{0.5}Sn_{0.5}I_3$/PCBM/BCP/Cr/Au device after various periods of encapsulated aging under open circuit, 65 °C, and simulated full spectrum sun light (76 mW cm^{-2}) irradiance conditions. b) Change in the bandgap of devices over time, extracted from measurements in a) by (E*EQE)^2 gradient.[12] c) Absorbance of encapsulated lead-tin perovskite films on glass after various periods of encapsulated aging under 65 °C and simulated full spectrum sun light (76 mW cm^{-2}) irradiance.*

4.3 Opto-electronic changes during aging

Although the perovskite's bulk structure and optical absorption properties remain stable during the first few hundred hours of aging, smaller-scale changes not captured by the previous methods may affect the electronic properties of the film during this time. This especially includes the evolution of point defects which may affect background carrier density, mobility, and rates of defect-mediated recombination.[7] Although it is difficult to

fully characterize the defect landscape and its evolution, changes in the optoelectronic properties of encapsulated lead-tin perovskite films are quantifiably inferred through transient photoconductivity (TPC) and photoluminescence quantum efficiency (PLQE) measurements.

Lead-tin perovskites are slightly p-type with a background hole density p_0 around 10^{14} cm^{-3} (previously determined by others using Hall effect measurements[11] and 2-point probe conductivity measurements[13]). The magnitude of p_0 is important to device functionality, as it is expected to affect the energetic alignment within devices when it is larger than $\sim 10^{15}$ cm^{-3},[14] and to impact recombination kinetics when it is larger than the photoexcited carrier density. Although p_0 has been shown to lie below these critical densities in fresh devices, it remains unclear to what extent it may increase during aging.

To measure background carrier density and long-range mobility, the lateral conductivity across 300-500 μm channels of perovskite thin films is probed in the dark and upon photoexcitation. The TPC method is described in detail elsewhere,[15] but briefly, a perovskite film is excited with a pulse of light to induce a temporary increase in free-carrier density and in turn in conductivity across the sample (conductivity traces are shown in Figure S6, and extracted dark- and maximum photo-conductance are plotted in Figure S7). Since conductivity is the product of carrier density (n, p) and mobility (μ) (eq. 1), measuring both the dark conductivity (eq. 2) and the photoconductivity after a known increase in free charge carrier density (eq. 3) allows us to determine the sum of charge carrier mobilities (eq. 4) and estimate an upper limit for the background hole density, p_0 (eq. 5). As lead-tin perovskites are expected to be p-type, the background electron density n_0 will be many orders of magnitude smaller than the photoexcited carrier densities Δn (10^{16}-10^{19} cm^{-3}) and can be approximated as $n = \Delta n + n_0 \approx \Delta n$.[16]

$$\sigma = e(\mu_n n + \mu_p p) \quad (1)$$

$$\frac{\sigma_{dark}}{e} = \mu_p(p_0) \tag{2}$$

$$\frac{\sigma_{photo}}{e} = \mu_n(\Delta n) + \mu_p(p_0 + \Delta n) \tag{3}$$

$$\frac{\sigma_{photo} - \sigma_{dark}}{e\Delta n} = \boldsymbol{\mu_n + \mu_p} \tag{4}$$

$$\frac{\sigma_{dark}}{e\mu_p} = \boldsymbol{p_0} \tag{5}$$

TPC measurements were performed on perovskite layers deposited on glass and on thin layers of HTLs on glass. The measurements include data from two different batches of glass/perovskite samples, prepared to an identical recipe. When calculating the sum of mobilities from the measured TPC traces, we need to estimate the value of the conductivity immediately after the laser pulse, when the photoexcited charge carrier density is equal to that delivered by the laser pulse. The simplest approach to this is to estimate this to be the maximum conductivity measured, which normally occurs after 20-40 ns. This conductivity is a significant underestimate of the conductivity at t_0, as during this time free charge carriers have already undergone significant recombination and have also been removed from the perovskite by charging of the electrodes. Hence, the sum of mobilities calculated is always a lower boundary estimate of the actual value. Here, I partially correct for this by extrapolating a mono-exponential fit of the photoconductivity back to t_0, as shown in Figure 4.6. However, this only corrects for the charge carriers removed by first-order non-radiative recombination.

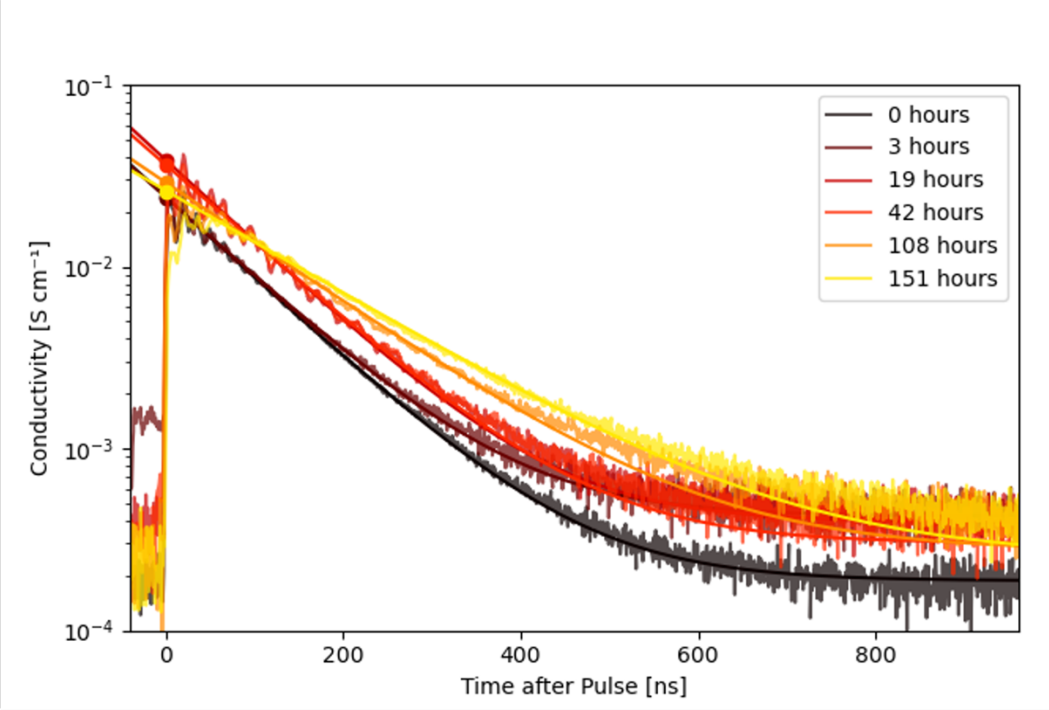


Figure 4.6. Example photoconductivity transients of lead-tin perovskite films on glass, after pulsed excitation at 10 Hz with 3.74 ns pulses, measured after various periods of aging under 65 °C and simulated full spectrum sun light (76 mW cm^{-2}) irradiance. Various fluences were measured at each aging step, and the fluence resulting in the highest conductivity at t_0 was selected and displayed here (on the order of 10^4 nJ cm^{-2}). Solid lines represent fits to a mono-exponential decay, which are extrapolated to t = 0 to extract the maximum photoconductivity (solid dot).

The extent of this underestimation of the t_0 conductivity is expected to increase with excitation fluence, where higher order recombination mechanisms become more dominant. To investigate this further, TPC decays were measured at 9 different fluences for each sample measurement. The extracted mobilities are plotted in Figure 4.7, which shows the expected decrease of mobility at higher fluences, ascribed to an increasingly severe underestimation of the t_0 conductivity. This trend holds for all of the samples measured, and has also been previously observed ion perovskite materials by others.[7] Hence, the maximum sum of mobilities calculated over all excitation fluences is taken to be closest to the 'actual' sum of mobilities in this case.

Interestingly, the dark conductivity also shows significant fluence dependence in some of the samples measured here, increasing with excitation fluence. This could be caused either by the delayed release of charge carriers after excitation (for example by de-trapping from long-lived trap states), and/or by a long-lived increase in mobility as a result of photoexcitation. To minimize the impact of this effect, the dark conductivity measured with the lowest excitation fluence was used to determine p_0.

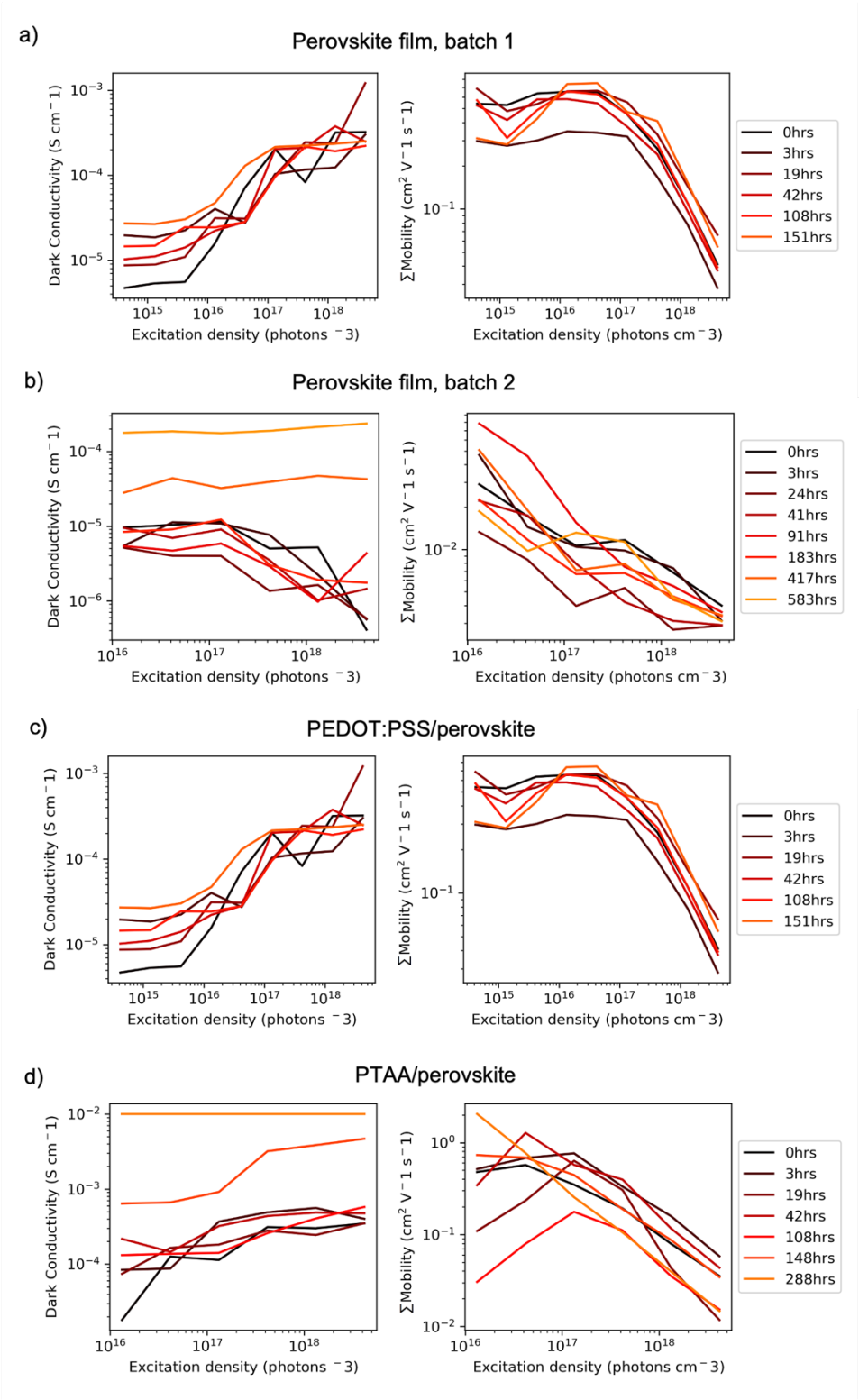


Figure 4.7. Dark conductivity and sum of mobilities extracted from TPC traces at a range of excitation densities, for a) a glass/perovskite sample referred to as 'batch 1' in the text, b) a glass/perovskite sample referred to as 'batch 2' in the text, c) a glass/PEDOT:PSS/perovskite sample, and d) a glass/PTAA/Al_2O_3 NPs/perovskite sample after various periods of aging under 65 °C and simulated full spectrum sun light (76 mW cm^{-2}) irradiance. For some measurements, the sum of mobilities could not be determined as the photoconductance trace was too noisy (a monoexponential fits has $R^2 < 0.8$).

Having discussed and validated the assumptions inherent to the calculations performed, I next present and discuss their results. The estimation of the sum of mobilities of the perovskite films on glass and HTLs versus aging time is presented in Figure 4.8a. The initial sum of mobilities measured here is roughly 10-300x smaller than measured by others using THz conductivity,[7,17] which may be due the systematic underestimation of maximum photoconductivity previously discussed, but may also be due to TPC probing charge transport on a longer length scale which includes transport through grain boundaries.[15] Compared to neat perovskites, the sum of mobilities is not significantly different for films with an $EDAI_2$ passivation layer (commonly used for lead-tin perovskites to improve device performance[1]), or for those deposited on HTLs. In all samples, including both neat perovskite films and in those aged on HTLs, the sum of mobilities varies little during aging.

The estimated p_0 of neat perovskite films as a function of aging time is presented in Figure 4.8b, assuming that electron and hole mobilities are equal (as TPC is only sensitive to their sum). Critically, p_0 only begins to increase significantly and exceed 10^{15} cm^{-3} after 150 hours of aging. The absolute value of p_0 may be slightly higher or lower than estimated here based on the actual electron to hole mobility ratio, but the observation that the perovskite doping density does not significantly change until 150 hours of aging remains valid. This further confirms that the alloying of Sn with Pb successfully avoids high levels of self-doping, not just immediately after fabrication, but also during at least 150 hours of aging.

Clearly, lead-tin perovskites are more resistant to the formation of Sn^{2+} vacancies during aging and hence experience much a slower increase in p-doping than neat tin perovskites. The higher formation energy of these Sn^{2+} vacancy defects in the mixed lead-tin perovskites, calculated by DFT, may play a large role in this.[18] It has also been suggested that the presence of Pb at neighbouring lattice sites may hamper Sn^{2+} oxidation.[19] Additionally, in

neat-Sn perovskites I_2 formed by combination of I_i^- and I_i^+ defects or perovskite reaction with water/oxygen has been found to promote Sn^{2+} oxidation at the perovskite surface.[20–22] Consequently, I_2-removing additives have been found to greatly improve the stability of neat-Sn solar cells under illumination.[22] In contrast to neat-tin and neat-lead perovskites, intrinsic I_2 formation through the combination of I_i^- and I_i^+ defects may be significantly lesser favourable in mixed lead-tin perovskites, as oxidized I_i^+ have been found by DFT calculation to be unstable in this composition.[18] This could also contribute to the slower p-doping observed.

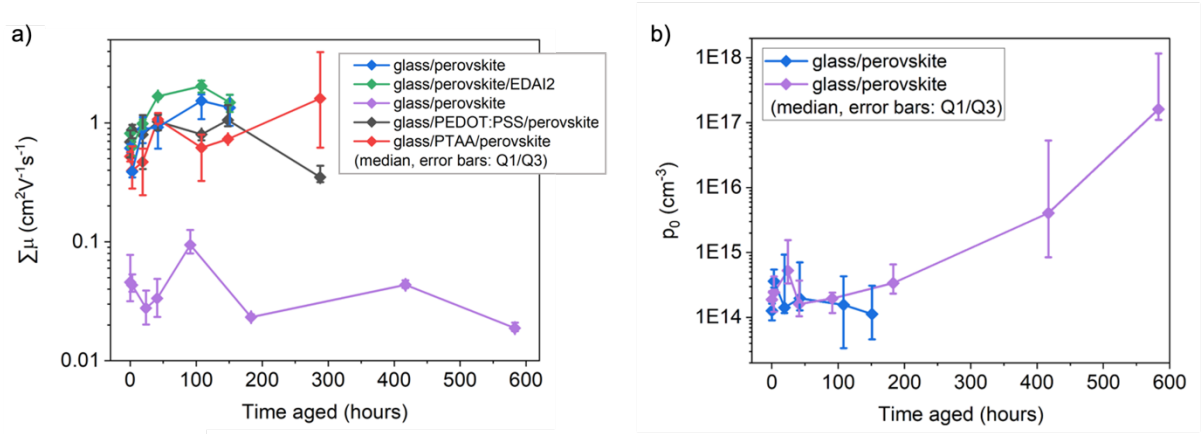


Figure 4.8. a) Sum of mobilities and b) background hole density from TPC measurements of lead-tin perovskite films deposited on glass or thin layers of PEDOT:PSS or PTAA, after various periods of aging under 65 °C and simulated full spectrum sun light (76 mW cm^{-2}) irradiance. For the neat perovskite films, the blue line is referred to as 'batch 1' in the text, and the purple as 'batch 2'. The median is plotted with error bars representing Q1/Q3.

Due to challenges in deconvolving the contribution to the total conductance from the perovskite layer and the HTL individually (HTL conductance higher than perovskite conductance, shown in Figure 4.9a), an absolute value for the p_0 of HTL/perovskite samples cannot be determined. Instead, relative changes in the absolute dark conductance of the HTL/perovskite stacks are considered in the analysis (Figure 4.9b). These should be directly proportional to changes in p_0 during aging, since mobility was not found to vary significantly.

Glass/PEDOT:PSS/perovskite samples show no significant increase in dark conductance during 300 hours (Figure 4.9a), whilst glass/PTAA/perovskite stacks exhibit a rapid increase in dark conductance between 100 and 300 hours of aging, from ~1 x 10^{-8} to ~5 x 10^{-7} S (Figure 4.9a). As the conductance of isolated PTAA films is found to not vary during aging (Figure 4.9a), we may infer that either the perovskite or the PTAA becomes significantly more conductive by being in contact during aging. For the observed 4 x 10^{-7} S conductance to be mainly due to conduction through the PTAA layer (estimated thickness <10 nm),[23] a conductivity of at least 0.4 S cm^{-1} would be required. This is unlikely to be the case, since the conductivity of PTAA is typically not reported to exceed 10^{-4} S cm^{-1} even when extrinsically doped.[24] It is hence proposed that the observed ~50-fold increase in conductance is dominated by changes in the perovskite, namely due to an increased p_0.

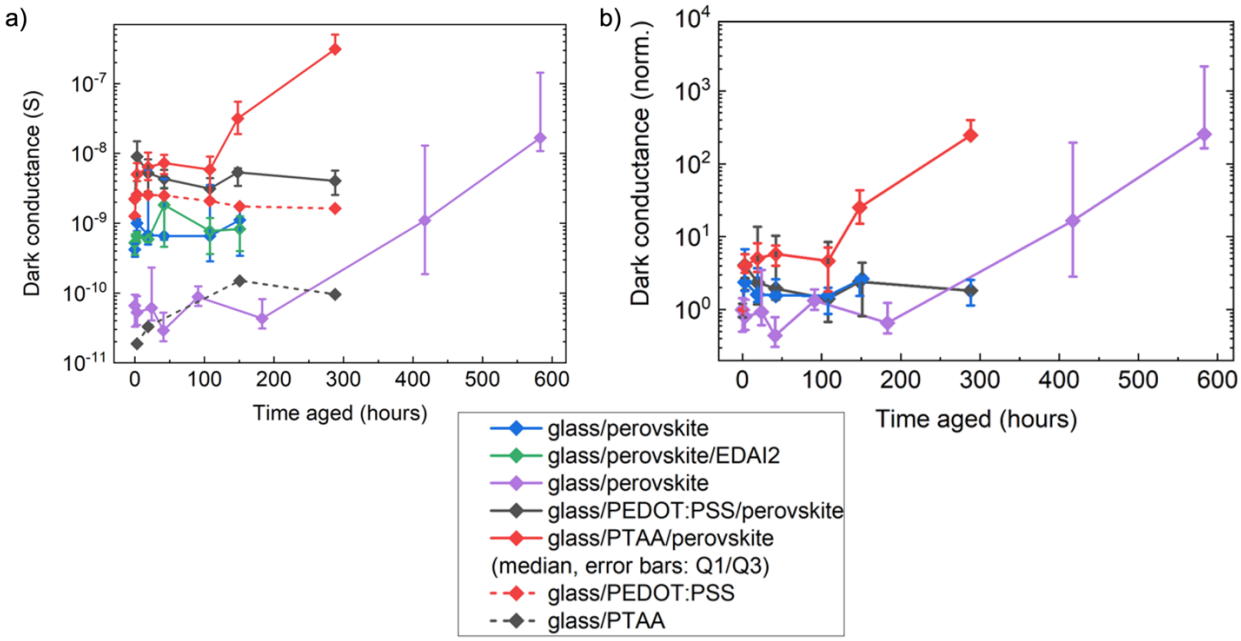


Figure 4.9. a) Dark conductance measured laterally across 300 µm or 500 µm channels on lead-tin perovskite films (660 nm thickness) deposited on glass or thin layers of PEDOT:PSS (diluted 1:6 with IPA) or undoped PTAA (1.5 mg ml^{-1}). Conductance of a film of PEDOT:PSS (diluted 1:6 with IPA) and PTAA (1.5 mg ml^{-1}) deposited on glass measured using the same technique is also shown. b) Values from a) normalized to conductance of fresh samples. For the neat perovskite films,

the blue line is referred to as 'batch 1' in the text, and the purple as 'batch 2'. The median is plotted with error bars representing Q1/Q3.

Next, to assess whether charge carrier recombination dynamics change during aging, the PLQE of lead-tin perovskite films on glass ('batch 1') at excitation fluences ranging from 0.4 - -4 suns equivalent during the first 150 hours of aging was measured. The PLQE continuously decreases during aging, without much change in the shape of the variation in PLQE across excitation fluences (Figure 4.10). This is consistent with a moderate increase in non-radiative recombination during aging. Interestingly, this is not accompanied by a significant decrease in long-range mobility, which would indicate that any defects formed do not act as effective charge scattering centres. When probing changes in the properties of lead-tin perovskites upon exposure to air using THz conductivity measurements, others also observed this increase in nonradiative recombination without a significant accompanying change in mobility.[7,17]

To understand possible effects related to interaction of the perovskite with the HTL during aging, perovskite films deposited on glass/PEDOT:PSS and glass/PTAA were investigated next (Figure 4.10). The PLQE of the fresh lead-tin perovskite on PEDOT:PSS is significantly lower than the PLQE of fresh films on glass or PTAA. Although initial perovskite mobility, crystallinity (from XRD, figure S2) are similar for films deposited on PEDOT:PSS and PTAA, small differences in film quality or heterogeneity[25] stemming from the difference in substrate could still contribute to differences in in defect formation rates. The PEDOT:PSS/perovskite interface is also expected to experience increased non-radiative recombination under open circuit conditions, due to the larger hole density in PEDOT:PSS as a strongly p-doped material.[26] The PLQE of PEDOT:PSS/perovskite films moderately decreases during aging, falling close to or under the noise limit after 19 hours. On PTAA,

however, the PLQE is similar in magnitude and follows a similar trend to that of the perovskite on glass, indicating reduced non-radiative recombination compared to the samples on PEDOT:PSS. Interestingly, we also observe a significant reduction in the gradient of the PLQE against excitation intensity of PTAA/perovskite stacks (Figure 4.10), which could be due to a significant increase in the background carrier density of the perovskite. When the background carrier density becomes larger than the steady-state photoexcited carrier density, the rate of radiative recombination tends towards monomolecular rather than bimolecular,[27] making the PLQE independent of excitation intensity for the measured fluence range.

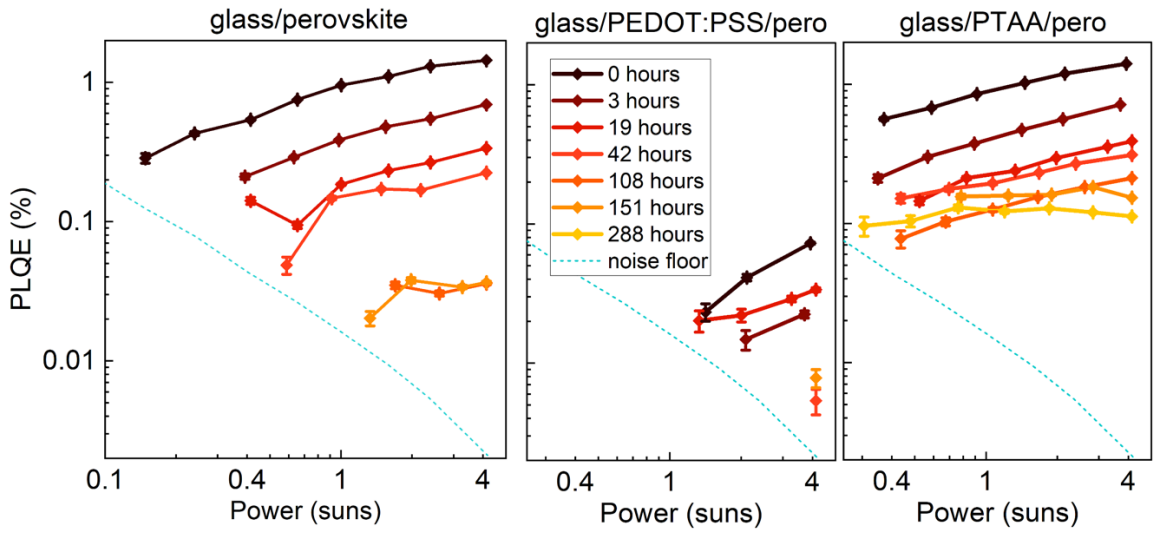


Figure 4.10. Intensity-dependent PLQE of lead-tin perovskite films deposited on glass (batch 1, glass/PEDOT:PSS or glass/PTAA, after various periods of aging under 65 °C and simulated full spectrum sun light (76 mW cm^{-2}) irradiance. Measurements for films on glass were only carried out until 150 hours of aging. The median is plotted with error bars representing Q1/Q3 (n = 4 for batch 1, n = 2 for EDAI$_2$ passivated, n=3 for batch 2, n=4 for sample on HTLs).

To confirm whether the trend observed in the intensity-dependent PLQE of glass/PTAA/perovskite samples can indeed be explained by an increase in background hole density, PLQE simulations were performed. The E_F was varied from 0.05-0.5 eV, and the single deep electron trap density was varied from 0 for Figure 4.11a to 10^{15} cm^{-3} for Figure

4.11b. All other parameters were kept constant. A downshift in Fermi level along with the presence of non-radiative recombination, as in Figure 4.11b, can indeed explain the trend we observe in the intensity-dependent PLQE measurements of glass/PTAA/perovskite samples (Figure 4.10).

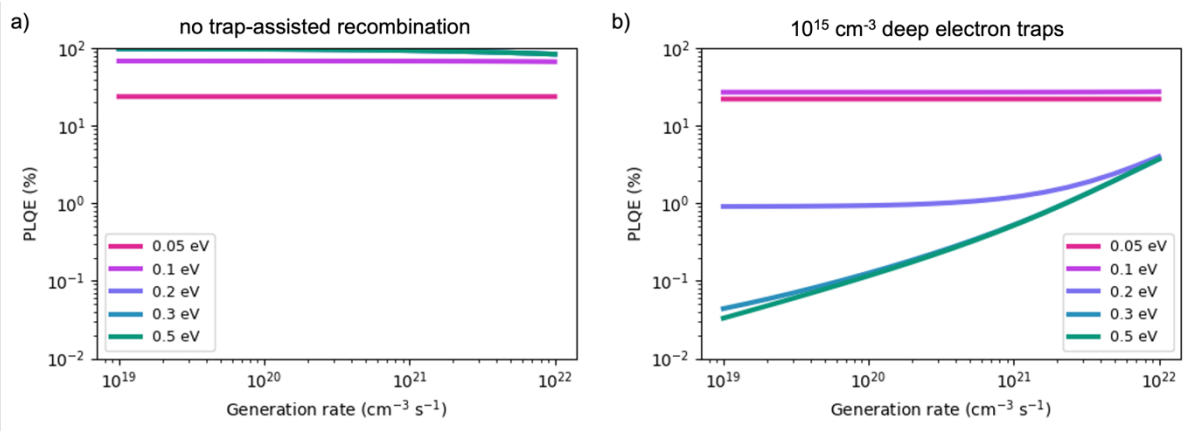


Figure 4.11. PLQE of perovskite films, simulated as a function of excitation fluence at a range of Fermi level positions a) with no trap-assisted recombination and b) with trap-assisted recombination.

The observations from TPC and PLQE measurements together strongly indicate that the presence of PTAA during aging results in increased p-doping in the lead-tin perovskite. This increase in p-doping during aging seems to occur slightly faster than we observe for films aged on glass. Conversely, aging films on PEDOT:PSS seems to suppress an increase in p-doping. This is discussed further this in the context of device aging in section 4.6.

Overall, the p_0 and mobility of isolated lead-tin perovskite films on glass are found to be stable over 150 hours of aging, with p_0 beginning to significantly increase thereafter. The presence of HTLs significantly affects the p-doping process, as films on PTAA already show increased p-doping after 100 hours, whilst films on PEDOT:PSS do not show increased p-doping even after 288 hours of aging. Non-radiative recombination rates are higher in films

on PEDOT:PSS, and moderately increased during aging in all samples. Next, the effect these changes would have on device performance during aging is considered.

4.4 Device performance

Next, lead-tin perovskite devices with an architecture of ITO/PEDOT:PSS or PTAA/$FA_{0.83}Cs_{0.17}Pb_{0.5}Sn_{0.5}I_3$/$EDAI_2$/PCBM/BCP/Cr/Au were investigated during aging at open-circuit conditions. Current density-voltage (J-V) scans under illumination and in the dark for two representative devices are shown in Figure 4.12, and time-resolved traces of maximum power point (MPP), steady-state short-circuit current (J_{sc}) and open-circuit voltage (V_{oc}) tracking are shown in Figure 4.13.

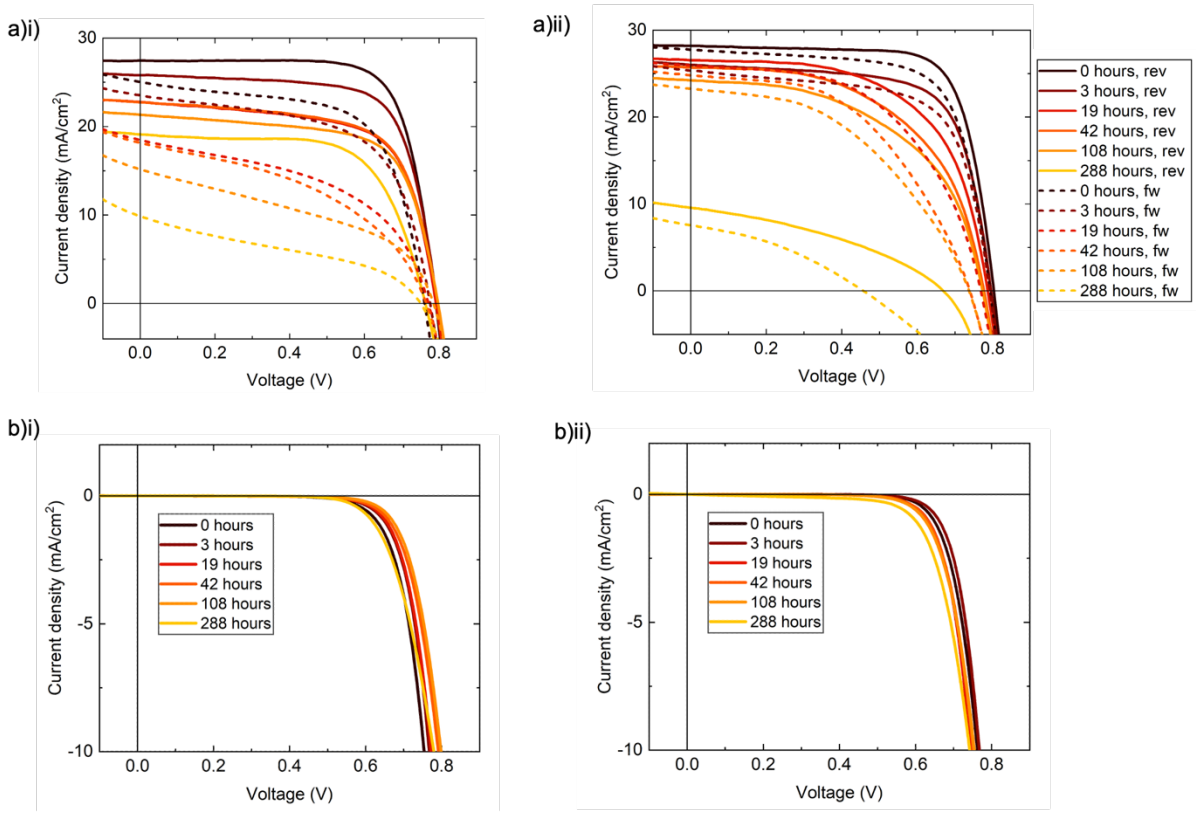


Figure 4.12. a) Current-voltage (J-V) curves measured under AM1.5 100 mW cm^{-2} simulated sun light, and b) J-V curves measured in the dark of champion ITO/HTL/$FA_{0.83}Cs_{0.17}Pb_{0.5}Sn_{0.5}I_3$/PCBM/BCP/Cr/Au devices using i) PEDOT:PSS or ii)

PTAA HTLs. Measurements were performed after various periods of encapsulated aging under 65 °C and simulated full spectrum sun light (76 mW cm^{-2}) irradiance under open circuit conditions.

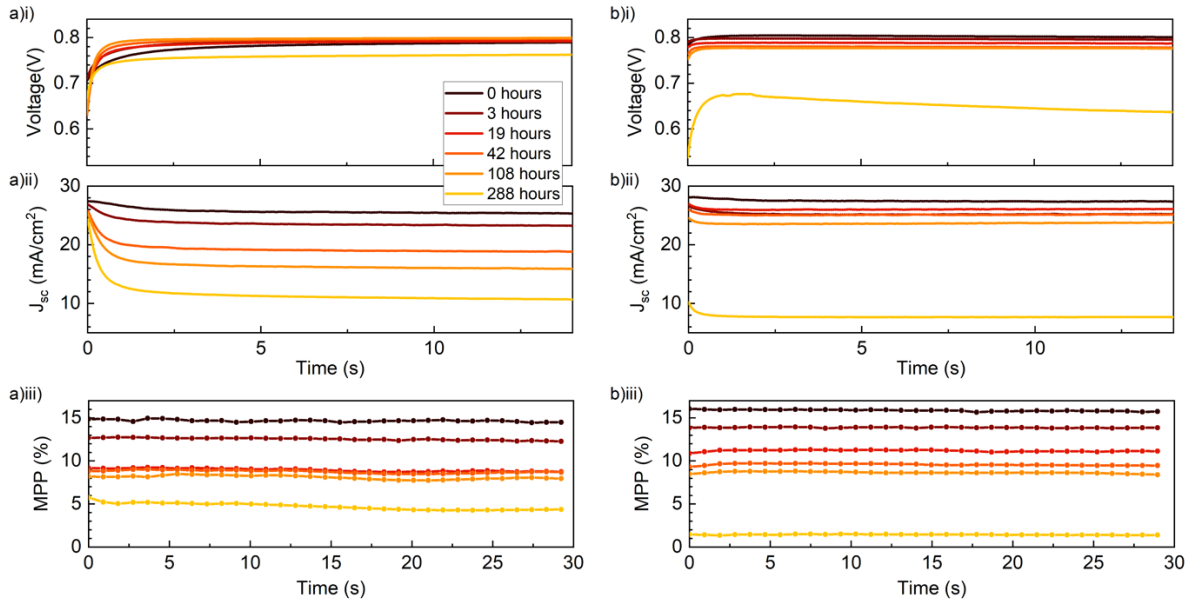


Figure 4.13. a) Voltage at open circuit, b) current density at short circuit, and c) MPP measured under AM1.5 100 mW cm^{-2} simulated sun light of a champion ITO/HTL/ $FA_{0.83}Cs_{0.17}Pb_{0.5}Sn_{0.5}I_3$/PCBM/BCP/ Cr/Au device using i) PEDOT:PSS or ii) PTAA HTLs. Measurements were performed after various periods of encapsulated aging under 65 °C and simulated full spectrum sun light (76 mW cm^{-2}) irradiance under open circuit conditions.

In devices using PEDOT:PSS, the MPP tracked PCE decreases by more than 50% during the first 108 hours of aging (Figure 4.14a). The V_{oc} (Figure 4.14b) is relatively stable during this time, while both the J_{sc} (Figure 4.14c) and fill factor (FF) (Figure 4.14d) rapidly decay. In addition, a notable increase in hysteresis (Figure 4.12 ai) can be observed over time when comparing the reverse (0.9 to -0.2 V) and subsequent forward (-0.2 to 0.9 V) J-V curve sweeps. The dominance of FF and J_{sc} decay during the degradation of lead-tin perovskite devices with PEDOT:PSS HTLs has been previously observed, even with different lead-tin perovskite compositions.[28,29] We also fabricate devices using PTAA and find that their initial performance is comparable to that of devices using PEDOT:PSS (Figure 4.14a), with

significantly less hysteresis (Figure 4.12 aii). Devices using PTAA have a much lower J_{sc} loss during the first 100 hours (Figure 4.14c) but continuously degrade and perform worse than devices using PEDOT:PSS after 288 hours of aging.

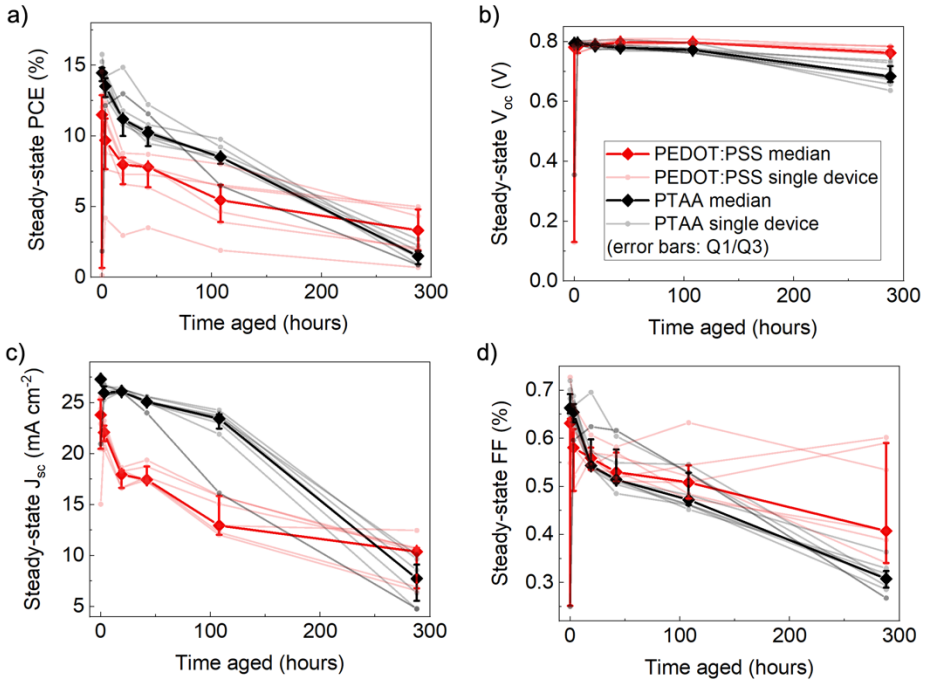


Figure 4.14. a) Performance metrics for encapsulated ITO/HTL/$FA_{0.83}Cs_{0.17}Pb_{0.5}Sn_{0.5}I_3$/PCBM/BCP/Cr/Au solar cells measured at room temperature under AM1.5 100 mW cm^{-2} simulated sun light at various time intervals during aging using PEDOT:PSS or PTAA HTLs, showing i) maximum power point power conversion efficiency, ii) steady-state open circuit voltage, iii) steady-state short circuit current, and iv) steady-state fill factor of devices during aging. Transparent solid lines represent individual devices, whilst the dark solid line represents the median value with error bars denoting Q1/Q3 (n = 8).

For both HTLs used, the current expected by integrating the EQE spectrum with the AM1.5 spectrum corresponds well to the measured current densities in devices (Figure 4.15a). Comparing the EQE of devices under low and high energy illumination provides additional information about bulk material degradation. High energy light (500 nm, solid line in Figure 4.15b) is more strongly absorbed than low energy light (900 nm, dotted line in Figure 4.15b) and hence generates free carriers closer to the HTL. An increase in the

difference between the EQE at these two points during aging could be caused by decreased electron diffusion lengths in the bulk perovskite material. For devices using PEDOT:PSS, EQE at 500 nm illumination indeed degrades somewhat faster in the first 19-42 hours, whilst for PTAA this only begins to happen after 100 hours of aging. This suggests a slightly larger increase in the density of electron traps and/or reduction in electron mobility for devices using PEDOT:PSS. However, for both HTLs the difference in EQE at the two wavelengths is relatively small, and the EQE at 900 nm is also significantly degraded after 300 hours of aging. This indicates that PCE degradation is dominated by a decrease in charge collection efficiency during aging.

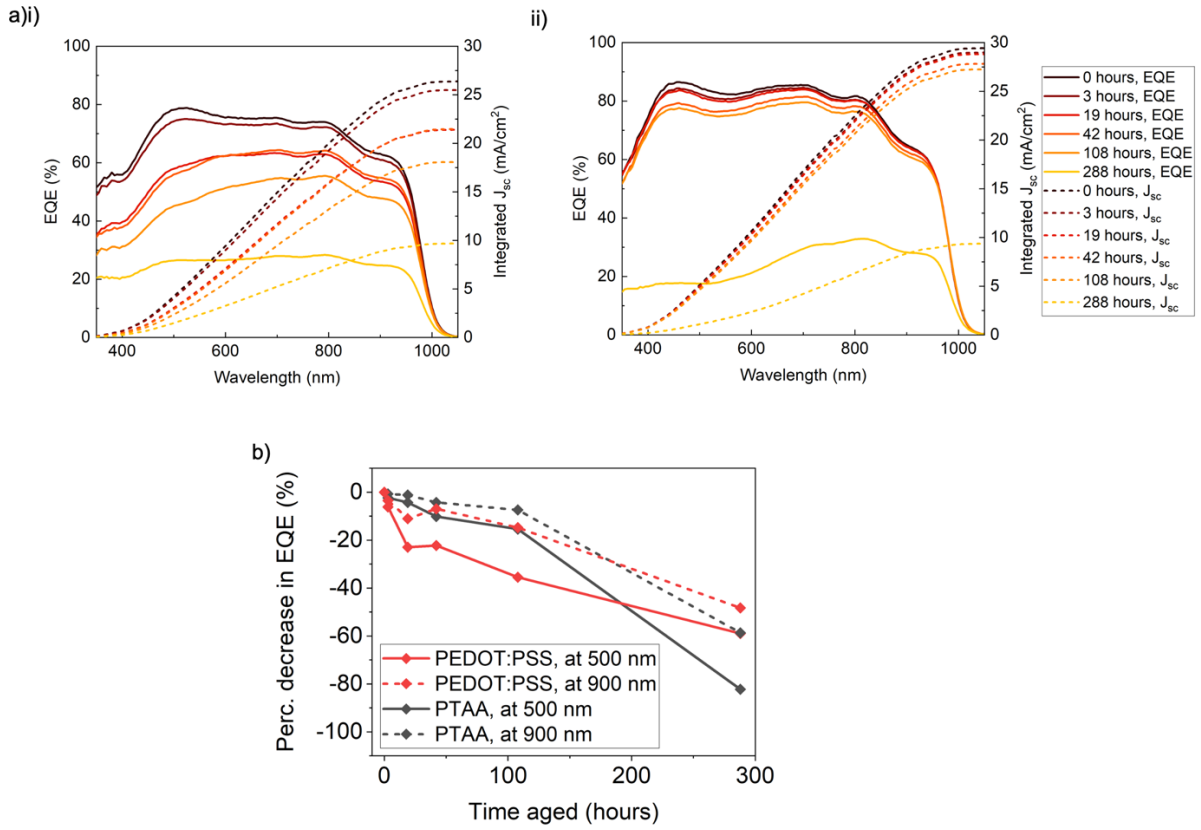


Figure 4.15. a) EQE curves of champion ITO/HTL/$FA_{0.83}Cs_{0.17}Pb_{0.5}Sn_{0.5}I_3$/PCBM/BCP/Cr/Au devices using i) PEDOT:PSS or ii) PTAA HTLs, after various periods of encapsulated aging under 65 °C and simulated full spectrum sun light (76 mW cm^{-2}) irradiance under open circuit conditions. b) EQE from a) at 500 and 900 nm excitation.

Previous investigations by others have also suggested the poor stability of lead-tin PSCs to be due to the formation of a charge extraction barrier, possibly as a result of the formation of degradation products,[28] a reaction with PEDOT:PSS at elevated temperatures,[29] and/or a conductivity drop at the perovskite grain boundaries.[29] I instead postulate that the formation of this charge extraction barrier arises from the effects of the bias-induced accumulation of mobile ions in the perovskite absorber at interfaces in response to an applied bias. This has been suggested to decrease device performance by hindering charge extraction.[13] Such an effect is expected to result in a rapid decay in J_{sc} when measuring at short-circuit. In fresh devices with both HTLs, only a minor steady-state J_{sc} decay is observed (Figure 4.16). However, after 288 hours of aging this decay increases to ~12 mA cm^{-2} in devices using PEDOT:PSS, whilst devices using PTAA show a much smaller current decay of only ~3 mA cm^{-2} after aging. I next attempt to explain this difference by examining the impact of a mobile ion population on these two different device architectures.

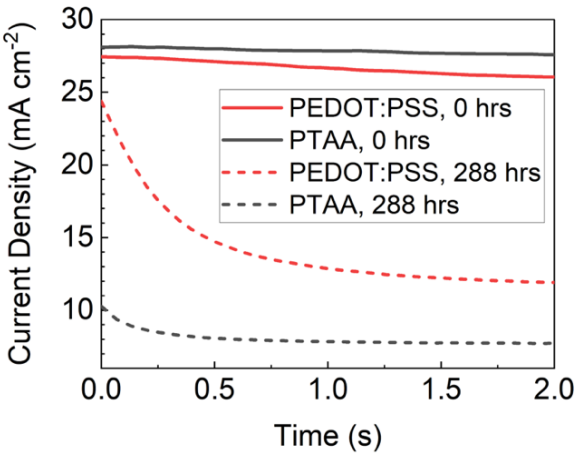


Figure 4.16. Current density under AM1.5 100 mW cm^{-2} simulated sun light over time at short circuit of a champion ITO/HTL/$FA_{0.83}Cs_{0.17}Pb_{0.5}Sn_{0.5}I_3$/ PCBM/BCP/Cr/Au device using a PEDOT:PSS or PTAA/Al_2O_3 HTL, measured after various periods of encapsulated aging under 65 °C and simulated full spectrum sun light (76 mW cm^{-2}) irradiance under open circuit conditions.

4.5 Impact of mobile ions on device performance during aging

It has been understood for several years now that the diffusion of I^- vacancies, and possibly also the slower diffusion of other vacancies or interstitials, is possible in PSCs with a variety of perovskite compositions.[30,31] In lead-tin PSCs, rapid-moving ions have previously been shown to cause significant performance losses in fresh devices.[13] This has been rationalized to be caused by the bias-induced accumulation of mobile ions at interfaces during device operation, resulting in screening of the bulk electric field across the absorber.[32,33] The resulting performance losses have been shown to get worse during aging under illumination, and seem to dominate early-time performance degradation for a variety of neat-Pb perovskite compositions.[34,33]

To investigate how such bias-induced processes affect device performance during aging, J-V scans were performed at a wide range of scan rates on fresh and aged devices.[35] Devices are pre-biased close to V_{oc} before carrying out a reverse and forward J-V sweep. We reliably measured J-V scans with rates between 0.2 ms - 7s per scan, and the extracted J-V parameters are presented in Figure 4.17. When a scan is performed at a faster rate than the characteristic time of ion motion, mobile ions are expected to redistribute during the scan in response to the applied voltage. When a scan is performed at a faster rate than the characteristic time of ion motion, however, it reveals the characteristics of a device with ions 'frozen' in their pre-biasing position.[13] Theoretical and experimental investigations have indicated that the main bias-driven process expected to affect device performance on the ms-s timescale is the migration of iodide vacancies across the perovskite.[30,36–39] Other mobile ion candidates such as A- or B-cation vacancies may still affect device stability by migrating during aging, but are not expected to undergo bias-driven migration on the timescale of our J-V scans. The difference between 'fast' and 'slow' J-V scans are hence expected to represent

the difference between the impact of iodide vacancies at their pre-biasing position compared to their redistributed position.

Bias-driven processes that are reversible on slower timescales than ~7s (such as the migration of ionic species other than iodide vacancies[40]) will not affect either the fast or slow scan. To evaluate whether slower bias-driven processes may also affect device performance, J-V parameters from the slowest scan at 0.18 V s^{-1} (7 s $scan^{-1}$) (Figure 4.17b) can be compared to 30s MPPT measurements (Figure 4.13). They are mostly very similar, indicating little additional impact of bias-driven processes on the timescale of 10s of seconds. The impact of very slow bias-driven processes on device performance during aging is likely minor compared to other degradation modes,[41] so is not investigated further here.

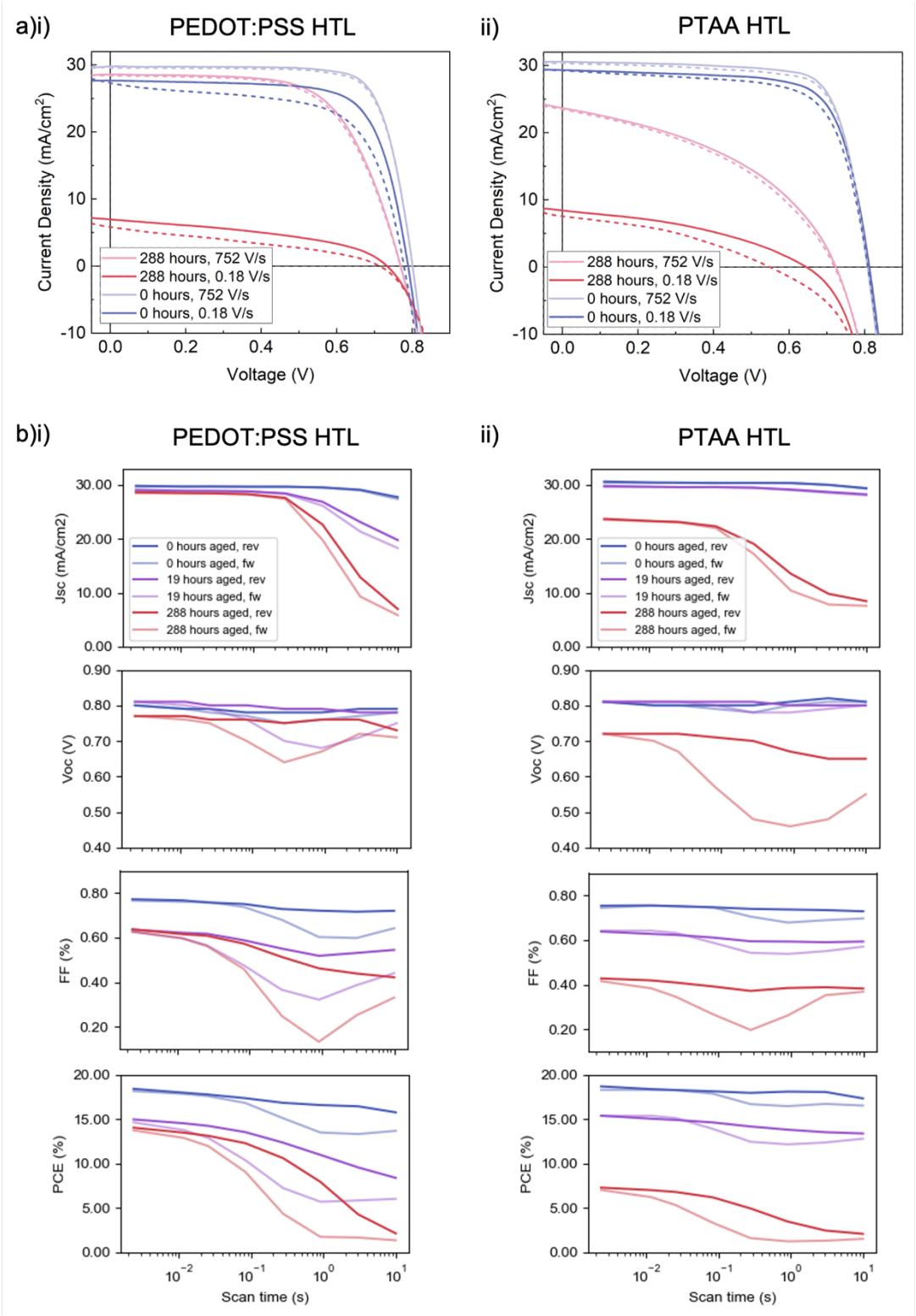


Figure 4.17. a) Fast 752 V s^{-1} and slow 0.18 V s^{-1} J-V scans of a ITO/HTL/ $FA_{0.83}Cs_{0.17}Pb_{0.5}Sn_{0.5}I_3$/$EDAI_2$/PCBM/BCP/Cr/Au device under AM1.5 100 mW cm^{-2} simulated sun light after 0 and 288 hours of aging, using either a i) PEDOT:PSS or a ii) PTAA HTL. Solid lines indicate reverse scans (from positive to negative voltage), and dotted lines indicate subsequent forward scans (from negative to positive voltage). b) Measured J-V parameters of lead-tin perovskite devices using i) PEDOT:PSS or ii) PTAA HTLs at varying scan rates, after 0, 19 and 288 hours of encapsulated aging under 65 °C and

simulated full spectrum sun light (76 mW cm^{-2}) irradiance under open circuit conditions. Solid lines indicate reverse scans (from positive to negative voltage), and transparent lines indicate subsequent forward scans (from negative to positive voltage)

The difference between the PCE at 'slow' (0.18 V s^{-1}) and 'fast' scans (752 V s^{-1}) represents the PCE loss that can be ascribed to the bias-induced accumulation of rapid-moving ions, and is plotted over time in Figure 4.18. Comparison of slow and fast J-V scans shows that bias-induced ion accumulation severely impacts the performance of devices using a PEDOT:PSS HTL. Surprisingly, the large J_{sc} loss observed in devices using PEDOT:PSS after aging for 288 hours is almost entirely recovered at fast scan speeds (Figure 4.18a). Although there remains a small progressive loss in FF under fast scans, the performance degradation is minor compared to that observed in the slow scans. This is strong evidence that the rapid degradation observed in lead-tin perovskite devices using PEDOT:PSS is dominated by effects from bias-induced accumulation of mobile ions at interfaces.

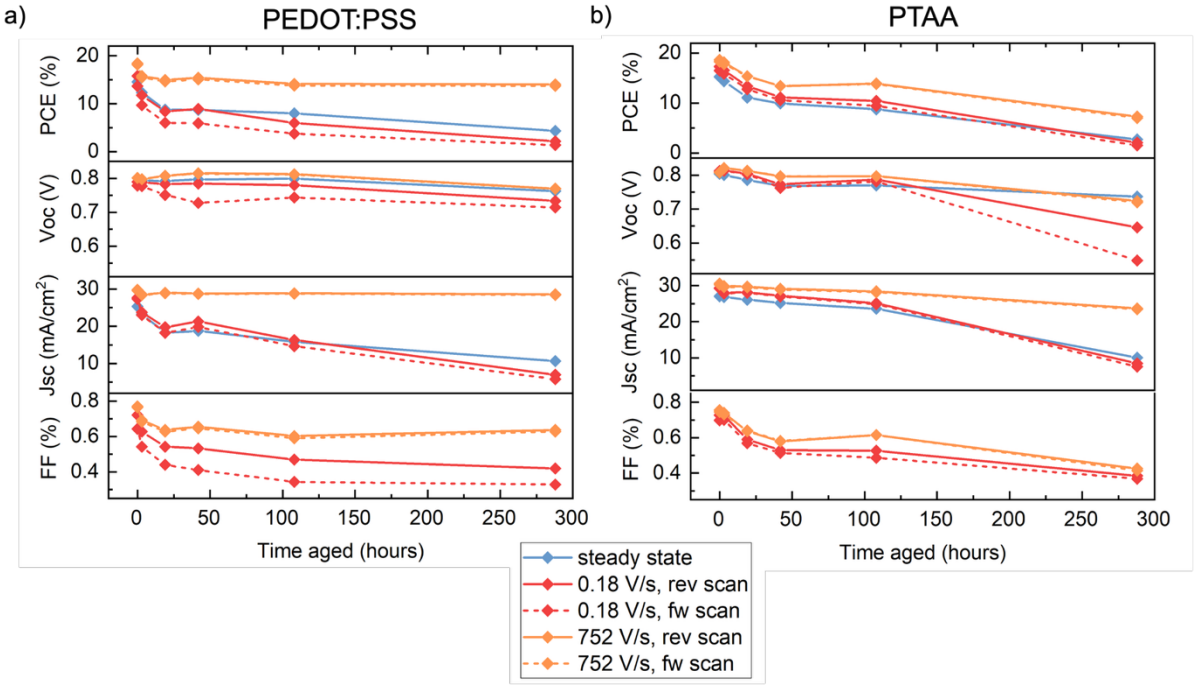


Figure 4.18. J-V parameters extracted from fast 752 V s^{-1} (orange) and slow 0.18 V s^{-1} (red) J-V scans of a champion ITO/HTL/$FA_{0.83}Cs_{0.17}Pb_{0.5}Sn_{0.5}I_3$/PCBM/BCP/Cr/Au device using a) PEDOT:PSS or b) PTAA HTLs. Parameters from steady-state measurements of the same devices from Figure 4.14 are overlaid in blue. Measurements were performed after various periods of encapsulated aging under 65 °C and simulated full spectrum sun light (76 mW cm^{-2}) irradiance under open circuit conditions.

Recent work by others suggested the possibility of a reduced impact of ion migration in lead-tin perovskites compared to neat lead perovskites, inferred from the observation of lower hysteresis in field effect transistors (FETs)[42] and the computational prediction of a higher energy barrier to I^- migration with an increased density of Sn^{2+} vacancies.[43] It is demonstrated here that this is not the case in lead-tin PSCs with PEDOT:PSS HTLs. This may be because the relatively lower density of Sn^{2+} vacancies in our lead-tin perovskite removes the higher energetic barrier to I^- migration, and/or because of a higher density of rapid-moving ions.

In devices with PTAA HTLs, there remains a difference between the slow and fast scans after aging for 288 hours, indicating that bias-induced mobile ion accumulation also contributes to device performance degradation when a PTAA HTL is used (Figure 4.17). However, the performance loss due to rapid-moving mobile ions is initially smaller than in devices using PEDOT:PSS, increases minimally during the first 20 hours and remains approximately half as large as that of devices using PEDOT:PSS (Figure 4.19). In contrast, the losses observed in the fast J-V scan after aging (which must be due to factors other than the bias-induced accumulation of mobile ions) are much worse than for devices using PEDOT:PSS.

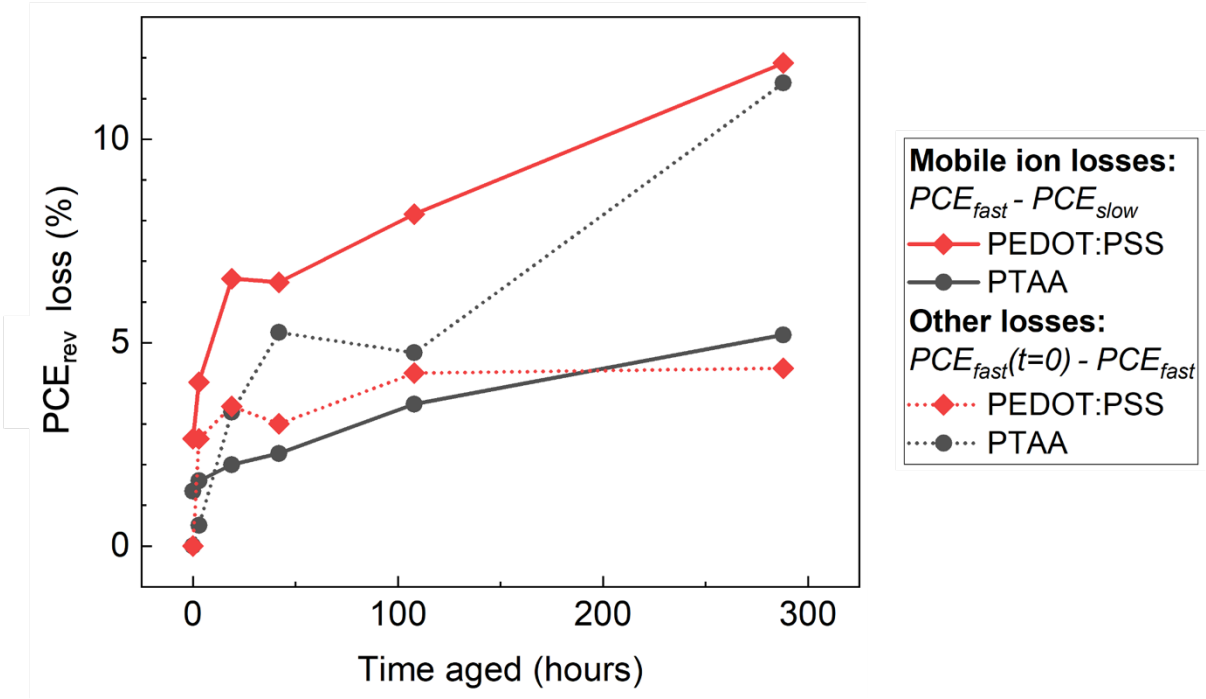


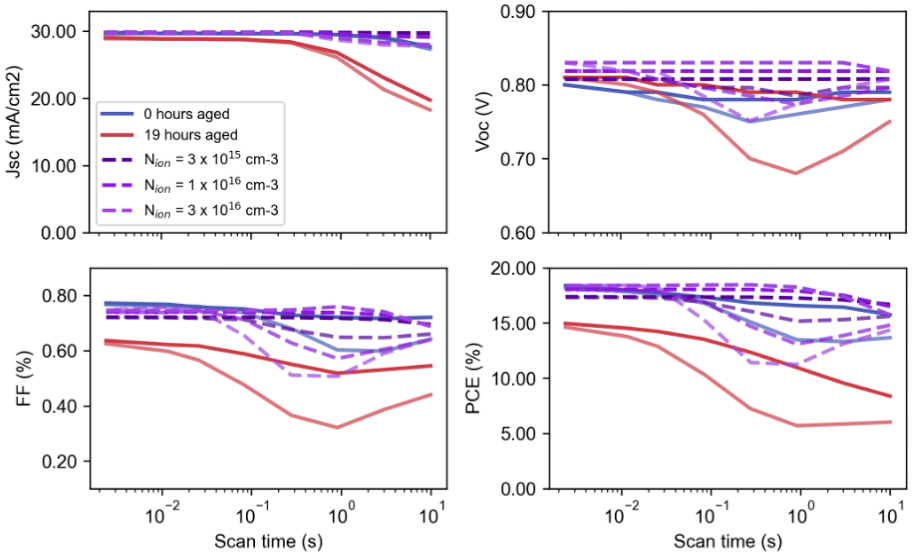
Figure 4.19. Plot of the PCE loss extracted from the forward J-V scans of the champion devices shown in Figure 4.18, after various periods of aging. Losses are divided into 'mobile ion' losses, derived from the difference between fast (752 V s^{-1}) and slow (0.18 V s^{-1}) scans at each aging time, and 'other' losses, derived from the progressive losses observed in the fast (752 V s^{-1}) scans over time.

To more deeply investigate the cause of the increased impact of mobile ion-induced field screening during aging, we next consider the full range of J-V scan speeds from 1 s scan^{-1} to 4 ms scan^{-1} (Figure 4.17). Previous work has argued that in neat-Pb perovskites, an increase in mobile ion-related losses could be best ascribed to an increase in the density of these highly mobile ionic species.[33] To investigate whether this is also the case in these lead-tin devices, the IonMonger drift-diffusion software[44] was used to simulate JV curves at the same range of scan speeds and compare them to the experimental data. The parameters used are given in Appendix 1.1, and the full range of simulations is shown in Figure 4.20 and Figure 4.21. As Ionmonger cannot take an elevated background hole density into account, simulations are compared to J-V measurements after 19 hours of aging, when PCE is already

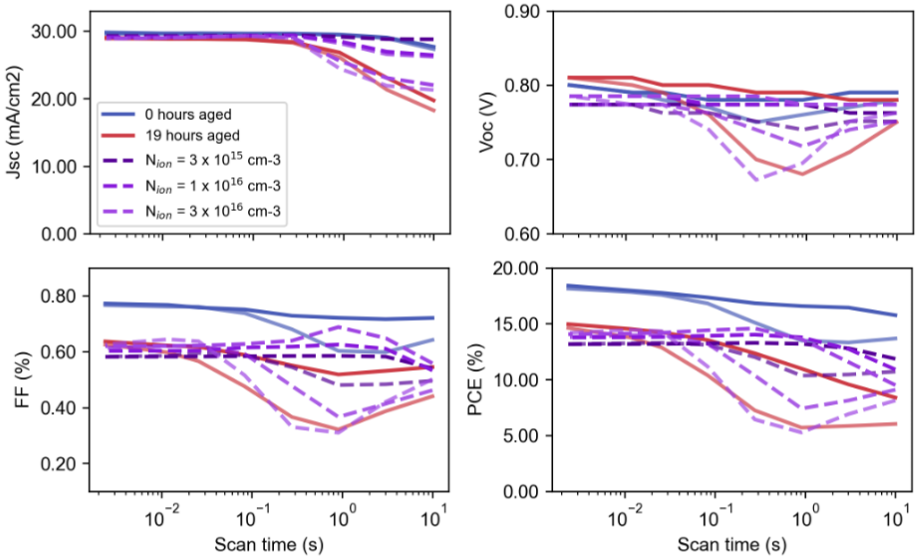
significantly degraded but elevated background carrier densities are not yet expected in devices with either HTL.

The effects of changes in mobile ion density, bulk free carrier lifetime, and surface recombination velocity (SRV) on J-V parameters are simulated at the full range of experimental scan speeds (Figure 4.20 and Figure 4.21). For devices using both HTLs the magnitude of mobile-ion-related losses and hysteresis increases with mobile ion density, but also with a decrease in bulk lifetime. Increasing SRV only slightly increased mobile-ion-related losses for the low-doping CTLs PCBM and PTAA, but had a stronger effect on mobile-ion-related V_{oc} losses for the highly doped PEDOT:PSS.

a) **PEDOT:PSS HTL,** varying ion density (**tau = 400 ns**, SRV = 5 / 50 cm s-1)



b) **PEDOT:PSS HTL,** varying ion density (**tau = 80 ns**, SRV = 5 / 50 cm s-1)



c) **PEDOT:PSS HTL,** varying SRV (tau = 400 ns, ion density = 10^{16} cm-3)

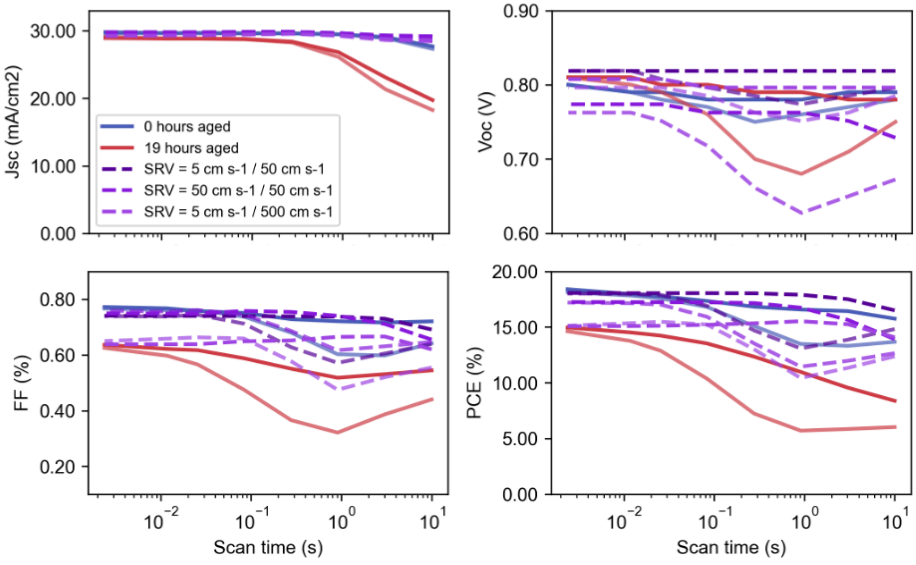
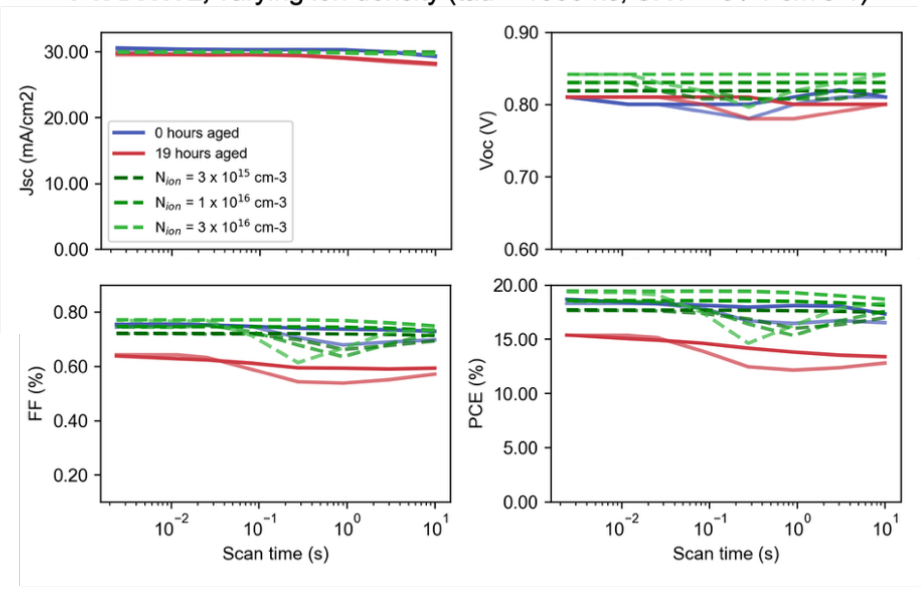
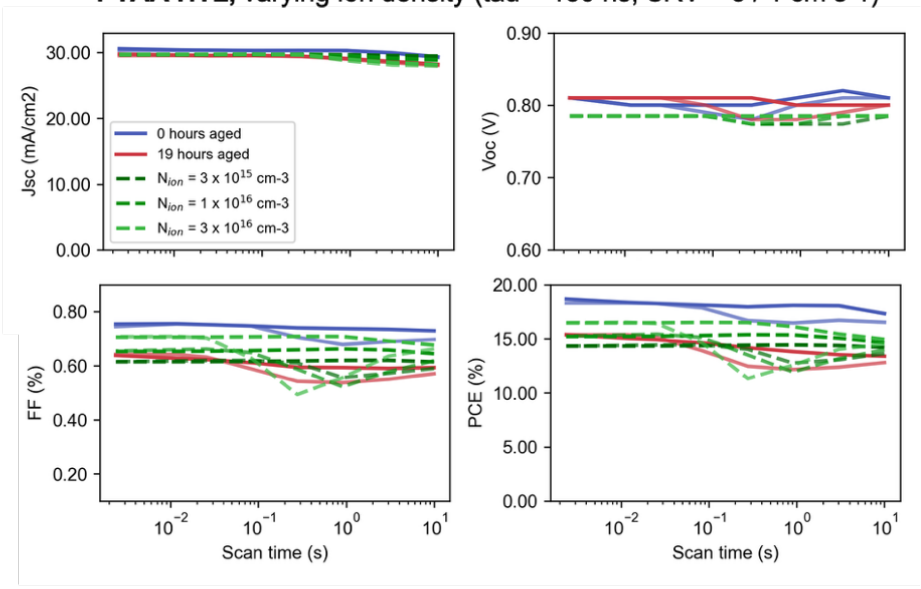


Figure 4.20. Simulations of J-V parameters at varying scan rates of lead-tin perovskite devices with a PEDOT:PSS HTL, using the IonMonger software.[44] Simulations are overlaid on measured J-V parameters at varying scan rates after 0 and 19 hours of encapsulated aging under 65 °C and simulated full spectrum sun light (76 mW cm^{-2}) irradiance under open circuit conditions. Solid lines indicate reverse scans (from positive to negative voltage), and transparent lines indicate subsequent forward scans (from negative to positive voltage).

a) **PTAA HTL,** varying ion density (tau = 1000 ns, SRV = 5 / 1 cm s-1)



b) **PTAA HTL,** varying ion density (tau = 150 ns, SRV = 5 / 1 cm s-1)



c) **PTAA HTL,** varying SRV (tau = 1000 ns, ion density = 10^{16} cm-3)

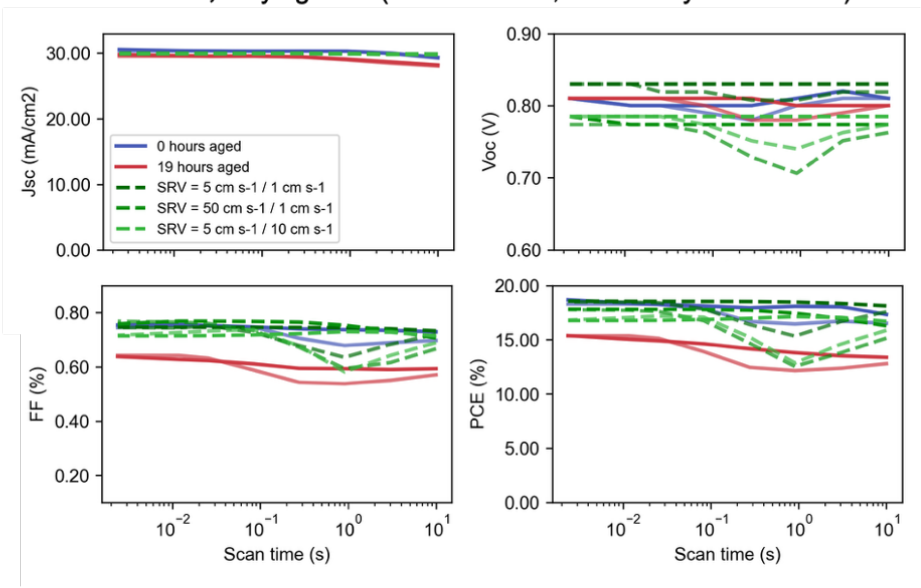


Figure 4.21. Simulations of J-V parameters at varying scan rates of lead-tin perovskite devices with a PTAA HTL, using the IonMonger software.[44] Simulations are overlaid on measured J-V parameters at varying scan rates after 0 and 19 hours of encapsulated aging under 65 °C and simulated full spectrum sun light (76 mW cm^{-2}) irradiance under open circuit conditions. Solid lines indicate reverse scans (from positive to negative voltage), and transparent lines indicate subsequent forward scans (from negative to positive voltage).

The best match to experimental data after 0 and 19 hours of aging that could be found by varying these parameters is presented in Figure 4.22. We found that for devices using PEDOT:PSS, the observed variation in J-V data across scan speeds could be well explained by a combined increase in mobile ion density and bulk recombination rate, whilst for devices using PTAA, increasing bulk recombination rate alone was sufficient to replicate experimental data (Figure 4.22). The best match to experimental data was achieved with a somewhat lower initial bulk lifetime for devices using PEDOT:PSS, but with both lifetimes decreasing to a similar extent during the first 19 hours of aging (5-fold for PEDOT:PSS and 7-fold for PTAA, respectively).

Crucially, simulations reveal that for devices with PEDOT:PSS, the experimental data could not be replicated without an increase in mobile ion density. Whilst increasing bulk and/or surface recombination rates does also increase mobile-ion-related losses, simulations with these parameters resulted in significantly different V_{oc} and/or FF than the observed data (Figure 4.21 a, b iii). Interestingly, a relatively small (3-fold) increase in mobile ion density was sufficient to replicate the significant losses observed in devices using PEDOT:PSS after 19 hours.

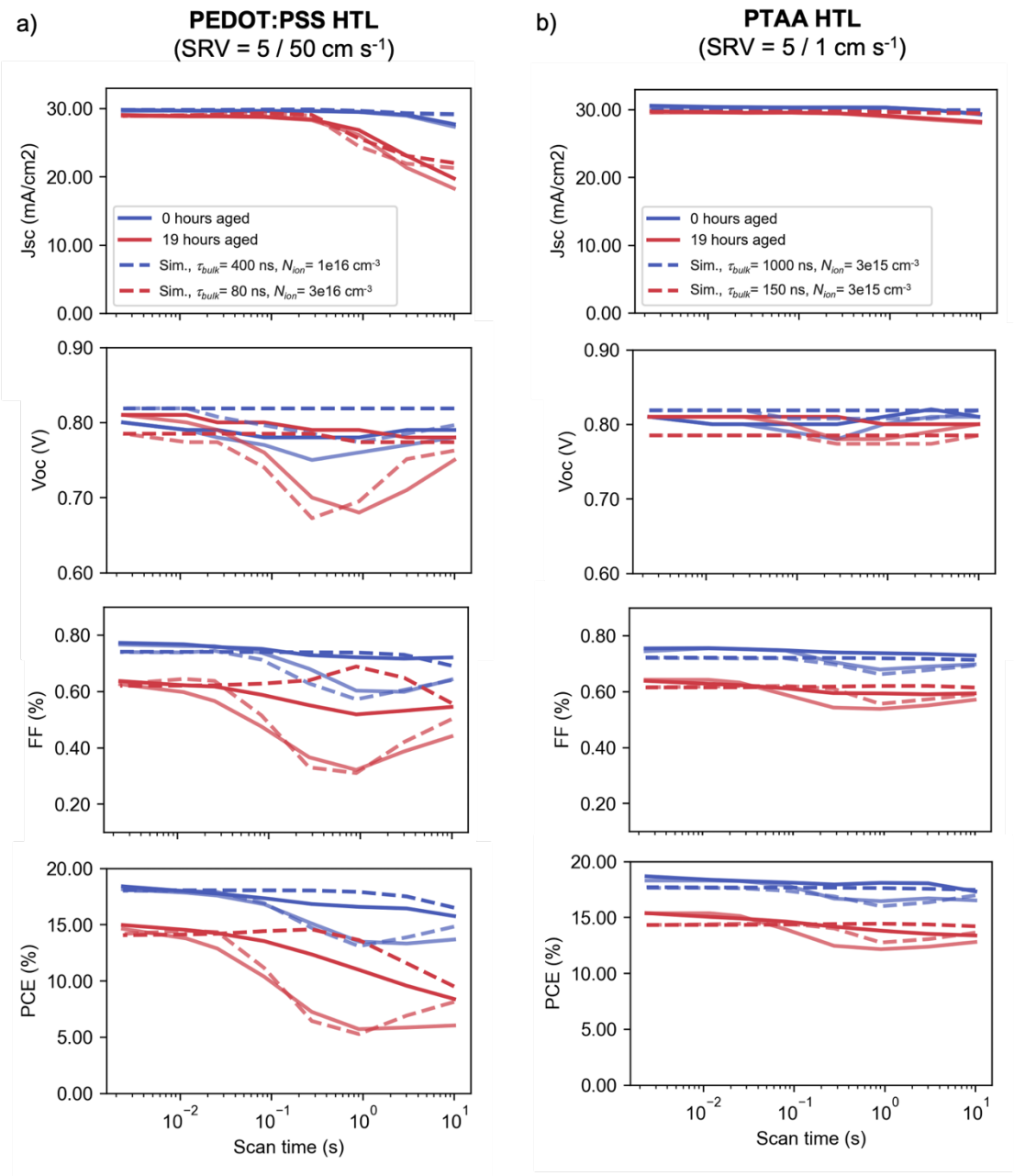


Figure 4.22. Simulations of J-V parameters at varying scan rates of lead-tin perovskite devices using a) a PEDOT:PSS HTL and b) a PTAA HTL using the IonMonger software.[44] Simulations are overlaid on measured J-V parameters at varying scan rates after 0 and 19 hours of encapsulated aging under 65 °C and simulated full spectrum sun light (76 mW cm^{-2}) irradiance under open circuit conditions. Solid lines indicate reverse scans (from positive to negative voltage), and transparent lines indicate subsequent forward scans (from negative to positive voltage).

Some iodide vacancy formation is expected in all perovskite materials during aging,[39] but this process can be accelerated by chemical interaction between perovskite and HTL. PSS

contains sulfonic acid groups (-SO_3H) which can react with I^- from the perovskite to form HI, leaving iodide vacancies in the perovskite film.[45] As both the iodide vacancies in the perovskite and protons in PEDOT:PSS are mobile (under illumination and/or heat),[42,46] this reaction is not limited to the interface but likely spreads through both layers until both reactants are significantly depleted. HI vapor is expected to be highly mobile in the perovskite[47] and may easily travel to CTLs or surfaces to react further, such that iodide vacancies are permanently left in the film. HI may participate in a number of different reactions within the perovskite solar cell, and oxidized iodine degradation products have been previously observed in lead-tin perovskites even in air-free environments.[28] It is also possible that direct complexation between PEDOT and I^- contributes to the production of iodide vacancies in the perovskite.[48] In contrast, PTAA is expected to be more chemically inert and is not expected to accelerate the formation of iodide vacancies in these ways. Hence, the increased rapid-moving ion related performance losses that we observe during aging when using PEDOT:PSS HTLs can be explained by the formation of a higher density of iodide vacancies due to chemical interaction between PSS and the perovskite. According to our simulations, densities of 10^{16}-10^{17} cm^{-3} iodide vacancies are already sufficient to replicate the performance degradation observed. As this only corresponds to 0.001-0.01% of iodide sites, the structural integrity of the perovskite phase remains intact. Such a small difference in iodine density in the perovskite lattice is also difficult to detect via chemical characterization methods.

An often-cited alternative effect of acidic PEDOT:PSS in perovskite solar cells is etching of the ITO electrode layer,[49] resulting in In^{3+} migration through the perovskite which could be occurring here. However, here the effects of ion migration affect devices using both PEDOT:PSS and PTAA HTLs at similar scan rates (Figure 4.17), suggesting that a mobile ion with a similar diffusion coefficient affects both architectures. Whilst In^{3+} migration can

likely affect interfacial properties when aging devices using PEDOT:PSS,[50] it is hence unlikely that In^{3+} ions are directly responsible for the rapidly reversible bias-induced losses we observe.

The increase in the density of iodide vacancies in devices using PEDOT:PSS during aging suggested by our results can in theory be mitigated not only by using PTAA, but also by using deprotonated PSS[51] or many other suitable chemically inert HTLs. Indeed, treatment of PEDOT:PSS with NaOH has already been observed to significantly increase the stability of devices during aging under illumination.[52,26]

The portion of the performance degradation due to bias-induced mobile ion accumulation in lead-tin perovskite devices using PTAA reaches 5% after 288 hours of aging, which is comparable to high-efficiency neat-lead devices examined in one study.[33] Also, the iodide vacancy densities used in these J-V simulations, as well as the non-radiative recombination rates and mobilities measured in section 4.3, are all comparable to those found in neat-lead perovskites.[53] This indicates that the mixed lead-tin perovskite composition used here is at least as resistant to iodide vacancy formation in the isolated perovskite as most neat-Pb compositions. In these compositional families, I hence argue that device architecture is likely to play a bigger role in determining mobile ion field screening-related losses, as CTLs and electrode materials may promote iodide vacancy formation by reacting with iodine-containing species stemming from the perovskite. Whilst the effects of mobile ions have been much less investigated in neat-tin perovskites, it is possible that the high background hole density (10^{18}-10^{20} cm^{-3})[54] affects the internal distribution of the electric field so strongly[14] that effects from redistribution of the smaller density of mobile ions are minor.

Whilst the degradation of devices using PTAA is slightly delayed compared to those using PEDOT:PSS, they have overall worse steady-state PCE after 288 hours of aging.

Hence, I next focus on identifying the causes of the remaining performance degradation observed in the fast scans.

4.6 Impact of electronic changes on device performance during aging

For devices using PTAA, the fast-scan losses far exceed the magnitude of slow-scan losses during aging, indicating that performance degradation is dominated by factors other than an increased impact of mobile ions accumulating at interfaces. We previously inferred a ~50-fold increase in the p_0 of the perovskite absorber after 288 hours of aging in contact with PTAA, which could significantly affect device performance. To visualize how this and other changes in material properties could affect device performance during the fast J-V scans (with mobile ions immobile at their open circuit positions), drift-diffusion simulations were performed using the SCAPS-1D simulation package (parameters used are detailed in Appendix 1.2).[55] Unlike the Ionmonger package, SCAPS can account for a doped active layer. The background hole density p_0 and deep trap density in the perovskite absorber layer, which were previously found to change during aging, are presented in Figure 4.23 as a function of parameter values. For completeness, changes in the mobility and shallow trap density in the perovskite, trap density at the HTL/perovskite and perovskite/ETL interfaces, and changes in HTL doping density and mobility were also simulated and are presented in Figure 4.24. The fast J-V scans of champion devices after 0 and 288 hours of aging, which reflect device performance with rapid-moving ions frozen at pre-biasing positions, are overlaid on the simulation results in blue and red.

For devices using PEDOT:PSS, both these and the previous simulations suggest that the small FF loss observed in the fast J-V scans can be accounted for by a moderate change in deep trap density, consistent with our earlier simulations and PL measurements, and/or a slight increase in p_0 during aging (Figure 4.23). In devices using PTAA, the previous

Ionmonger simulations suggested that the losses observed during the first 19 hours can be well-accounted for by an increase in deep trap density. However, SCAPS simulations show that after 288 hours of aging, a further increase in bulk recombination rates no longer describes the shape of the fast J-V curve well. Instead, the shape can be most closely reproduced by increasing the p_0 of the lead-tin perovskite to $\sim 10^{16}$ cm^{-3}, although some increase in bulk deep trap density may also contribute (Figure 4.23).

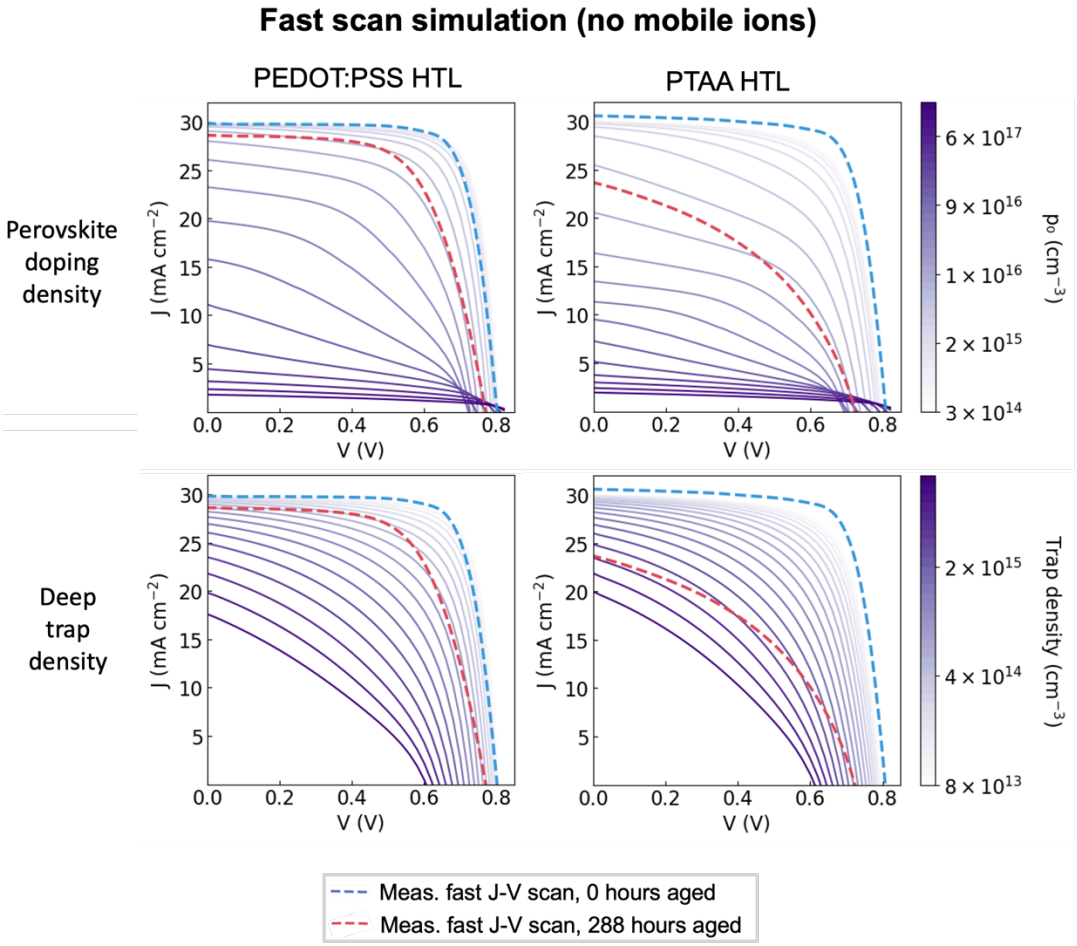


Figure 4.23. Simulated J-V curves of ITO/HTL/ $FA_{0.83}Cs_{0.17}Pb_{0.5}Sn_{0.5}I_3$/PCBM/BCP/Cr/Au devices produced with SCAPS-1D[9] using the HTL parameters of PEDOT:PSS or PTAA. J-V curves presented are created by varying either the background hole density in the perovskite bulk or the deep trap density in the perovskite bulk. Real device data is overlaid, showing fast (752 V s^{-1}) reverse J-V scans of a fresh device (blue dotted line) and 288 hour aged device (red dotted line).

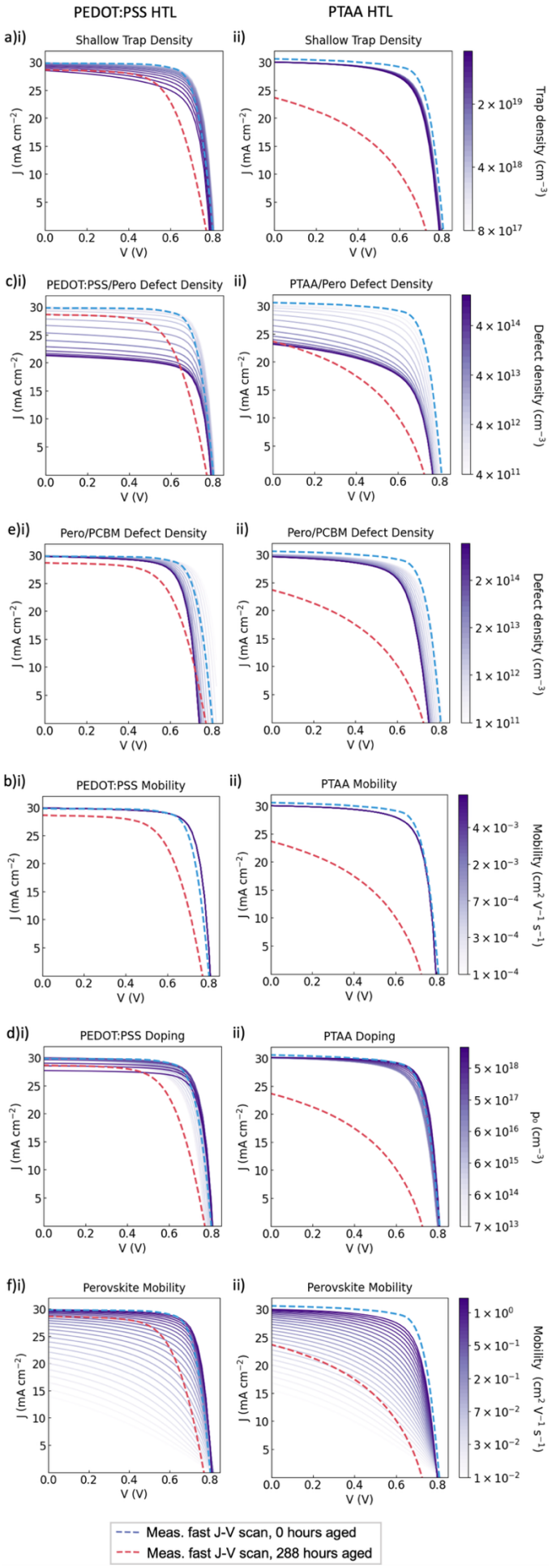

PEDOT:PSS HTL
PTAA HTL
a)i)
Shallow Trap Density
ii)
Shallow Trap Density
Trap density (cm^{-3})
c)i)
PEDOT:PSS/Pero Defect Density
ii)
PTAA/Pero Defect Density
Defect density (cm^{-3})
e)i)
Pero/PCBM Defect Density
ii)
Pero/PCBM Defect Density
Defect density (cm^{-3})
b)i)
PEDOT:PSS Mobility
ii)
PTAA Mobility
Mobility (cm^2 V^{-1} s^{-1})
d)i)
PEDOT:PSS Doping
ii)
PTAA Doping
p$_0$ (cm^{-3})
f)i)
Perovskite Mobility
ii)
Perovskite Mobility
Mobility (cm^2 V^{-1} s^{-1})
J (mA cm^{-2})
V (V)
Meas. fast J-V scan, 0 hours aged
Meas. fast J-V scan, 288 hours aged

Figure 4.24. Simulated J-V curves of ITO/HTL/ $FA_{0.83}Cs_{0.17}Pb_{0.5}Sn_{0.5}I_3$/PCBM/BCP/Cr/Au devices produced with SCAPS-1D[9] using the HTL parameters of i) PEDOT:PSS or ii) PTAA. J-V curves presented are created by varying a) shallow (0.03 eV from conduction band) electron trap density in the perovskite bulk, b) defect density at the perovskite/PEDOT:PSS or PTAA interface, c) defect density at the perovskite/PCBM interface, d) mobility in the PEDOT:PSS or PTAA HTL, e) acceptor density in the PEDOT:PSS or PTAA HTL and f) perovskite hole and electron mobility. Real device data is overlaid as dotted lines, showing fast (752 V s^{-1}) reverse J-V scans of the champion devices when fresh (blue dotted line) and after 288 hours of aging (red dotted line).

The larger increase in background hole density during aging is not likely to be due to chemical interaction between PTAA and the perovskite, which is relatively inert and has been used to fabricate stable neat-Pb perovskite solar cells.[56] Rather, it is proposed that the suspected chemical interaction between the perovskite and PEDOT:PSS counteracts p-doping. Significant iodide vacancy formation is expected to n-dope perovskites.[39] Hence, a p-doping process (such as tin vacancy formation) would be counteracted by increased iodide vacancy formation. This mechanism has been previously experimentally observed in $CsSnI_3$.[57] Additionally, it is possible that HI produced by the reaction between acidic PEDOT:PSS and perovskite further acts as a reducing agent to counteract p-doping processes. Such a mechanism is completely consistent with both the increased bias-induced mobile ion accumulation-related performance losses observed in devices using PEDOT:PSS, and the increased background carrier density observed when the lead-tin perovskite is aged on PTAA. This mechanism is illustrated in Figure 4.25.

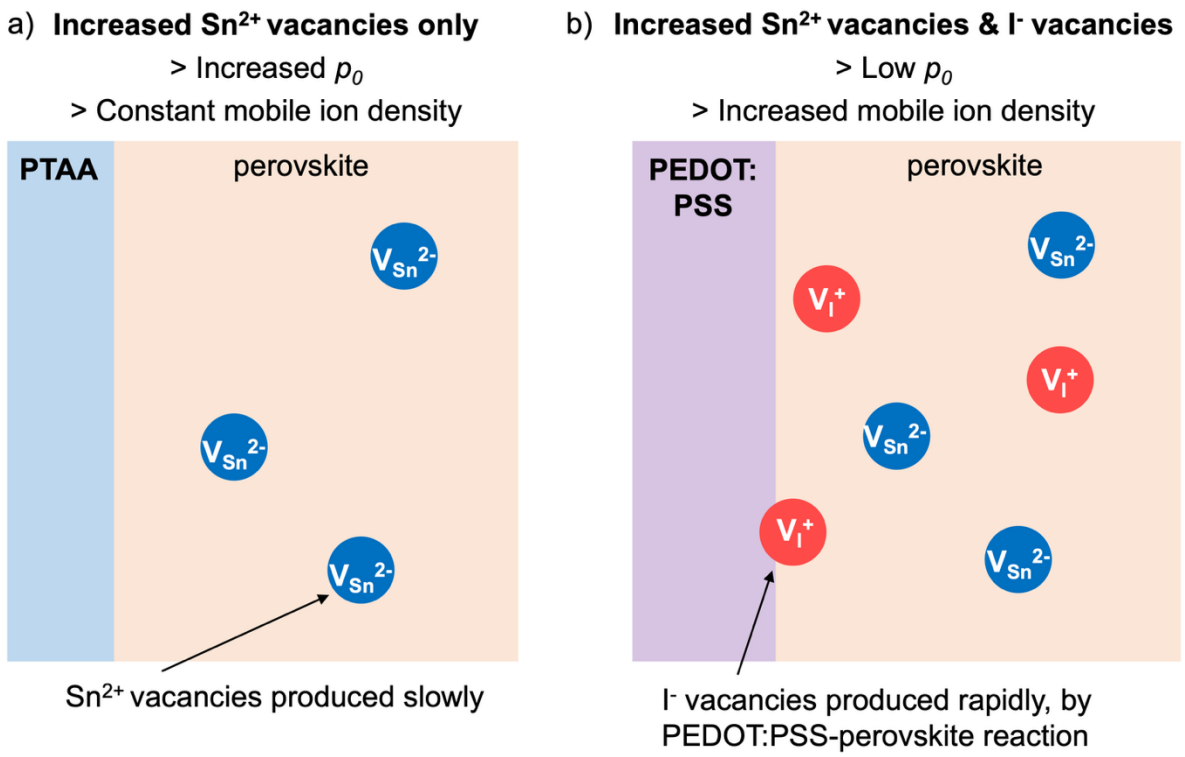


Figure 4.25. Diagram illustrating a mechanism consistent with the observed differences in the behaviour of lead-tin perovskite solar cells with PTAA or PEDOT:PSS HTLs after aging. a) Devices using PTAA are proposed to mainly experience an increase in low mobility p-doping defects (such as the Sn2+ vacancies shown here) during aging, resulting in an increased background hole density p_0 but a constant mobile ion density. b) Devices using PEDOT:PSS are proposed to additionally experience an increase in mobile I- vacancy density. This counteracts the effect of the p-doping defects on the Fermi level, keeping the background hole density p_0 low.

This indicates that whilst reducing the rate of iodide vacancy formation in lead-tin perovskite devices will reduce rapid-mobile ion related losses, it will eventually allow p-doping related losses to increase as demonstrated in devices using PTAA. The effect of iodide vacancy formation on the PCE of lead-tin perovskite devices will hence depend on the balance between their negative impact on internal field screening and recombination during device operation, and their positive impact counteracting p-doping. Ultimately, both iodide vacancy formation and p-doping must be avoided to achieve target stabilities.

Whilst it has been demonstrated that the increase in background hole density in encapsulated lead-tin perovskite films and devices during aging is much slower than in

devices exposed to air or in neat-Sn perovskites, these results indicate that it becomes a limiting factor after ~150 hours of aging under illumination and heat. Further research is necessary to clarify whether this self-doping process can be ascribed to the slow ingress of oxygen (and can hence be avoided by even better encapsulation), or to some other chemical interaction within the device (for example with residual DMSO[58]).

4.7 Conclusion & outlook on lead-tin perovskite stability

In conclusion, this chapter revealed four different degradation modes affecting the performance of lead-tin perovskite solar cells during encapsulated aging under elevated temperatures (65 °C) and illumination. Losses due to an increased density of mobile ions occur within days, those due to increased non-radiative recombination and p-doping occur over weeks, and the separation of a $CsSnI_3$ phase occurs over months.

The bias-induced accumulation of mobile ions during device operation is the primary degradation mode in devices using PEDOT:PSS, and is significantly mitigated when using the hole conductor PTAA. This is ascribed to an increase in iodide vacancy density in devices using PEDOT:PSS during aging, occurring due to chemical interaction between the perovskite and PSS. Avoiding charge transport materials that readily react with iodide in the perovskite is hence essential to improving stability of lead-tin PSCs. These losses are strongly reduced in devices using PTAA, but not entirely eliminated. Hence, developing a better understanding of iodine chemistry within the entire device architecture to further reduce iodide vacancy formation during aging can likely contribute to further stability improvements for all types of perovskite solar cells.

Although lead-tin PSCs employing PTAA are less affected by bias-induced mobile ion accumulation related losses during aging, the performance losses resulting from an increased p-doping during aging lead to comparable overall degradation as devices using

PEDOT:PSS over a few hundred hours. The increased p-doping in these devices is not caused by PTAA directly, but rather a process inherent to the lead-tin perovskite material which is counteracted by the formation of iodide vacancies by PEDOT:PSS. Although PCE losses from self-p-doping occur on slower timescales than those from rapid-moving ions, they too must be addressed to achieve target stability. It is probable that same defect which increases non-radiative recombination during aging is also responsible for the eventual increase in p-doping. To improve the stability of lead-tin perovskite solar cells, a better understanding of the type of recombination-active defects that develop in lead-tin perovskites during aging must be developed.

Of tertiary importance is slowing the formation of the δ-$CsSnI_3$ phase observed after weeks to months of aging, which may necessitate adjusting the perovskite composition. Understanding the potential impact of this phase and avoiding its formation may also contribute to the reduction of non-radiative recombination related losses.

The emerging picture is that the lead-tin perovskite phase is quite stable under combined heat and light stressing when well-protected from air exposure. However, small-scale changes in point defect chemistry strongly affect device performance by causing an increase in non-radiative recombination and self-p-doping, and the density of mobile ions. The kinetics of these changes are demonstrated to be strongly affected by chemical interaction between the perovskite and HTL.

Overall, if acidic PEDOT:PSS can be avoided, the main hurdle to making lead-tin perovskite solar cells as stable as their neat-Pb counterparts is stopping the observed increase in non-radiative recombination rates and self-p-doping during aging. This will require a better understanding of the changes in defect chemistry causing this degradation. If these changes can be slowed, for example by targeted passivation strategies, I expect that lead-tin PSCs will be no less stable than standard lead-based PSCs. These results are highly encouraging for the

realization of efficient and stable multi-junction thin-film PSCs and define a clear direction for future efforts to improve the stability of lead-tin PSCs.

4.8 Works cited

1. Hu, S. *et al. Optimized Carrier Extraction at Interfaces for 23.6% Efficient Tin–Lead Perovskite Solar Cells*. https://www.researchsquare.com/article/rs-727823/v1 (2021).
2. Lin, R. *et al.* All-perovskite tandem solar cells with 3D/3D bilayer perovskite heterojunction. *Nature* (2023).
3. Wang, Z. *et al.* Suppressed phase segregation for triple-junction perovskite solar cells. *Nature* **618**, 74–79 (2023).
4. Khenkin, M. V. *et al.* Consensus statement for stability assessment and reporting for perovskite photovoltaics based on ISOS procedures. *Nat Energy* **5**, 35–49 (2020).
5. Mauersberger, P. & Huber, F. Structure of caesium triiodostannate(II). *Acta Crystallogr B Struct Sci* **36**, 683–684 (1980).
6. Chung, I. *et al.* $CsSnI_3$: Semiconductor or Metal? High Electrical Conductivity and Strong Near-Infrared Photoluminescence from a Single Material. High Hole Mobility and Phase-Transitions. *J. Am. Chem. Soc.* **134**, 8579–8587 (2012).
7. Lim, V. J. -Y. *et al.* Air-Degradation Mechanisms in Mixed Lead-Tin Halide Perovskites for Solar Cells. *Advanced Energy Materials* 2200847 (2022).
8. Qiu, X. *et al.* From unstable CsSnI3 to air-stable Cs2SnI6: A lead-free perovskite solar cell light absorber with bandgap of 1.48 eV and high absorption coefficient. *Solar Energy Materials and Solar Cells* **159**, 227–234 (2017).
9. Xu, S., Libanori, A., Luo, G. & Chen, J. Engineering bandgap of CsPbI3 over 1.7 eV with enhanced stability and transport properties. *iScience* **24**, 102235 (2021).
10. Goldstein, J. I. *et al. Scanning Electron Microscopy and X-Ray Microanalysis*. (Springer New York, New York, NY, 2018).
11. Stoumpos, C. C., Malliakas, C. D. & Kanatzidis, M. G. Semiconducting Tin and Lead Iodide Perovskites with Organic Cations: Phase Transitions, High Mobilities, and Near-Infrared Photoluminescent Properties. *Inorg. Chem.* **52**, 9019–9038 (2013).
12. Carron, R. *et al.* Bandgap of thin film solar cell absorbers: A comparison of various determination methods. *Thin Solid Films* **669**, 482–486 (2019).
13. Thiesbrummel, J. *et al.* Universal Current Losses in Perovskite Solar Cells Due to Mobile Ions. *Adv. Energy Mater.* **11**, 2101447 (2021).
14. Pena-Camargo, F. *et al.* Revealing the doping density in perovskite solar cells and its impact on device performance. *Applied Physics Reviews* (2022).
15. Lim, J. *et al.* Long-range charge carrier mobility in metal halide perovskite thin-films and single crystals via transient photo-conductivity. *Nat Commun* **13**, 4201 (2022).
16. Davies, C. L. *et al.* Bimolecular recombination in methylammonium lead triiodide perovskite is an inverse absorption process. *Nat Commun* **9**, 293 (2018).
17. Kamaraki, C. *et al.* Charting the Irreversible Degradation Modes of Low Bandgap Pb-Sn Perovskite Compositions for De-Risking Practical Industrial Development. *Advanced Energy Materials* 2302916 (2024).
18. Meggiolaro, D., Ricciarelli, D., Alasmari, A. A., Alasmary, F. A. S. & De Angelis, F. Tin versus Lead Redox Chemistry Modulates Charge Trapping and Self-Doping in Tin/Lead Iodide Perovskites. *J. Phys. Chem. Lett.* **11**, 3546–3556 (2020).

19. Leijtens, T., Prasanna, R., Gold-Parker, A., Toney, M. F. & McGehee, M. D. Mechanism of Tin Oxidation and Stabilization by Lead Substitution in Tin Halide Perovskites. *ACS Energy Lett.* **2**, 2159–2165 (2017).
20. Lanzetta, L. *et al.* Degradation mechanism of hybrid tin-based perovskite solar cells and the critical role of tin (IV) iodide. *Nat Commun* **12**, 2853 (2021).
21. Webb, T. & Haque, S. A. A comparison of molecular iodine evolution on the chemistry of lead and tin perovskites. *Energy Environ. Sci.* **17**, 3244–3269 (2024).
22. Sanchez-Diaz, J. *et al.* Tin perovskite solar cells with >1,300 h of operational stability in N2 through a synergistic chemical engineering approach. *Joule* **6**, 861–883 (2022).
23. Stolterfoht, M. *et al.* Approaching the Fill Factor Shockley Queisser Limit in Stable, Dopant-Free Triple Cation Perovskite Solar Cells. *Energy & Environmental Science* **10**, 1530 (2017).
24. Rombach, F. M., Haque, S. A. & Macdonald, T. J. Lessons learned from spiro-OMeTAD and PTAA in perovskite solar cells. *Energy Environ. Sci.* **14**, 5161–5190 (2021).
25. Singh, S., Siliavka, E., Löffler, M. & Vaynzof, Y. Impact of Buried Interface Texture on Compositional Stratification and Ion Migration in Perovskite Solar Cells. *Adv Funct Materials* 2402655 (2024).
26. Wang, Q., Chueh, C.-C., Eslamian, M. & Jen, A. K.-Y. Modulation of PEDOT:PSS pH for Efficient Inverted Perovskite Solar Cells with Reduced Potential Loss and Enhanced Stability. *ACS Appl. Mater. Interfaces* **8**, 32068–32076 (2016).
27. Milot, R. L. *et al.* Radiative Monomolecular Recombination Boosts Amplified Spontaneous Emission in $HC(NH_2)_2SnI_3$ Perovskite Films. *J. Phys. Chem. Lett.* **7**, 4178–4184 (2016).
28. Mundt, L. E. *et al.* Surface-Activated Corrosion in Tin–Lead Halide Perovskite Solar Cells. *ACS Energy Lett.* **5**, 3344–3351 (2020).
29. Prasanna, R. *et al.* Design of low bandgap tin–lead halide perovskite solar cells to achieve thermal, atmospheric and operational stability. *Nat Energy* **4**, 939–947 (2019).
30. Eames, C. *et al.* Ionic transport in hybrid lead iodide perovskite solar cells. *Nat Commun* **6**, 7497 (2015).
31. Pering, S. R. & Cameron, P. J. The effect of multiple ion substitutions on halide ion migration in perovskite solar cells. *Mater. Adv.* **3**, 7918–7924 (2022).
32. Tress, W. *et al.* Understanding the rate-dependent J–V hysteresis, slow time component, and aging in $CH_3NH_3PbI_3$ perovskite solar cells: the role of a compensated electric field. *Energy Environ. Sci.* **8**, 995–1004 (2015).
33. Thiesbrummel, J. *et al.* Ion-induced field screening as a dominant factor in perovskite solar cell operational stability. *Nat Energy* (2024).
34. Zhang, X. *et al.* Rapid degradation behavior of encapsulated perovskite solar cells under light, bias voltage or heat fields. *Nanoscale Adv.* **3**, 6128–6137 (2021).
35. Le Corre, V. M. *et al.* Quantification of Efficiency Losses Due to Mobile Ions in Perovskite Solar Cells via Fast Hysteresis Measurements. *Solar RRL* **6**, 2100772 (2022).
36. Barboni, D. & De Souza, R. A. The thermodynamics and kinetics of iodine vacancies in the hybrid perovskite methylammonium lead iodide. *Energy Environ. Sci.* **11**, 3266–3274 (2018).

37. Tammireddy, S. *et al.* Temperature-Dependent Ionic Conductivity and Properties of Iodine-Related Defects in Metal Halide Perovskites. *ACS Energy Lett.* **7**, 310–319 (2022).
38. Futscher, M. H. *et al.* Quantification of ion migration in $CH_3NH_3PbI_3$ perovskite solar cells by transient capacitance measurements. *Mater. Horiz.* **6**, 1497–1503 (2019).
39. Bitton, S. & Tessler, N. Perovskite ionics – elucidating degradation mechanisms in perovskite solar cells *via* device modelling and iodine chemistry. *Energy Environ. Sci.* **16**, 2621–2628 (2023).
40. Wang, H., Guerrero, A., Bou, A., Al-Mayouf, A. M. & Bisquert, J. Kinetic and material properties of interfaces governing slow response and long timescale phenomena in perovskite solar cells. *Energy Environ. Sci.* **12**, 2054–2079 (2019).
41. Tirawat, R. *et al.* Measuring metal halide perovskite single cell degradation consistent with module-based conditions. *Sustainable Energy Fuels* **8**, 546–553 (2024).
42. Senanayak, S. P. *et al.* Charge transport in mixed metal halide perovskite semiconductors. *Nat. Mater.* **22**, 216–224 (2023).
43. Dey, K. *et al.* Substitution of Lead with Tin Suppresses Ionic Transport in Halide Perovskite Optoelectronics.
44. Courtier, N. E., Cave, J. M., Walker, A. B., Richardson, G. & Foster, J. M. IonMonger: a free and fast planar perovskite solar cell simulator with coupled ion vacancy and charge carrier dynamics. *J Comput Electron* **18**, 1435–1449 (2019).
45. Ke, Q. B., Wu, J.-R., Lin, C.-C. & Chang, S. H. Understanding the PEDOT:PSS, PTAA and P3CT-X Hole-Transport-Layer-Based Inverted Perovskite Solar Cells. *Polymers* **14**, 823 (2022).
46. Lee, M. M., Teuscher, J., Miyasaka, T., Murakami, T. N. & Snaith, H. J. Efficient Hybrid Solar Cells Based on Meso-Superstructured Organometal Halide Perovskites. *Science* **338**, 643–647 (2012).
47. Kerner, R. A., Xu, Z., Larson, B. W. & Rand, B. P. The role of halide oxidation in perovskite halide phase separation. *Joule* **5**, 2273–2295 (2021).
48. Lee, S. *et al.* Buried interface modulation via PEDOT:PSS ionic exchange for the Sn-Pb mixed perovskite based solar cells. *Chemical Engineering Journal* **479**, 147587 (2024).
49. Meng, Y. *et al.* Improving the Stability of Bulk Heterojunction Solar Cells by Incorporating pH-Neutral PEDOT:PSS as the Hole Transport Layer. *ACS Appl. Mater. Interfaces* **6**, 5122–5129 (2014).
50. Zhan, C. *et al.* Indium Tin Oxide Induced Internal Positive Feedback and Indium Ion Transport in Perovskite Solar Cells. *Angew Chem Int Ed* **63**, e202403824 (2024).
51. Xia, Y., Yan, G. & Lin, J. Review on Tailoring PEDOT:PSS Layer for Improved Device Stability of Perovskite Solar Cells. *Nanomaterials* **11**, 3119 (2021).
52. Wu, D. *et al.* Enhancing the Efficiency and Stability of Tin-Lead Perovskite Solar Cells via Sodium Hydroxide Dedoping of PEDOT:PSS. *Small Methods* 2400302 (2024).
53. Diekmann, J. *et al.* Determination of Mobile Ion Densities in Halide Perovskites via Low-Frequency Capacitance and Charge Extraction Techniques. *J. Phys. Chem. Lett.* **14**, 4200–4210 (2023).
54. Savill, K. J. *et al.* Impact of Tin Fluoride Additive on the Properties of Mixed Tin-Lead Iodide Perovskite Semiconductors. *Adv. Funct. Mater.* **30**, 2005594 (2020).

55. Burgelman, M., Nollet, P. & Degrave, S. Modelling polycrystalline semiconductor solar cells. *Thin Solid Films* **361–362**, 527–532 (2000).
56. Saliba, M. *et al.* Incorporation of rubidium cations into perovskite solar cells improves photovoltaic performance. *Science* **354**, 206–209 (2016).
57. Rajendra Kumar, G., Kim, H.-J., Karupannan, S. & Prabakar, K. Interplay between Iodide and Tin Vacancies in $CsSnI_3$ Perovskite Solar Cells. *J. Phys. Chem. C* **121**, 16447–16453 (2017).
58. Pascual, J. *et al.* Origin of Sn(II) oxidation in tin halide perovskites. *Mater. Adv.* **1**, 1066–1070 (2020).

5 Extrinsic doping of lead-tin perovskites

5.1 Overview

Compared to neat lead perovskites, mixed lead-tin perovskites experience increased self-p-doping that may hinder their efficiencies in solar cells. The ability to control the long-term stability and the self-p-doping level is of central importance for the full exploitation of lead-tin perovskites in solar cells. Reducing the background hole density below 10^{15} cm^{-3} is expected to improve energetic alignment,[1] as well as reduce loss pathways involving the recombination of photo-excited electrons with the hole background.[2] This motivates the search for ways to tune the E_F of lead-tin perovskites to make them less p-type.

Bi^{3+} and Sb^{3+} ions appear as a natural choice for n-doping, due to their comparable ionic radius to Pb^{2+} and the similar electronic structure. They are suggested to n-dope by incorporating in the perovskite at the B-cation position in their 3+ charge state (Figure 5.1).[3,4] Previous experimental works, however, have highlighted the emergence of deep trap states associated with the Bi^{3+} dopant in neat lead perovskites, strongly impacting the optoelectronic properties by increased non-radiative recombination.[5–8] Such observations are in agreement with theoretical predictions.[3,4] Recent computational studies on neat-Sn perovskite compositions found that both Bi and Sb introduce deep recombination levels even when lead was entirely substituted by Sn.[9] A recent investigation on the effects of relatively large concentrations of Bi doping (1%+) of mixed lead-tin perovskites found that Bi also induces increased non-radiative recombination in these materials.[10] Although Sb^{3+} doping has also been indicated to slightly n-dope neat lead perovskites, it has not been as widely explored.[10,11] The effects of small densities of both Bi^{3+} and Sb^{3+} doping on lead-tin perovskites hence remain unexplored.

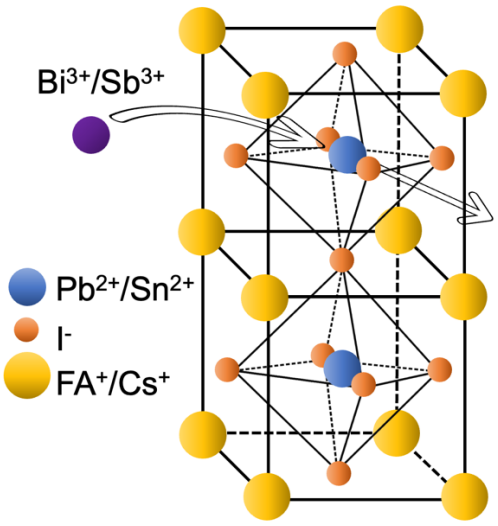


Figure 5.1 Schematic illustrating trivalent doping of hybrid lead-tin perovskites. Bi^{3+} or Sb^{3+} incorporate at the substitutional Pb^{2+} site.

In this chapter, the impact of Bi^{3+} and Sb^{3+} metal dopants on the optoelectronic properties of mixed lead-tin perovskites was investigated. A wide range of dopant concentrations down to 0.01 ppm are explored, and it is found that Bi^{3+} doping densities as low as 1 ppm (corresponding to a Bi^{3+} density of ~10^{15} cm^{-3} in the film) severely quench the photoluminescence of the perovskite. Sb^{3+} doping is also found to quench photoluminescence, but only at significantly higher densities of 100 ppm. The observed increase in non-radiative recombination is rationalized using DFT simulations. These show that both Bi^{3+} and Sb^{3+} can incorporate into the lattice of lead-tin perovskites, but induce deep electron traps in the band gap, similarly to what has been previously observed in neat lead perovskites. The disastrous impact of very small amounts of Bi^{3+} on the optoelectronic quality of the perovskite poses serious concerns regarding its presence as a potential impurity in perovskite precursor chemicals. Motivated by this, chemical impurity analysis of different precursor powders was carried out and found that in some precursors Bi is present in amounts that could affect perovskite quality. In response, a strategy to remove Bi^{3+} impurities from

perovskite precursor chemicals based on reduction by Sn^0 metal was developed and validated.

The work presented in this chapter stems from a collaboration between 5 different institutions which was led by me. In particular, the DFT calculations, high resolution EQE, and ICP-MS measurements were carried out by collaborators and specific attributions are detailed in the text and in the methods (Chapter 3).

5.2 Optoelectronic quality of Bi^{3+} and Sb^{3+}-doped lead-tin perovskite films

To investigate the effects of Bi^{3+} and Sb^{3+} doping on the optoelectronic properties of mixed lead-tin perovskites, perovskite films with 0.001 ppm (10^{-7} % in the precursor solution, or 1×10^{12} cm^{-3} in the films) to 50'000 ppm (5 %, or 5×10^{19} cm^{-3}) dopant were fabricated. As SbI_3 was found to be less soluble in the precursor solvents, it could only be investigated up to a doping density of 1000 ppm (0.1%, or 1×10^{18} cm^{-3}). Bi^{3+} and Sb^{3+} are expected to be incorporated into the perovskite lattice at the metal cation position (Figure 5.1). Although the dopant added to the precursor solution may not entirely incorporate in the perovskite bulk at the higher concentrations, the density of incorporated dopant is expected to follow the trend of dopant precursor concentration. For example, for Bi doping of $MAPbBr_3$, it has been shown that Bi is incorporated into the lattice at approximately the same concentration as $BiBr_3$ in the perovskite precursor solution.[7] Throughout this chapter, references to dopant density refer to the concentration of dopant added to the perovskite precursor solution, with respect to the sum of the lead and tin concentrations.

Perovskite thin films were successfully deposited by solution processing from precursors containing the Bi^{3+} and Sb^{3+} doping densities described, with no significant visible differences in film drying and curing. These films were characterized by X-ray diffraction (XRD) (Figure 5.2a), and it was found that the original lead-tin perovskite phase is unchanged for all concentrations of Bi^{3+} and Sb^{3+} tested. Optical measurements of both Bi^{3+} and Sb^{3+}-doped films confirm this by showing no shift in band gap for the full range of doping densities. A slight reduction in XRD scattering peak intensity was observed at Bi^{3+} densities above 5'000 ppm. When 50'000 ppm Bi^{3+} was added, two new XRD peaks corresponding to BiI_3 were also observed, suggesting that at this precursor concentration there is a significant amount of excess Bi^{3+} which is not incorporated in the perovskite crystal. This is consistent with previous studies on single crystals of Bi doped $MAPbBr_3$, where Bi incorporation could be observed up to around 50'000 ppm doping.[7,6] The PL peak position was also measured, and no change in either the position or the shape of the PL emission peak was found (Figure 5.2b). Whilst previous investigations of Bi^{3+} doping in $MAPbBr_3$ observed an enhanced emission in the region of 1000-1080 nm in the doped films,[6–8] in this case no new emission peaks were observed at longer wavelengths, up to the detector limit of 1400 nm.

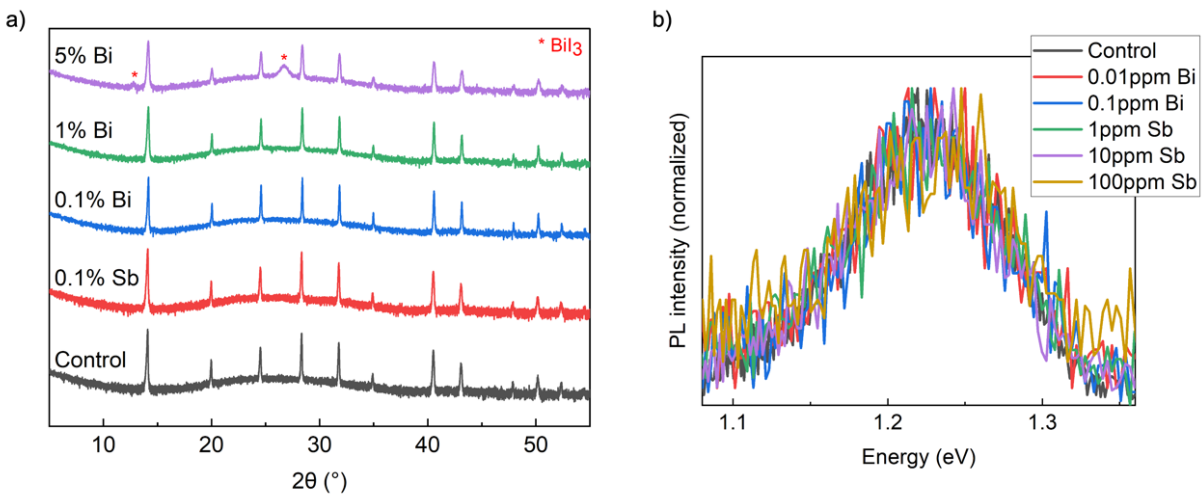


Figure 5.2. a) X-ray diffraction (XRD) measurements of $FA_{0.83}Cs_{0.17}Pb_{0.5}Sn_{0.5}I_3$ films doped with various concentrations of Bi^{3+} and Sb^{3+}, with intensity scaled on a log scale. b) Steady-state photoluminescence peaks of lead-tin perovskite films doped with various densities of BiI_3 or SbI_3, measured during rapid (40MHz) pulsed excitation with a 630 nm laser.

To map the effect of Bi^{3+} and Sb^{3+} doping on the optoelectronic quality of the lead-tin perovskite films, PLQE measurements were performed. These are representative of the ratio of radiative to total recombination in the films. Samples were excited with a red 660 nm laser at an intensity which resulted in an absorbed photon flux equivalent to 1-sun conditions for a 1.25 eV bandgap material. Surprisingly, very small amounts of Bi^{3+} doping led to a severe decrease in the PLQE of the lead-tin perovskite films (Figure 5.3a), with the addition of 1 ppm Bi^{3+} causing an ~80% reduction in PLQE with respect to undoped samples. To confirm, TRPL decay measurements were also performed on the same samples, and the tails of the decays were fitted with a mono-exponential decay (Figure 5.4a). The dynamics show an identical trend to the PLQE, with 1 ppm Bi^{3+} causing a ~10-fold decrease in lifetime with respect to controls. This suggests that the addition of even very small densities of Bi^{3+} severely increases the rate of non-radiative recombination in lead-tin perovskites. This is consistent with previous observations of Bi^{3+} doping in neat lead perovskites, in which 10 ppm Bi^{3+} was observed to already reduce device performance.[5] Doping the lead-tin perovskite

in the same manner with Sb^{3+} revealed that this dopant similarly increases non-radiative recombination rates in the perovskite films, but at significantly higher concentrations of 100-1000 ppm (Figure 5.3b, Figure 5.4b).

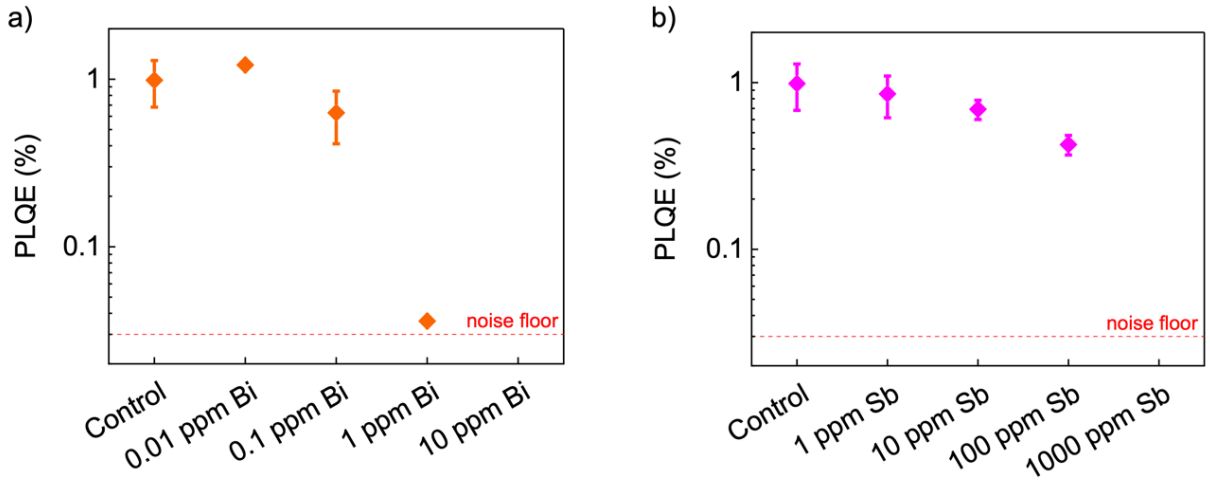


Figure 5.3. PLQE of lead-tin perovskite films doped with small quantities of i) Bi^{3+} or ii) Sb^{3+}.

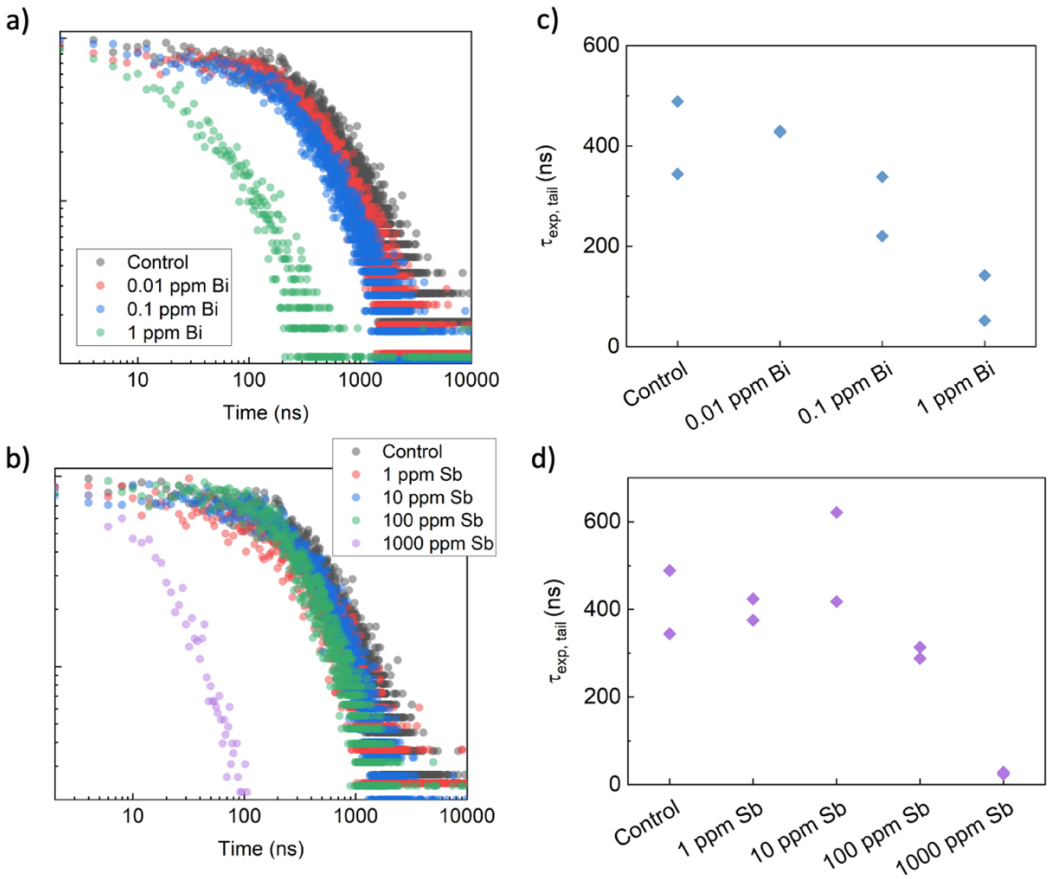


Figure 5.4 a), b) Normalized time-resolved photoluminescence decays of lead-tin perovskite films doped with small quantities of Bi^{3+} and Sb^{3+}. Decays were measured with a repetition rate of 10 kHz and using a 630 nm with an excitation density of 3.1 nJ cm^{-2} $pulse^{-1}$ and a spot size of 2.4 x 10^{-3} cm^2. c), d) Photoluminescence lifetimes resulting from monoexponential fits to the decays presented in a) and b). Fits were performed from 200 ns until the point in the decay where the signal-to-noise ratio fell below 2. For decays with lifetimes shorter than 200 ns, fits were performed on the 50 ns before the point in the decay where the signal-to-noise ratio fell below 2.

No significant changes to the above-bandgap absorption properties of Bi^{3+} and Sb^{3+}-doped films could be discerned as measured by UV-Vis-NIR transmission and reflectance spectrophotometry (Figure 5.5a). To probe more subtle changes that may occur in the sub-bandgap region of the absorption onset and tail, collaborators Dr. Stefan Zeiske (Northwestern University) and Dr. Ardalan Armin (Swansea University) performed ultra-sensitive EQE measurements on electrically contacted Bi^{3+}-doped lead-tin perovskite films.[12] Films doped with 10'000 ppm Bi^{3+} show a significant broadening of the EQE onset (Figure 5.5b). This can be ascribed to increased energetic disorder, which has previously also been observed by others in Bi^{3+}-doped neat Pb perovskites.[5–8] However, for films doped with 10 ppm Bi^{3+}, both EQE and absorptance spectra were found to be very similar to films without any Bi^{3+}, despite the PLQE being strongly quenched at this density. Analogously, there was also no change observed in the absorptance spectra of Sb^{3+}-doped films up to 1000 ppm density. Hence, it can be concluded that at impurity levels between 1-10 ppm for Bi^{3+} and above 100 ppm for Sb^{3+}, doping with these elements does not affect electronic disorder to an observable extent but does significantly increase the rate of non-radiative recombination. This would be consistent with the Bi^{3+} and Sb^{3+} dopants creating highly recombination-active traps in the perovskite, which cause rapid recombination even at densities that do not observably increase electronic disorder.

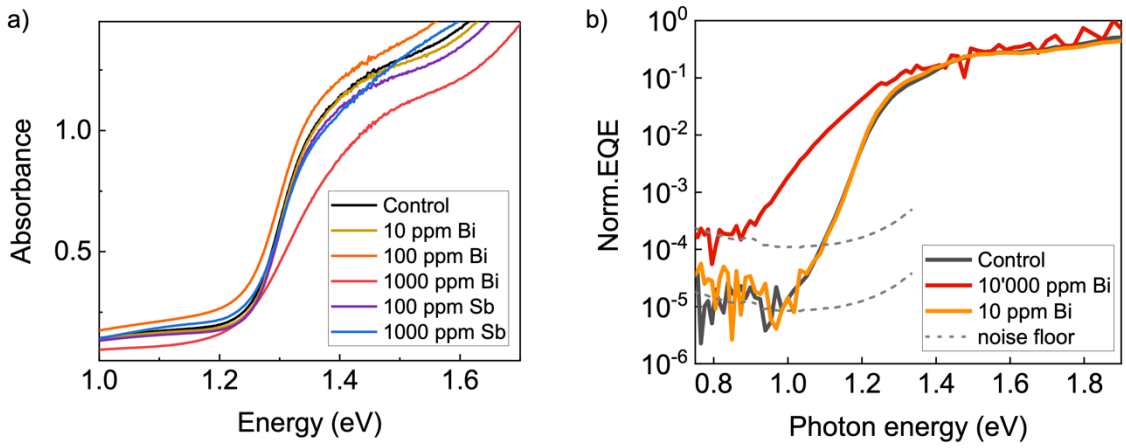


Figure 5.5. a) Absorbance around the band edge of lead-tin perovskite films doped with various amounts of Bi^{3+} and Sb^{3+}. b) Ultra-sensitive EQE measurements of electrically contacted lead-tin perovskite films doped with various amounts of Bi^{3+}.

5.3 DFT & PL simulations

The DFT calculations presented in this section were carried out by collaborators Dr. Daniele Meggiolario at the Istituto CNR di Scienze e Tecnologie Chimiche (SCITEC-CNR) in Perugia, and Dr. Luca Gregori at the University of Perugia. Figures 5.6, 5.7, 5.8 and 5.10 were also created by them.

To rationalize the observed impact of Bi^{3+} and Sb^{3+} on the lead-tin perovskite, DFT calculations were employed to investigate the efficacy of Bi^{3+} and Sb^{3+} incorporation and their effect on the electronic band structure and defect energies of $MAPb_{0.5}Sn_{0.5}I_3$. For simplicity, MA was selected as the monovalent cation for the DFT calculations. The choice of monovalent cation is not anticipated to significantly affect the calculated defect energies induced by group V metal doping, since the band structure near the CB minimum and VB maxima is predominantly influenced by the divalent metal and halide orbitals, and the crystal structure and lattice constant of a Fa/Cs mixed cation perovskite closely resemble those of the MA perovskite.

DFT analysis highlights that dopant incorporation is thermodynamically more favourable in substitutional positions to Pb and Sn compared to other lattice positions, such as interstitial or substitutional to the organic cation (Table 5.1). For both Bi and Sb, incorporation in the substitutional position to Pb is slightly more advantageous than on the Sn site, due to the more similar ionic radius of the dopants with lead. Consequently, the defect analysis was focused on dopants in substitutional position to Pb in the lattice. To provide accurate defect properties, the defect formation energies and thermodynamic ionization levels were calculated using the PBE0 hybrid functional (α=0.20)[13,14] and by including spin-orbit coupling (details in methods, Chapter 3). Results are shown in Figure 5.6.

Table 5.1. Defect formation energies (DFE) of Bi dopant in different positions of the $MAPb_{0.5}Sn_{0.5}I_3$ lattice, under stoichiometric growth conditions: interstitial position (Bi_i^{3+}), substitutional to the MA cation (Bi_{MA}^{2+}) and substitutional to the Pb / Sn metal (Bi_{Pb}^{+} / Bi_{Sn}^{+}). DFEs have been calculated at the PBE-D3 level of theory at the VBM of the perovskite.

Defect	DFE (eV)
Bi_i^{3+}	1.74
Bi_{MA}^{2+}	1.01
Bi_{Pb}^{+}	-0.03
Bi_{Sn}^{+}	0.11
Sb_{Pb}^{+}	-0.03
Sb_{Sn}^{+}	0.12

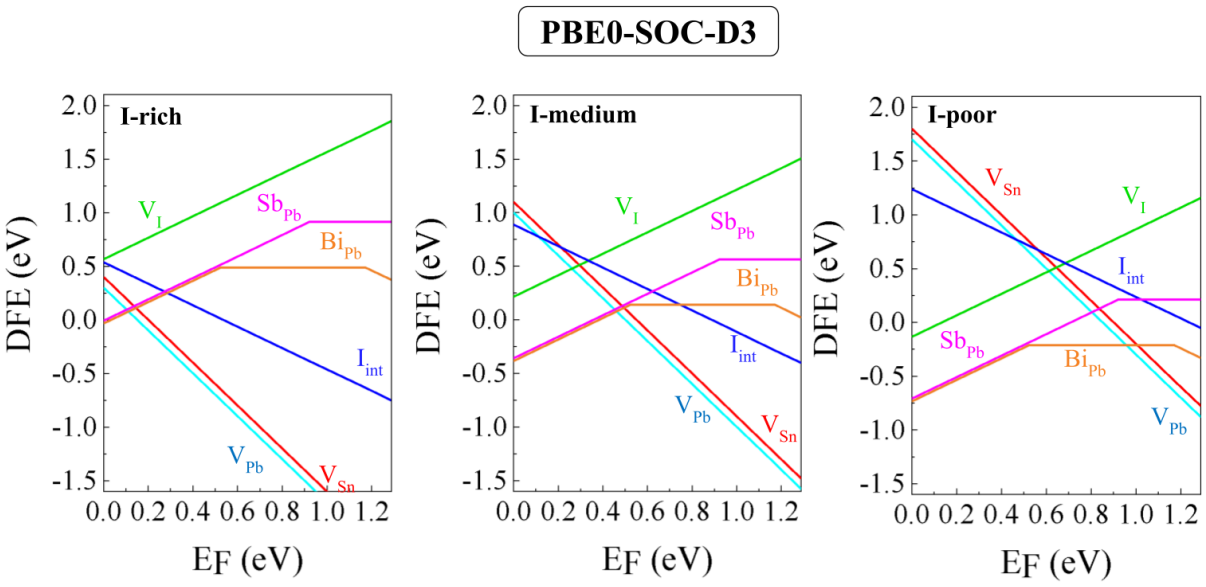


Figure 5.6. Defect formation energies of Bi and Sb dopants in substitutional positions to Pb in different conditions of growth of the $MAPb_{0.5}Sn_{0.5}I_3$ perovskites, as calculated at the PBE0-SOC-D3 (α=0.20) level of theory. This figure was created by D. Meggiolario and L. Gregori.

Figure 5.7a presents the calculated defect formation energies of substitutional dopants in I-medium growth conditions, compared to the defect formation energies of the most stable native defects in $MAPb_{0.5}Sn_{0.5}I_3$ (V_{Pb}^{2-}, V_{Sn}^{2-}, I_i^- and V_I^+). For Fermi levels up to 0.52 eV, the Bi dopant remains stable in the positive state of charge (+III oxidation state). At this point, a deep (+/0) transition occurs, and the neutral state becomes the stable form of the defect. In heavily n-doped perovskites, where the Fermi level approaches the conduction band, the negative form of the defect is also stable. Due to the similar ionic radius of Bi^{3+} (103 pm) and Pb^{2+} (119 pm), incorporation of Bi^{3+} in the Pb site results in minimal metal-iodide bond variation compared to the pristine perovskite (Figure 5.8). Analysis of the projected density of states for Bi_{Pb}^+ indicates that the dopant introduces a localized Kohn-Sham (KS) level in the perovskite's band gap, positioned approximately 1.0 eV above the VBM (Figure 5.7b). Upon photoexcitation, this state traps one electron, resulting in an occupied KS level 0.3 eV

above the VBM after lattice relaxation. The relaxation process is accompanied by an elongation of the Bi-I bond lengths, attributed to the population of the metal's antibonding state.

Compared to Bi, Sb is stable in the +III oxidation state across a broader Fermi level range. The positively charged state remains the most stable form of the defect up to 0.92 eV above the VBM, corresponding to the position of the (+/0) deep transition (Figure 5.6). Like Bi, Sb preferentially incorporates in the +III oxidation state under thermodynamic equilibrium (Sb_{Pb}^{+}). However, due to its smaller radius, Sb^{3+} induces a slight contraction of the metal-iodide bonds (Figure 5.8). The analysis of the electronic structure of the Sb_{Pb}^{+} defect reveals an unoccupied orbital below the CBM. Following electron trapping, an occupied KS level forms at approximately 0.6 eV above the VBM, as evidenced in the PDOS of the neutral charged state (Figure 5.7). The (+/0) ionization level of Sb occurs at a higher energy (0.9 eV above VBM) compared to Bi (0.5 eV above VBM), indicating that electrons can detrap from the Sb_{Pb}^{+} defect at a faster rate.

The defect equilibrium obtained after the incorporation of the dopants is predicted to have a significant impact on the charge carrier equilibrium density. In the pristine perovskite, the native Fermi level is placed at around 0.3 eV above the VBM and is mainly set by the equilibrium between iodine vacancies and lead vacancies. DFT calculations predict that the incorporation of Bi and Sb shift E_F by 0.2 eV towards the middle of the band gap (Figure 5.7a), with a decrease in hole density of around four orders of magnitude. If there were no other consequences of the Bi or Sb doping, this significant Fermi level shift would be advantageous.

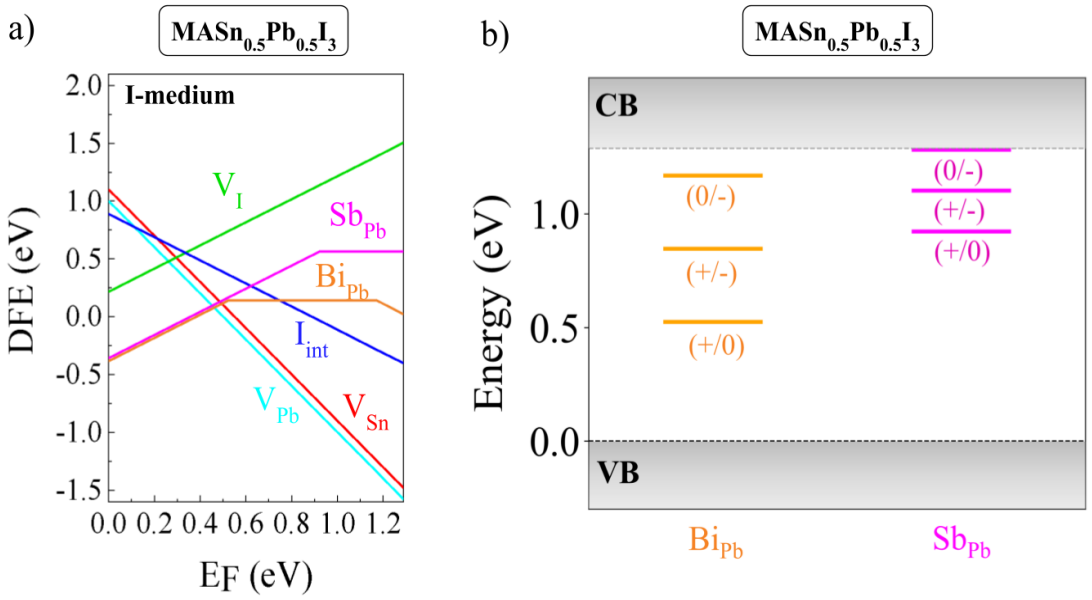


Figure 5.7. a) Defect formation energies of substitutional Bi_{Pb} and Sb_{Pb} dopants compared with the more stable native defects in $MAPb_{0.5}Sn_{0.5}I_3$ (I-medium conditions); b) associated thermodynamic ionization levels. Defect quantities have been calculated at PBE0-SOC (α=0.20) level of theory by including DFT-D3 dispersions. This figure was created by D. Meggiolario and L. Gregori.

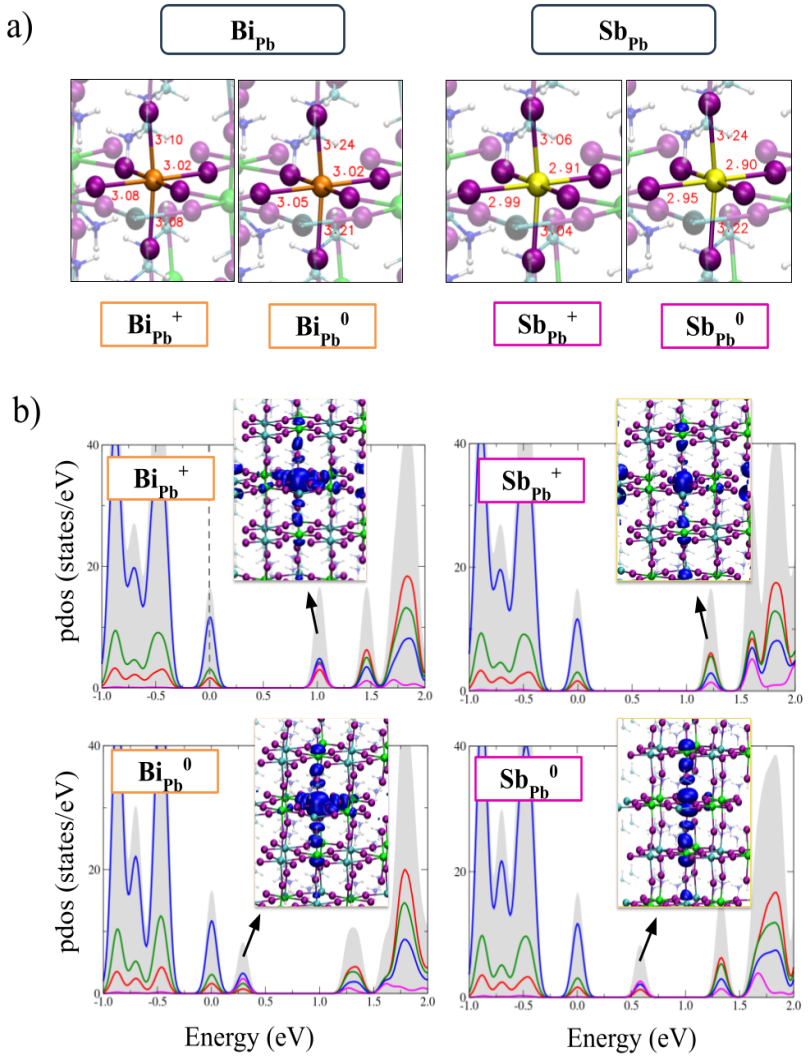


Figure 5.8. a) Equilibrium structures of the positive and neutral Bi_{Pb}, Sb_{Pb} defects; b) projected density of states (PDOS) of the same defects, highlighting the presence of deep trap states in the band gap of the perovskite (blue=I, red=Pb, green=Sn, purple=dopant). In the insets the plot of the LUMO (HOMO) Kohn-Sham (KS) orbitals of the positive (neutral) defects are reported. This figure was created by D. Meggiolario and L. Gregori.

If completely incorporated in the perovskite structure, the addition of 1 ppm Bi^{3+} would lead to a trap state density of 10^{15} cm^{-3} (substituting 0.0001% of the ~10^{21} cm^{-3} B-cation sites in the perovskite lattice). To investigate whether such a density of deep defects can completely explain the observed increase in non-radiative recombination, TRPL and PLQE simulations are presented in Figure 5.9. When modelling Bi as a mid-gap trap (0.625eV from CB) with

symmetrical hole and electron capture coefficients of 10^{-8} $cm^{-3}s^{-1}$, a density of 10^{15} cm^{-3} (equivalent to the full incorporation of 1 ppm Bi) can indeed closely replicate the reductions in PLQE and TRPL lifetimes observed in the films, with only a slight deviation in the early-time shape of the TRPL decay.

However, performing the same simulation with a shallower trap (0.35 eV from the CB) to simulate the effect of Sb doping shows that the shallower energy level of Sb in the perovskite lattice cannot completely explain the reduced impact on non-radiative recombination (Figure 5.9b). The TRPL and PLQE results can be well-reproduced when it is assumed that only 0.3% of the added Sb^{3+} incorporates in the perovskite lattice. Alternatively, the electron and hole capture coefficients of the Sb^{3+} defect may in reality be lower than estimated here. Based on DFT predictions, no remarkable differences in the incorporation energies of Bi and Sb have been observed. Hence, the less severe effect of Sb^{3+} doping on non-radiative recombination rates and energetic disorder may be explained by a combination of a shallower trap energy and a kinetic hindrance to the incorporation of Sb^{3+} ions which are more strongly solvated with respect to Bi^{3+} in the precursor solution.

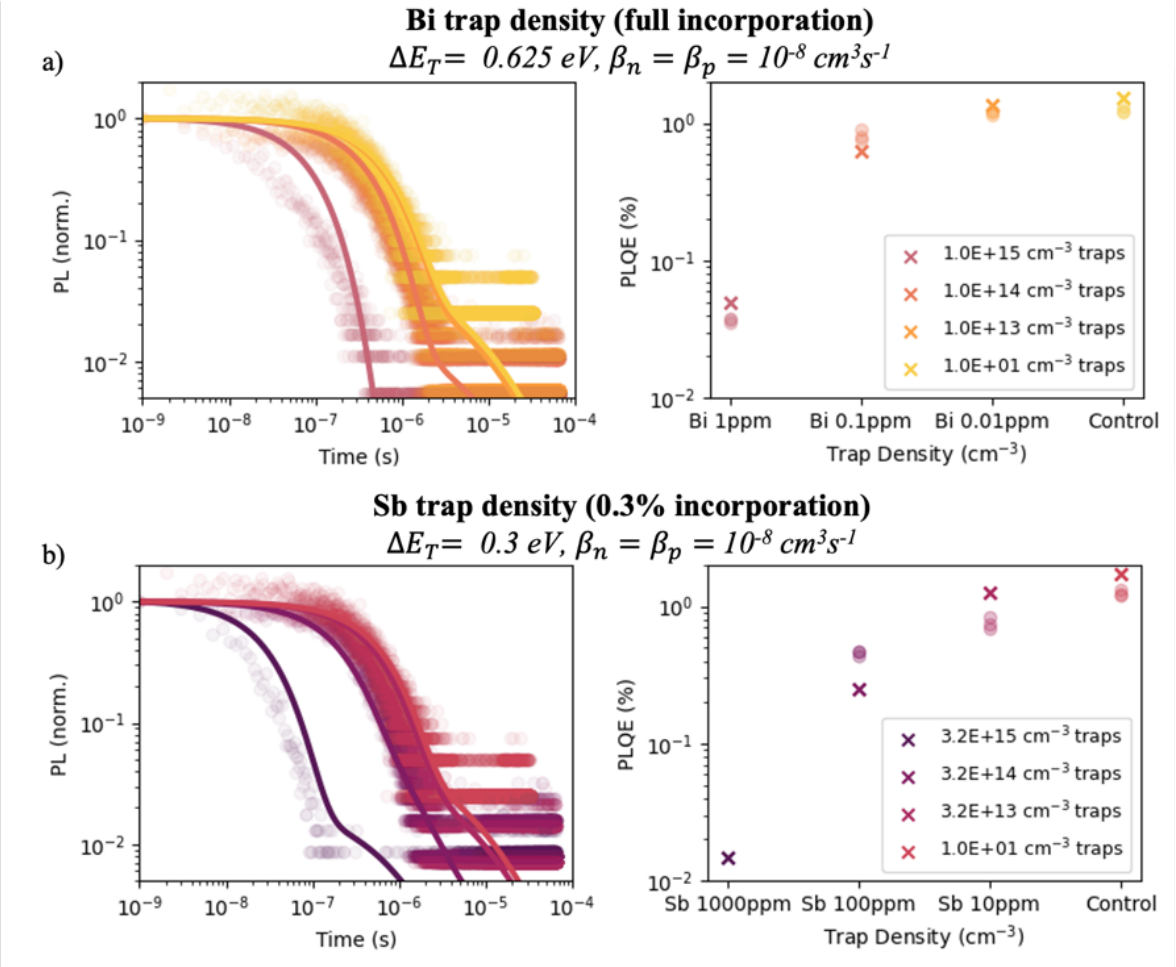


Figure 5.9. Simulated TRPL decays and PLQE values with varying trap types and densities. TRPL and PLQE variation with a) Bi^{3+} trap density variation (0.625 eV from CB, equal hole and electron capture coefficients of 10^{-8} cm^3 s^{-1}), b) Sb^{3+} trap density variation (0.3 eV from CB, equal hole and electron capture coefficients of 10^{-8} cm^3 s^{-1})

Previous computational studies on neat-lead perovskites demonstrated that non-radiative recombination on the Bi_{Pb}^{3+} defect is hindered by the presence of a thermodynamic barrier to recombination. The loss of performance of Bi^{3+}-doped perovskite solar cells was instead attributed to the Fermi level shift induced by the dopant, increasing the density of compensatory deep acceptor defects, specifically iodine interstitials, in the material.[15]

The non-radiative recombination of the hole on the neutral Bi_{Pb}^{0} defect was investigated by calculating the energy-coordinate diagram of the neutral and positive defect along distortion of the Bi-I bond (Figure 5.10). Unlike what was found for neat-lead

perovskites,[15] this diagram reveals only a small barrier (0.18 eV) to hole recombination, indicating that Bi incorporation likely directly enhances non-radiative recombination in the material.

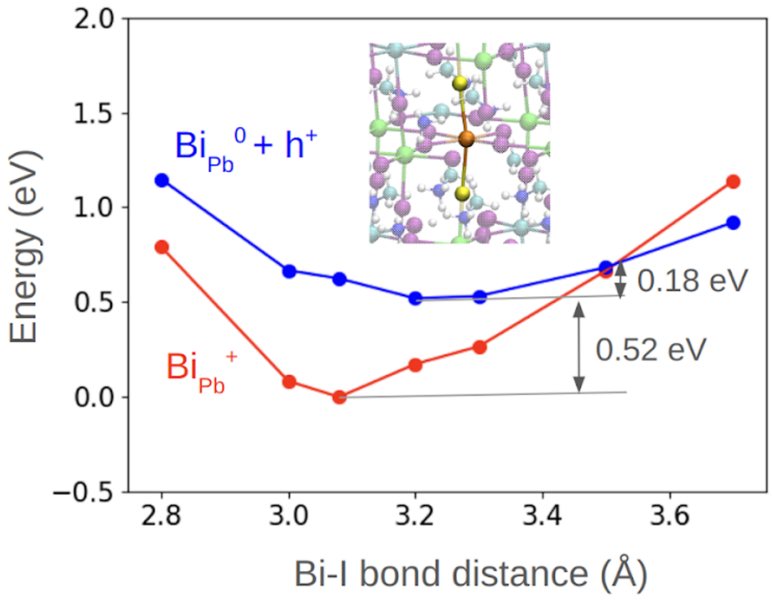


Figure 5.10. Energy-coordinate diagram for the non-radiative recombination of the hole on the Bi_{Pb}^{0} dopant site. The monitored coordinate is the bond distance between the Bi dopant and two apical I, reported in orange and yellow in the inset, respectively. The difference in energy between the minimum of the positive and the neutral state, i.e. the (+/0) transition, is that calculated at the PBE0-SOC-D3 level (0.52 eV), while distortions along the Bi-I bond are calculated at the PBE-D3 level. A barrier to recombination of 0.18 eV is estimated. This figure was created by D. Meggiolario and L. Gregori.

Defect formation energy analysis confirms that the incorporation of Bi^{3+} and Sb^{3+} is compensated by the formation of lead or tin vacancies $V_{Pb/Sn}^{2-}$, while the formation of compensating iodine interstitials I_i^- shows more unfavourable thermodynamics, see Table 5.2. Bi^{3+} doping is hence expected to cause a large increase in the $V_{Pb/Sn}^{2+}$ defects, and also some increase in I_i^- defects. However, unlike in neat-Pb perovskites, both of these defects were previously calculated to be relatively shallow defects in the bulk of mixed lead-tin

perovskites, with a distance from the VB not exceeding 0.15 eV.[16] It is hence possible that their recombination activity is limited.

Table 5.2. Simulated incorporation reactions of Bi and Sb dopants into the $MAPb_{0.5}Sn_{0.5}I_3$ perovskite and associated thermodynamics calculated at the PBE0-SOC level of theory.

Reaction	M = Bi	M = Sb
R1) $3/2\ Pb_{Pb} + MI_3 = M_{Pb}^{+} + 1/2\ V_{Pb}^{2-} + 3/2\ PbI_2$	0.12 eV	0.14 eV
R2) $Pb_{Pb} + MI_3 = M_{Pb}^{+} + I_i^{-} + PbI_2$	0.50 eV	0.53 eV

To test the effect of an increase in the density of these shallow defects, their effect on PLQE and TRPL decays was simulated (Figure 5.11a). Indeed, an increase in shallow defect density could not by itself recreate the severe decrease in PLQE and TRPL lifetime we observed without showing a strong trap-filling feature in the first 10 ns of the TRPL decay (not observed in the experimental data). However, increasing the shallow defect density in addition to a 10^{15} cm^{-3} Bi trap density produced simulations that match the experimental TRPL decay shape better (Figure 5.11b). Hence, these PL simulations suggest that compensatory shallow defects contribute to recombination processes, but Bi/Sb defects determine overall non-radiative recombination rates. It should be noted that this analysis is contingent on the assumed capture coefficients for the (shallow) compensatory defects. If these are significantly different, and particularly if the hole capture coefficient is unexpectedly stronger, these defects could contribute more strongly to the increased non-radiatively recombination than outlined here.

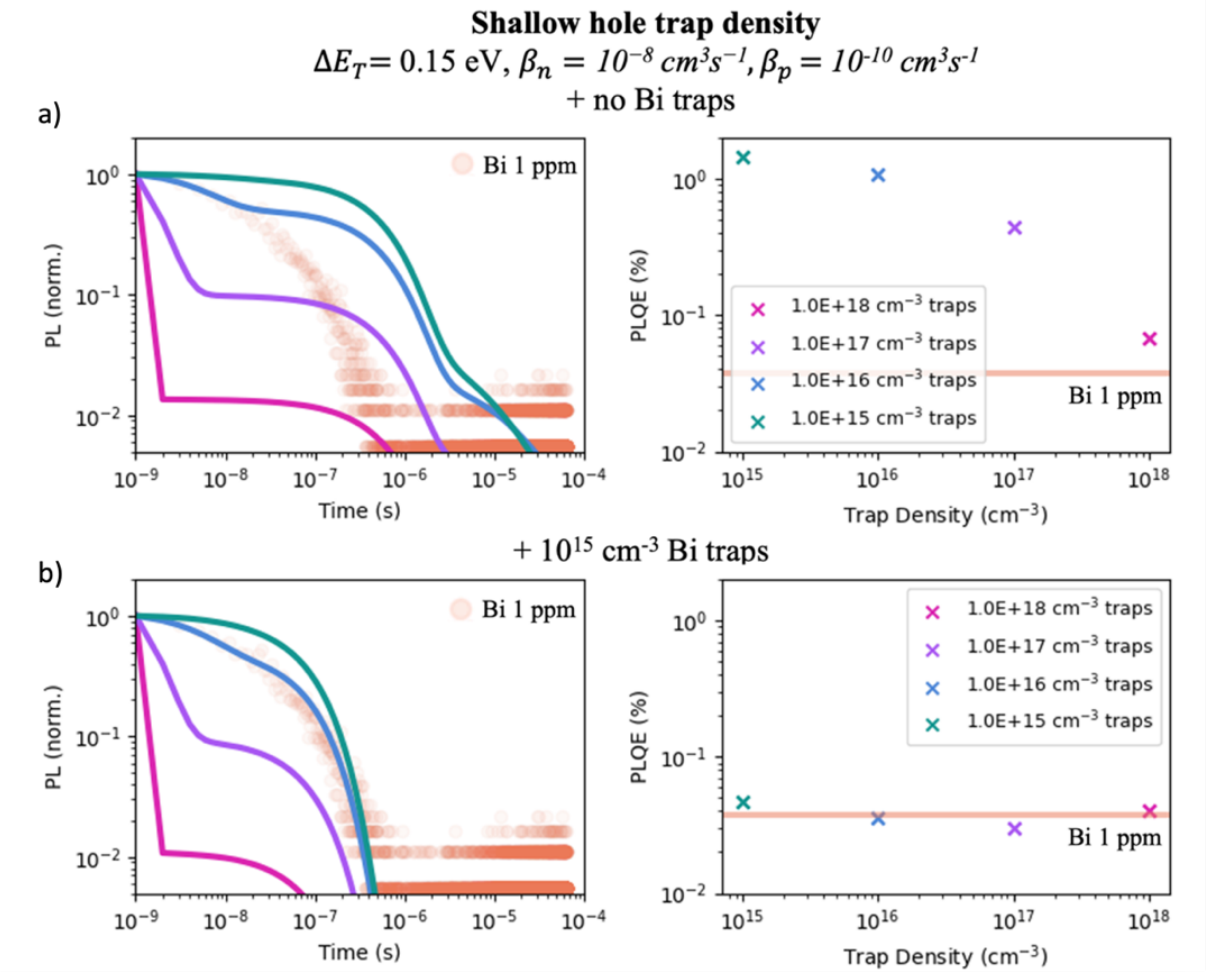


Figure 5.11. TRPL and PLQE as a function of shallow hole trap such as $V_{Pb/Sn}^{2-}$ or I_I^- variation (0.15 eV from CB, asymmetrical hole and electron capture coefficients of 10^{-8}, 10^{-10} cm^3s^{-1} respectively), a) without additional Bi traps and b) with 10^{15} cm^{-3} additional Bi traps. All additional simulation parameters are given in the methods.

This evidence, together with the small barrier to recombination predicted by DFT, suggest that the increased non-radiative recombination in of Bi- and Sb-doped films is mainly due to the direct trapping-recombination on the dopant sites. Encouragingly, this indicates that n-doping Sn-containing perovskites is not always doomed to increase non-radiative recombination, as the compensatory acceptor defects formed seem only minimally recombination-active.

5.4 Bi^{3+} impurities in perovskite precursor chemicals

The deleterious effect of very small amounts of Bi^{3+} doping (1 ppm) on the optoelectronic properties of lead-tin perovskites raises concerns about the potential presence of Bi^{3+} as an impurity in perovskite precursor chemicals. Even very high purity precursors normally only quote purity to 15 ppm and could thus have impurities on this scale (0.0001%). A range of lead-tin perovskite precursor powders were tested for Bi and Sb impurities by ICP-MS, which was able to detect these elements to a sensitivity of 0.01 ppm. The type, supplier, and purity of each precursor investigated is listed in Table 5.3, and the absolute Bi and Sb impurity densities determined by ICP-MS are presented in Table 5.4. These are representative of impurity concentrations that can be present under the typical operating conditions of a metal halide perovskite-producing laboratory, under which cross-contamination cannot be fully excluded. Even with strict fabrication procedures and cleanliness protocols, contamination may occur while precursor chemicals are stored in a glovebox area where Bi and Sb are also stored and occasionally handled. In addition, it should be emphasized that at such low impurity concentrations, batch-to-batch variation is likely and hence this data is not necessarily representative of other batches of a certain material or supplier.

Table 5.3. Descriptions of commercially available perovskite precursor chemicals tested by ICP-MS. It should be noted that samples were taken from containers which had been in use for some time, in a glovebox area where salts of Bi and Sb were also occasionally handled. Hence this data is not necessarily representative of a certain batch or supplier of material.

Chemical	**Description & purity, if provided**	**Supplier**
FAI	>99.99%	Greatcellsolar
CsI	99.9%	Alfa Aesar

PbI_2	Beads, ultra dry, 99.999% (metals basis)	Thermo Fisher Scientific
SnI_2 A	Beads, ultra dry, 99.999% (metals basis)	Thermo Fisher Scientific
SnI_2 B	Powder, for perovskite precursor, >97.0%	TCI
SnF_2	99.9%	Sigma Aldrich
Sn(0)	99.5%	Sigma Aldrich

*Table 5.4. Bi and Sb impurity concentrations in perovskite precursor chemicals, determined by ICP-MS. * signifies a minimum amount, as some solids remained after sample digestion which were deemed insoluble in nitric acid.*

	Contaminant concentration (ppm)	
	Sb (mean ± stdev)	Bi (mean ± stdev)
FAI	0.580 ± *0.225*	0.057 ± *0.059*
CsI	0.356 ± *0.057*	0.027 ± *0.017*
PbI_2	0.025 ± *0.002*	0.026 ± *0.005*
SnI_2 (A)	0.204* ± *0.008*	not detected (<0.01)
SnI_2 (B)	0.298* ± *0.002*	1.059* ± *0.012*
SnF_2	1.816* ± *0.047*	1.613* ± *0.065*
Sn(0)	0.476* ± *0.010*	0.198* ± *0.002*

The concentration of Bi which each precursor chemical would deliver to the perovskite ink (a 1.8M dispersion of $FA_{0.83}Cs_{0.17}Pb_{0.5}Sn_{0.5}I_3$ with 10% SnF_2 and 10 mg ml^{-1} Sn^0) is shown in Figure 5.12a. No precursors contributed significant levels of Sb (> 10 ppm),

but one precursor contributed possibly significant levels of Bi (> 0.1 ppm) to the solution. This was the SnI_2 precursor labelled 'B', at 0.5 ppm. However, perovskite films fabricated with this SnI_2 were compared to films fabricated with an alternate SnI_2 precursor containing no detected Bi (labelled 'A'), no significant difference in PLQE was observed (Figure 5.12b).

One possible explanation for this is that the Bi impurity could be present in its metallic neutral state within the precursor, since ICP-MS cannot determine in which oxidation state a trace impurity exists. Sn is more readily oxidized than Bi, so it is feasible that Bi impurities remain in their neutral state during the synthesis of SnI_2. Bi^0 is not expected to become dissolved in the perovskite ink, as neither Pb^{2+} nor Sn^{2+} are expected to be able to oxidize it, and as such the presence of Bi^0 impurities in perovskite precursor chemicals is not expected to lead to Bi^{3+} doping of the perovskite.

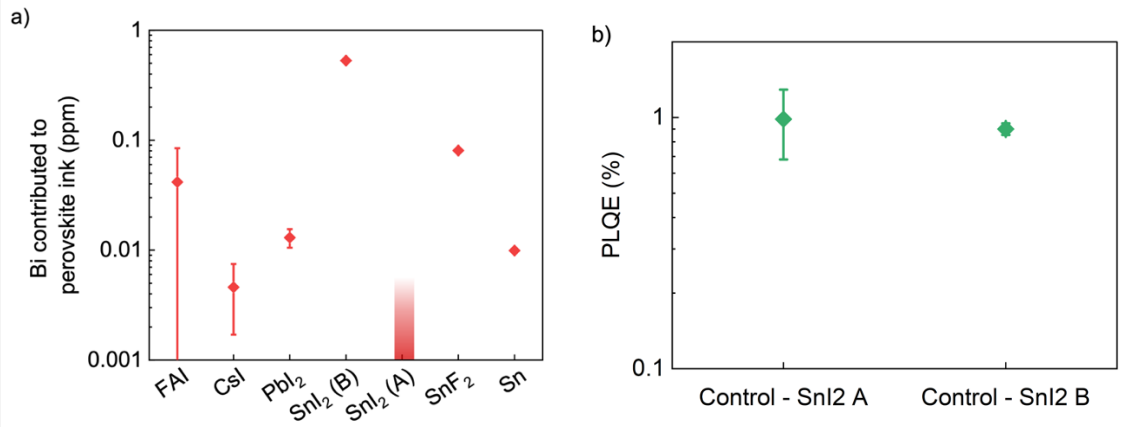


Figure 5.12. a) Bi density contributed to $FA_{0.83}Cs_{0.17}Pb_{0.5}Sn_{0.5}I_3$ perovskite precursor ink by commercial precursor chemicals, as determined by ICP-MS. B PLQE of lead-tin perovskite films fabricated either with SnI_2 from supplier A, which was determined by ICP-MS to contain <0.01 ppm Bi, or with SnI_2 from supplier B, which was determined by ICP-MS to contain 1 ppm Bi.

Although not demonstrated to be significant in this case, Bi^{3+} impurities could certainly present a problem for the field of perovskite photovoltaics in general, particularly

when large quantities of precursors are needed for scaling up. A facile solution for removing Bi^{3+} impurities could hence be achieved by treating the perovskite ink with a small amount of Sn^0 metal powder before filtering. Both Sn and Pb are more readily oxidized than Bi, which means that the following reaction is expected to take place between Sn^0 and Bi^{3+} (Equation 5.1).

$$3Sn^0_{(s)} + 2Bi^{3+}_{(sol)} \Rightarrow 2Bi^0_{(s)} + 3Sn^{2+}_{(sol)} \quad (5.1)$$

Bi^0 is subsequently expected to precipitate out of the solution and would be filtered out along with excess Sn^0. To test this approach, a precursor ink doped with a large amount of Bi^{3+} (100 ppm) was prepared, which would ordinarily result in films with very low PLQE. 10 mg/ml Sn^0 powder were subsequently added to the solution and stirred for 1 hour (Figure 5.13a). During the first ~20 minutes, the orange color slowly disappeared until the original yellow color of the precursor ink was restored. This precursor ink was then filtered and used to fabricate perovskite films. The PLQE (Figure 5.13b) of these films was comparable to undoped perovskite films. This confirms that the addition of Sn^0 powder removes Bi^{3+} impurities from perovskite precursor inks. For neat Pb perovskites, in theory Pb^0 powder can be added to achieve the same effect.

Overall, it is shown that although Bi impurities can be present in perovskite precursors at significant concentrations, these can be easily removed by reduction of Bi^{3+} in the precursor solution. Metallic Sn^0 is already a popular additive to tin-based perovskite inks, where it is said to reduce Sn^{4+} impurities in solution to Sn^{2+} via comproportionation, and thus improve device reproducibility and performance.[17] It may be the case that these improvements are also caused by the ability of metallic Sn^0 to purify precursor solutions from all metallic impurities which are less reactive than Sn.

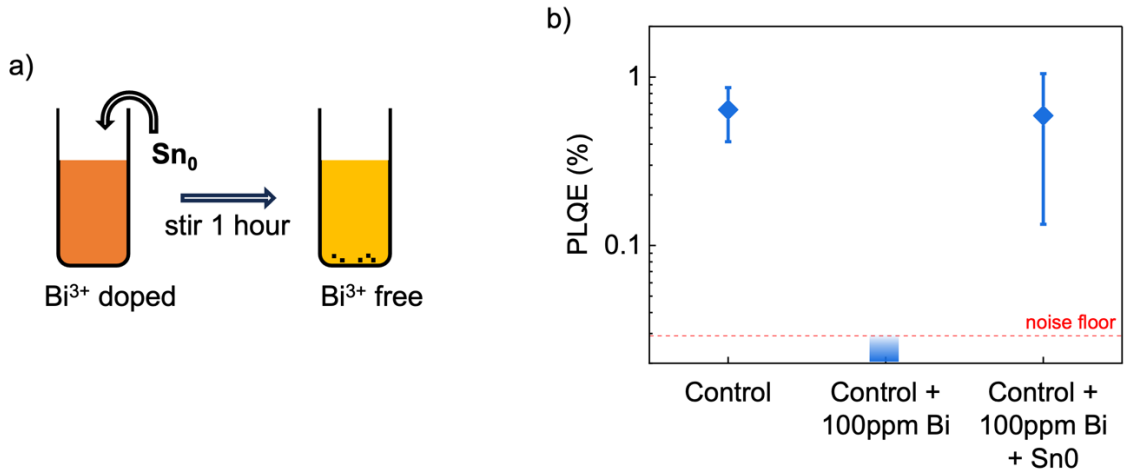


Figure 5.13. a) Schematic illustrating treatment of Bi^{3+}-containing perovskite precursor ink with Sn_0 powder to reduce and remove Bi^{3+}. b) PLQE of lead-tin perovskite films without any Bi^{3+} doping, doped with 100 ppm Bi^{3+}, and doped with 100 ppm Bi^{3+} and subsequently treated with Sn^0 for 1 hour, showing complete recovery of PLQE after Sn^0 treatment.

5.5 Conclusion & outlook on perovskite doping

In conclusion, the effect of Bi^{3+} and Sb^{3+} doping was investigated in lead-tin halide perovskites, and it was demonstrated that both dopants strongly increase the rate of non-radiative recombination within the perovskite. Through DFT simulations, it was shown that Bi^{3+} and Sb^{3+} can be stably incorporated in the perovskite lattice in the substitutional position to Pb^{2+}, where they directly induce deep electron trap states within the band gap of the material. Ultimately, the strong charge trapping activity of Bi^{3+} and Sb^{3+} makes them unsuitable for use as n-dopants in lead-tin perovskites.

Experiments showed that while lead-tin perovskites are more tolerant towards the presence of Sb^{3+} in the perovskite precursor, they are extremely sensitive to the incorporation of Bi^{3+}, showing quenched photoluminescence at concentrations as low as 1 ppm. Some precursors contribute bismuth concentrations approaching 0.5 ppm to the perovskite precursor ink but reveal that the use of these precursors did not result in films with

significantly accelerated non-radiative recombination, possibly due to Bi impurities existing in their metallic rather than ionic form. However, these Bi^{3+} impurities can be easily removed from perovskite precursors by stirring with metallic Sn^0 powder. Using this method, the successful removal of 100 ppm Bi from the perovskite precursor such that the electronic quality of the resulting film is equal to that of undoped films was demonstrated.

5.6 Works cited

1. Pena-Camargo, F. *et al.* Revealing the doping density in perovskite solar cells and its impact on device performance. *Applied Physics Reviews* (2022).
2. Milot, R. L. *et al.* Radiative Monomolecular Recombination Boosts Amplified Spontaneous Emission in $HC(NH_2)_2SnI_3$ Perovskite Films. *J. Phys. Chem. Lett.* **7**, 4178–4184 (2016).
3. Mosconi, E., Merabet, B., Meggiolaro, D., Zaoui, A. & De Angelis, F. First-Principles Modeling of Bismuth Doping in the $MAPbI_3$ Perovskite. *J. Phys. Chem. C* **122**, 14107–14112 (2018).
4. Lyons, J. L. Effective Donor Dopants for Lead Halide Perovskites. *Chem. Mater.* **33**, 6200–6205 (2021).
5. Yavari, M. *et al.* How far does the defect tolerance of lead-halide perovskites range? The example of Bi impurities introducing efficient recombination centers. *J. Mater. Chem. A* **7**, 23838–23853 (2019).
6. Ulatowski, A. M. *et al.* Charge-Carrier Trapping Dynamics in Bismuth-Doped Thin Films of $MAPbBr_3$ Perovskite. *J. Phys. Chem. Lett.* **11**, 3681–3688 (2020).
7. Nayak, P. K. *et al.* Impact of Bi^{3+} Heterovalent Doping in Organic–Inorganic Metal Halide Perovskite Crystals. *J. Am. Chem. Soc.* **140**, 574–577 (2018).
8. Meng, R. *et al.* Understanding the Impact of Bismuth Heterovalent Doping on the Structural and Photophysical Properties of $CH_3NH_3PbBr_3$ Halide Perovskite Crystals with Near-IR Photoluminescence. *Chemistry A European J* **25**, 5480–5488 (2019).
9. Gregori, L., Meggiolaro, D. & De Angelis, F. Combining Trivalent Ion-Doping with Halide Alloying to Increase the Efficiency of Tin Perovskites. *Small* 2403413 (2024).
10. Palmer, J. R. *et al.* Bismuth in Lead–Tin Alloy Perovskites: Effect on Material Properties and Photovoltaic Device Performance. *ACS Appl. Energy Mater.* **7**, 2726–2734 (2024).
11. Huang, L. *et al.* Schottky/p-n Cascade Heterojunction Constructed by Intentional n-Type Doping Perovskite Toward Efficient Electron Layer-Free Perovskite Solar Cells. *Solar RRL* **3**, 1800274 (2019).
12. Zeiske, S., Kaiser, C., Meredith, P. & Armin, A. Sensitivity of Sub-Bandgap External Quantum Efficiency Measurements of Solar Cells under Electrical and Light Bias. *ACS Photonics* **7**, 256–264 (2020).

13. Perdew, J. P., Ernzerhof, M. & Burke, K. Rationale for mixing exact exchange with density functional approximations. *The Journal of Chemical Physics* **105**, 9982–9985 (1996).
14. Adamo, C. & Barone, V. Toward reliable density functional methods without adjustable parameters: The PBE0 model. *The Journal of Chemical Physics* **110**, 6158–6170 (1999).
15. Zhang, X., Shen, J.-X., Turiansky, M. E. & Van De Walle, C. G. Hidden role of Bi incorporation in nonradiative recombination in methylammonium lead iodide. *J. Mater. Chem. A* **8**, 12964–12967 (2020).
16. Meggiolaro, D., Ricciarelli, D., Alasmari, A. A., Alasmary, F. A. S. & De Angelis, F. Tin versus Lead Redox Chemistry Modulates Charge Trapping and Self-Doping in Tin/Lead Iodide Perovskites. *J. Phys. Chem. Lett.* **11**, 3546–3556 (2020).
17. Lin, R. *et al.* Monolithic all-perovskite tandem solar cells with 24.8% efficiency exploiting comproportionation to suppress Sn(ii) oxidation in precursor ink. *Nat Energy* **4**, 864–873 (2019).

6 Modelling recombination in lead-tin perovskites

6.1 Overview

The ability of organic-inorganic hybrid perovskite materials to attain long charge carrier lifetimes even with low-cost processing techniques has been central to its rapid development in PV devices.[1] Often, record-breaking PSCs are enabled by a novel additive or deposition strategy which is reported to reduce defect densities in the perovskite bulk or at its interfaces.[2–4] It is hence essential for researchers to be able to accurately quantify the effects of perovskite additives or material stressing on defect densities in perovskites. A wide range of characterization techniques has been employed to investigate recombination dynamics in MHP materials. Popular examples include TRPL,[5] PLQE,[6] TPC,[7] transient absorption (TAS),[8] and time-resolved microwave conductivity (TRMC).[9] The goal of such measurements is normally to quantify rates of non-radiative recombination in the perovskite material. It is even more desirable to estimate various recombination coefficients and defect densities directly from these measurements.

However, these characterization methods can only quantify recombination indirectly, as they rely on a pre-determined model of recombination to interpret measurements. As a result, the accuracy of the extracted material parameters strongly depends on the correctness of the model selected for interpretation. Formulating a recombination model always requires some simplification of the actual physical processes expected to take place. This may present special challenges in perovskites due to their degree of inhomogeneity and uncertainty about dominant recombination processes. The recombination dynamics in hybrid halide perovskites are not yet fully understood,[10] and may differ significantly per perovskite composition, phase and quality. For example, there is not yet a consensus in the field over which model should be used to interpret the commonly used TRPL measurements.[11,12,13,14]

Whilst methods to directly quantify defect densities and energy levels exist,[15] they are less accessible to the majority of research groups and may still require some degree of modelling to extract the most relevant material parameters. Hence, deeper investigation into the most relevant recombination modes in perovskites is of great relevance to the field, especially for less studied perovskite compositions. In this chapter, PLQE and TRPL data of lead-tin MHP are presented, and simulations are used to illustrate how various recombination mechanisms can affect the output TRPL and PLQE data. Based on these simulations, two competing models for charge carrier recombination in a lead-tin MHP material are formulated, on which I perform Bayesian inference and use the results to calculate Bayes factors[16] for the competing models. This method can be used to quantitatively select a 'best' model for the extraction of relevant recombination parameters. In this case, the proof-of-concept shows that a two-trap model is more appropriate than a one-trap model in describing the combined TRPL and PLQE dataset used here. The use of this revised model for recombination in lead-tin perovskites is then demonstrated to extract relevant parameters from data.

6.2 Current state of PL measurement interpretation

This chapter focuses on the interpretation of TRPL and PLQE data (Figure 6.1a), selected because they are very commonly used in the perovskite research community. Additionally, the lack of electrical contacting involved in these characterization methods avoids the need to take into account capacitive processes at metal contacts, simplifying the model (unlike in transient photovoltage measurements,[17,18] for example).

TRPL decays reflect the change in the radiative recombination rate (a function of free carrier density) in the material over time after pulsed excitation, whilst PLQE calculates the rate of radiative to total recombination. A sample TRPL and PLQE dataset of an encapsulated

$MA_{0.3}FA_{0.6}Cs_{0.1}Pb_{0.5}Sn_{0.3}I_3$ film on glass is presented in Figure 6.1b and c. Both of these measurements were performed at a range of excitation densities to enable further insight into the recombination dynamics, as different recombination mechanisms are expected dominate at different carrier densities. PLQE measurements were repeated three weeks after sample fabrication, and minimal difference in the measured PLQE values was found. Hence, no sample degradation is expected to have occurred during measurement. To calculate the expected rate of carrier generation per pulse or per second (shown on the x-axis in Figure 6.1b and c), the 900 nm thick films were assumed to absorb all incident light which was not reflected (88% of incident photons, determined from reflectance measurements).

Lead-tin perovskites are expected to be slightly p-type, with reported background hole densities in the range $10^{14} – 10^{17}$ cm^{-3}.[19,20,21] To investigate whether recombination in the lead-tin perovskite films at the excitation densities measured here is mainly occurring in the high injection ($\Delta n/p > p_0$) or low injection ($\Delta n/p < p_0$) regime, the PL count intensity at the beginning (maximum) of the measured TRPL decay was measured at a range of excitation fluences (Figure 6.1d). Assuming that that no recombination has taken place at this time, the dependence of this signal intensity on excitation fluence reflects how the rate of radiative band-to-band recombination producing this signal scales with carrier density. In a high injection regime, $\Delta n > p_0$ and $R_{rad} = k_{rad}\Delta n^2$, whilst in the low injection regime, $\Delta n < p_0$ and $R_{rad} = k_{rad}p_0\Delta n$.

In this case, Figure 6.1d shows that the rate of radiative emission scales quadratically with excitation fluence, indicating that recombination is taking place in the high injection regime. From this, the density of background holes can be estimated to lie below the lowest density of photoexcited carriers probed, ~10^{13} cm^{-3} (E_F ~0.3 eV from VB). Whilst this indicates that the background hole density in these lead-tin perovskite films does not affect recombination dynamics at very early times in these transient measurements, it does not

guarantee that they don't affect the rest of the data. It is feasible for photoexcited carrier densities to fall below 10^{13} cm^{-3} during later times in the TRPL measurement, or in the lower excitation density steady-state PLQE measurements. Such potential impacts are further explored by simulation in section 6.3.

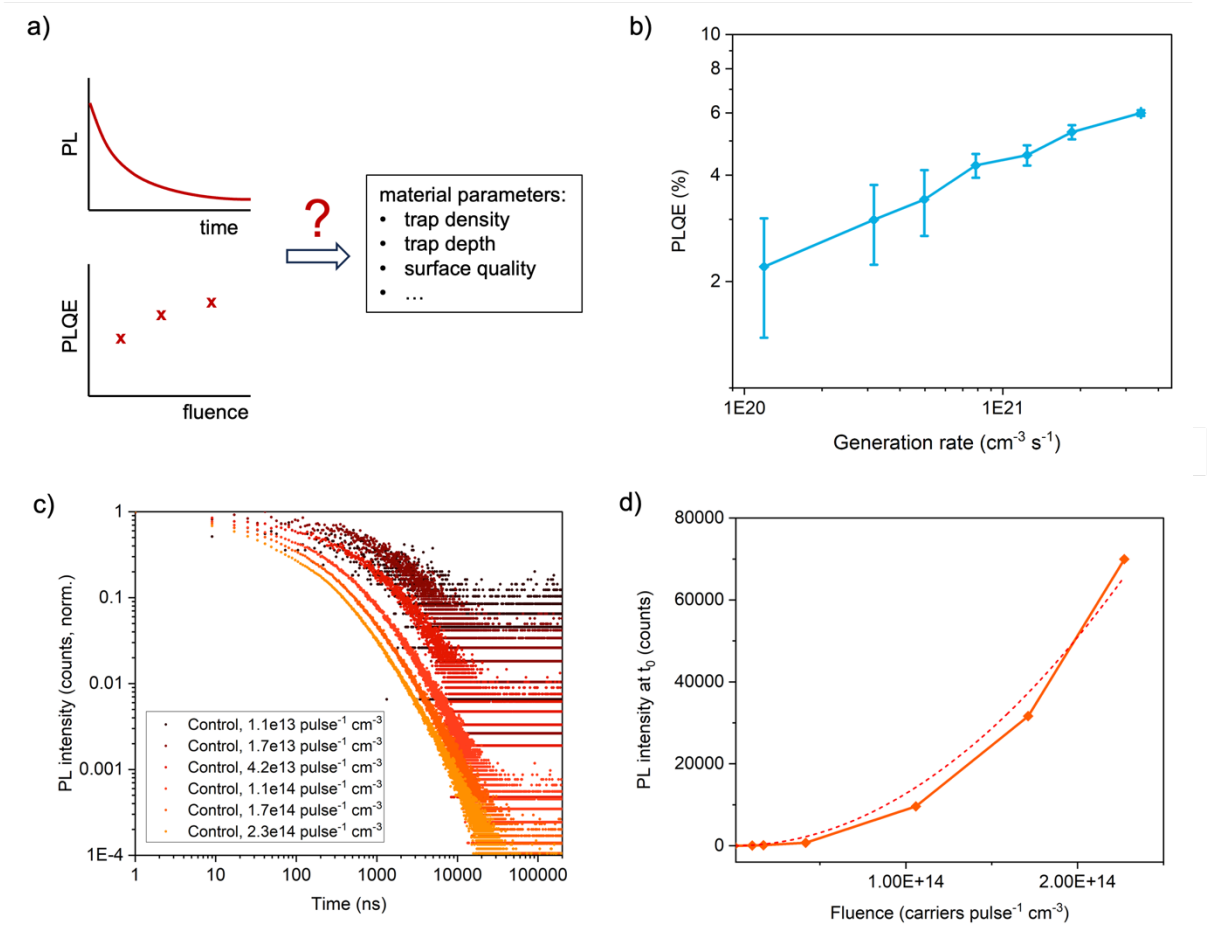


Figure 6.1. a) Schematic representing desired information to be extracted from TRPL and PLQE measurements. b) Intensity-dependent PLQE and b) TRPL after 4 kHz pulsed excitation of encapsulated $MA_{0.3}FA_{0.6}Cs_{0.1}Pb_{0.5}Sn_{0.5}I_3$ films deposited on glass. d) PL intensity immediately after pulsed excitation (time resolution: 4ns) as a function of 4 kHz pulsed excitation density. A quadratic fit is overlaid (red dotted line).

The simplest analysis of TRPL decay measurement often performed is the extraction of a recombination lifetime by fitting to the monoexponential decay $e^{-t/\tau}$. Such analysis assumes that the recombination dynamics are dominated by a single trap-assisted

recombination process ($dn/dt = G - n/\tau$), for which detrapping is negligible (because electron and hole capture rates are very similar, or because the trap energy lies towards the middle of the bandgap).[11] A stretched monoexponential decay is sometimes used to represent the same recombination process, but assuming a distribution of lifetimes (due to a distribution of recombination processes, trap states, or spatial inhomogeneity of the perovskite material).[12]

Recent work has shown that this model describes the shape of high-quality TRPL decays (counts signal collected over 3+ orders of magnitude) quite poorly, suggesting that an alternative model is needed.[11] This is true for the TRPL data measured here also. Calculation of the 'differential lifetime', proportional to $\left(\frac{dln(PL)}{dt}\right)^{-1}$, reveals the recombination lifetime that would be extracted from fitting the TRPL transient to a monoexponential decay at each point in time (Figure 6.2a). A decay dominated by a single trap-assisted recombination process should result in a differential lifetime that does not vary over time or with excitation fluence.[22] However, instead an initial fluence-dependent variation is observed, after which the lifetime continuously increases. Based on range of recombination lifetimes observed in the TRPL data (τ = 10^{-7} – 10^{-5} s), expected PLQE values are simulated at a range of excitation densities, which are presented in Figure 6.2b. The simulations clearly show that the lifetimes can account for a vast range of PLQE values. Furthermore, none of them can reproduce the dependence of PLQE on generation rate observed in the experimental data. This conclusively shows that a more complex model is needed to explain and extract parameters from the measured TRPL and PLQE data.

This continuous variation in differential lifetime of TRPL decays was also observed by Yuan et al., and was ascribed by them to the slow de-trapping of carriers from shallow defects.[11] Whilst this is likely an important factor to include when modelling recombination, many other mechanisms may affect recombination dynamics also. These were explored in section 2.4, but in brief include higher-order Auger and radiative recombination, the

aforementioned background hole density in lead-tin perovskites, and inhomogeneous carrier and trap density distribution in the cross-sectional direction. In the next section, their potential impact on TRPL and PLQE measurements is quantified by simulation.

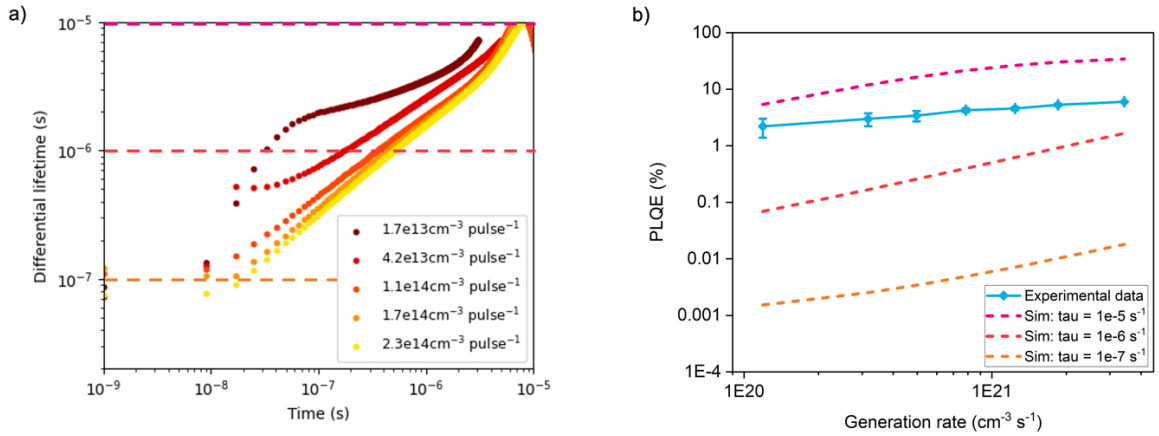


Figure 6.2. a) Differential lifetimes calculated from the decays in Figure 6.1c. The differential lifetime for the lowest fluence of 1.7 x 10^{13} cm^{-3} $pulse^{-1}$ could not be reliably determined due to excessive noise on the data. b) PLQE values simulated for radiative ($k_{rad,int}$ = 10^{-10} cm^3 s^{-1}), Auger (k_{aug} = 10^{-28} cm^6 s^{-1}), and single deep trap-assisted recombination (R_{SRH} = $-n/\tau$, τ = 10^{-7} – 10^{-5} s). Simulated data (dotted lines) is overlaid on the experimental data (solid line) from Figure 6.1b.

6.3 PLQE & TRPL simulations

To assess which recombination mechanisms most strongly affect TRPL and PLQE measurements, the impact of the variation of various recombination parameters on transients and steady-state measurements was simulated. An intermediate excitation fluence of 10^{14} absorbed carriers cm^{-3} $pulse^{-1}$ was used for TRPL simulations.

The impacts of variation in E_F, Auger recombination coefficient (k_{aug}), and radiative recombination coefficient ($k_{rad,\ int}$) on TRPL and PLQE in the presence of some trap-assisted recombination (10^{14} cm^{-3} deep electron traps) are presented in Figure 6.3. Within the range of excitation densities used here for TRPL and PLQE measurements, E_F only begins to affect measurements when it lies less than 0.2 eV away from the VB. Moving the E_F closer to the

VB, which causes a further increase in background hole density, initially flattens the dependence of PLQE on excitation density. This occurs because the rate of radiative recombination begins to increase and becomes monomolecular due to the switch to a low injection regime. A very high background hole density (E_F very close to the VB) begins to decrease PLQE across all fluences. Simulations furthermore demonstrate that variation of both k_{aug} and $k_{rad,int}$ have a negligible effect on TRPL decays, but $k_{rad,int}$ strongly affects the magnitude of PLQE.

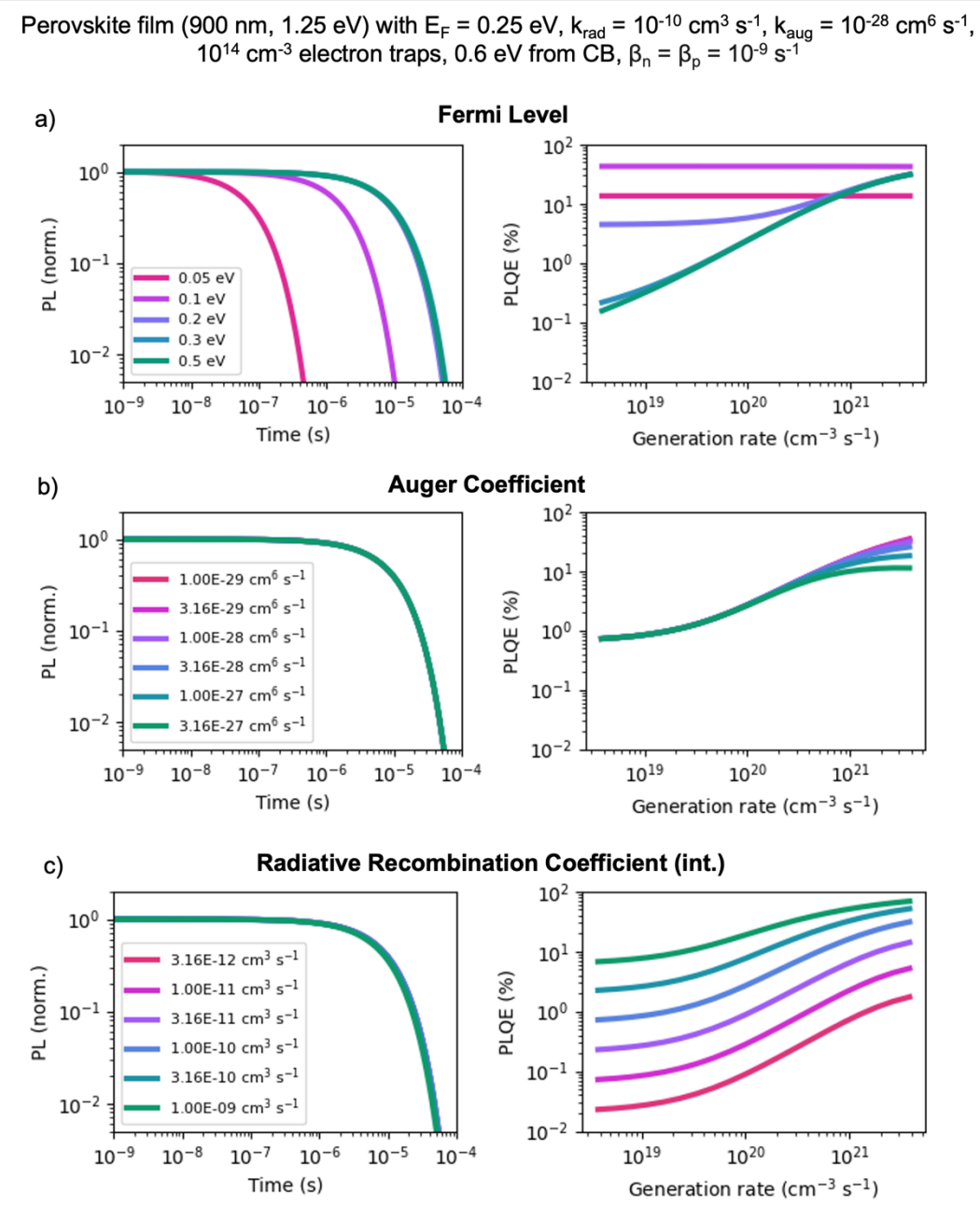


Figure 6.3. Simulations of TRPL decays produced by 4 kHz pulsed excitation generating 10^{14} carriers cm^{-3} pulse^{-1}, and PLQE values at continuous excitation generating 4 x 10^{18} – 4 x 10^{21} carriers cm^{-3} s^{-1}, upon variation of the a) Fermi level E_F, b) Auger recombination coefficient for nnp and ppn (k_{aug}), and c) internal radiative recombination coefficient ($k_{rad,\ int}$).

Next, the effect of various trapping parameters on TRPL and PLQE was investigated. Within the Shockley-Read-Hall model, trapping and de-trapping rates of holes and electrons can be fully described by the free charge carrier densities, trap density N_T, electron and hole capture coefficients β_n and β_p, and the trap depth E_T. Figure 6.4 shows the effects of these

parameters on TRPL and PLQE by comparing deep (0.6 eV from CB) and shallow (0.05 eV from CB) traps with different capture coefficients.

Classical statistical models of multi-phonon trapping predicts that traps with an energy level E_T further away from the CB/VB have an smaller electron/hole capture coefficient, which decreases approximately exponentially.[23] A full quantitative prediction of the relationship between trap depth and capture coefficients using this model has been made for $MAPbI_3$ by Das et al.[24] This relationship has led to the commonly held assumption that deep traps are always recombination-active, as they are able to efficiently capture both electrons and holes. Recent first-principles simulations have indicated that this relationship between trap energy and capture coefficients does not hold for halide perovskites. In these relatively soft materials, there are often pronounced differences in the lattice relaxation and in the vibrational frequencies associated with the empty and filled trap state. These factors cause a large difference in configuration coordinate (ΔQ) and/or significant anharmonicity of the potential energy surface.[1] Consequently, the value of electron and hole capture coefficients in halide perovskites cannot be predicted by the trapping energy.

Figure 6.4 demonstrates two important differences between the effect of deep and shallow traps on TRPL and PLQE (a,c compared to b,d). First, shallow traps have a much smaller impact on the acceleration of the TRPL signal decay, although very high densities cause the appearance of a rapid (few ns) trap-filling component. Second, shallow traps cause flattening of the dependence of PLQE on excitation density. However, simulations also reveal that a shallow electron trap can replicate the behaviour of a deep electron trap if it has a significantly increased hole capture coefficient (Figure 6.4f). This balances the net electron and hole trapping rates, resulting in a trap that is more strongly recombination-active. Finally, Figure 6.4e shows that when one of the capture coefficients is much smaller than the other, a ‘bump’ appears in the TRPL decay which can be attributed to de-trapping at later times.

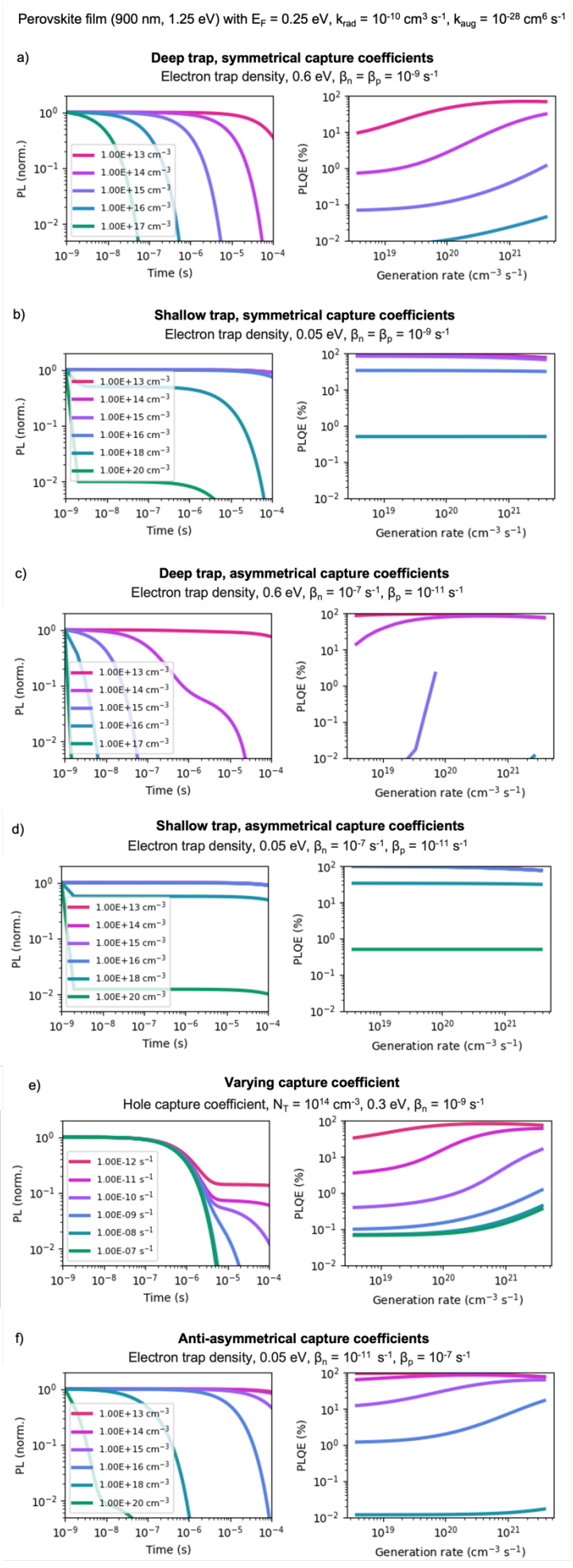

Perovskite film (900 nm, 1.25 eV) with E_F = 0.25 eV, k_{rad} = 10^{-10} cm^3 s^{-1}, k_{aug} = 10^{-28} cm^6 s^{-1}
a)
Deep trap, symmetrical capture coefficients
Electron trap density, 0.6 eV, β_n = β_p = 10^{-9} s^{-1}
b)
Shallow trap, symmetrical capture coefficients
Electron trap density, 0.05 eV, β_n = β_p = 10^{-9} s^{-1}
c)
Deep trap, asymmetrical capture coefficients
Electron trap density, 0.6 eV, β_n = 10^{-7} s^{-1}, β_p = 10^{-11} s^{-1}
d)
Shallow trap, asymmetrical capture coefficients
Electron trap density, 0.05 eV, β_n = 10^{-7} s^{-1}, β_p = 10^{-11} s^{-1}
e)
Varying capture coefficient
Hole capture coefficient, N_T = 10^{14} cm^{-3}, 0.3 eV, β_n = 10^{-9} s^{-1}
f)
Anti-asymmetrical capture coefficients
Electron trap density, 0.05 eV, β_n = 10^{-11} s^{-1}, β_p = 10^{-7} s^{-1}
PL (norm.)
Time (s)
PLQE (%)
Generation rate (cm^{-3} s^{-1})
1.00E+13 cm^{-3}
1.00E+14 cm^{-3}
1.00E+15 cm^{-3}
1.00E+16 cm^{-3}
1.00E+17 cm^{-3}
1.00E+18 cm^{-3}
1.00E+20 cm^{-3}
1.00E-12 s^{-1}
1.00E-11 s^{-1}
1.00E-10 s^{-1}
1.00E-09 s^{-1}
1.00E-08 s^{-1}
1.00E-07 s^{-1}

Figure 6.4. Simulations of TRPL decays produced by 4 kHz pulsed excitation generating 10^{14} carriers cm^{-3} $pulse^{-1}$, and PLQE values at continuous excitation generating 4 x 10^{18} – 4 x 10^{21} carriers cm^{-3} s^{-1}, upon variation of trap density for a) a deep trap with $\beta_n = \beta_p$, b) a shallow trap with $\beta_n = \beta_p$, c) a deep trap with $\beta_n >> \beta_p$, d) a shallow trap with $\beta_n >> \beta_p$, d) variation in β_p, and f) a shallow trap with $\beta_n << \beta_p$.

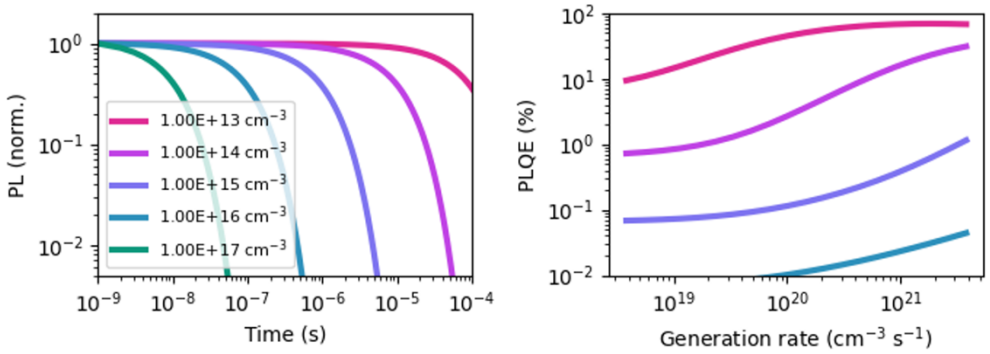
Next, the impact of electron and hole traps were compared for a slightly p-type perovskite (E_F = 0.25 eV). Figure 6.5 shows that the non-intrinsic nature of the material causes only a small difference in the recombination activity of an electron trap compared to a hole trap, although this may be more pronounced for a more strongly doped material.

Perovskite film (900 nm, 1.25 eV) with E_F = 0.25 eV, k_{rad} = 10^{-10} cm^3 s^{-1}, k_{aug} = 10^{-28} cm^6 s^{-1}

a)

Deep electron trap

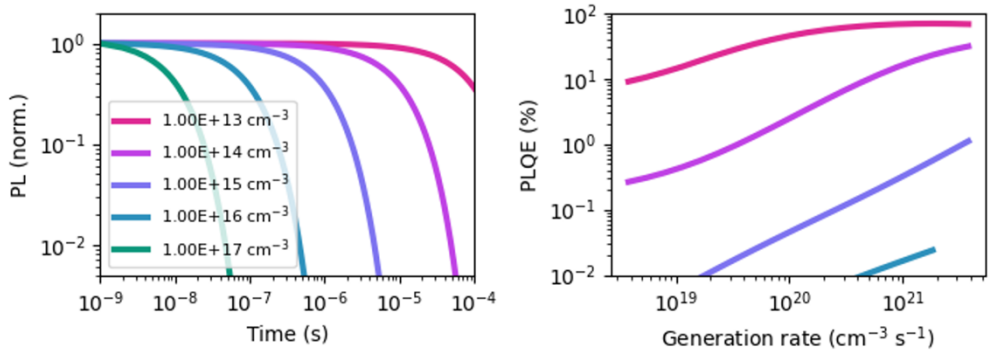
Electron trap density, 0.6 eV, $\beta_n = \beta_p = 10^{-9}$ s^{-1}



b)

Deep hole trap

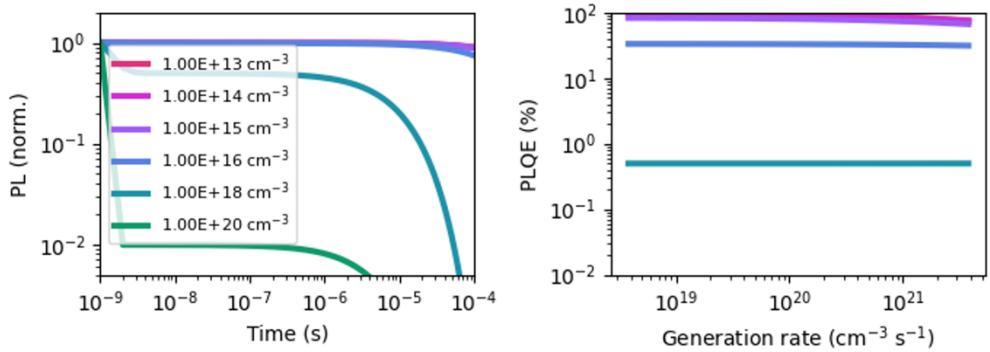
Hole trap density, 0.05 eV, $\beta_n = \beta_p = 10^{-9}$ s^{-1}



c)

Shallow electron trap

Electron trap density, 0.05 eV , $\beta_n = \beta_p = 10^{-9}$ s^{-1}



d)

Shallow hole trap

Hole trap density, 0.05 eV eV, $\beta_n = \beta_p = 10^{-9}$ s^{-1}

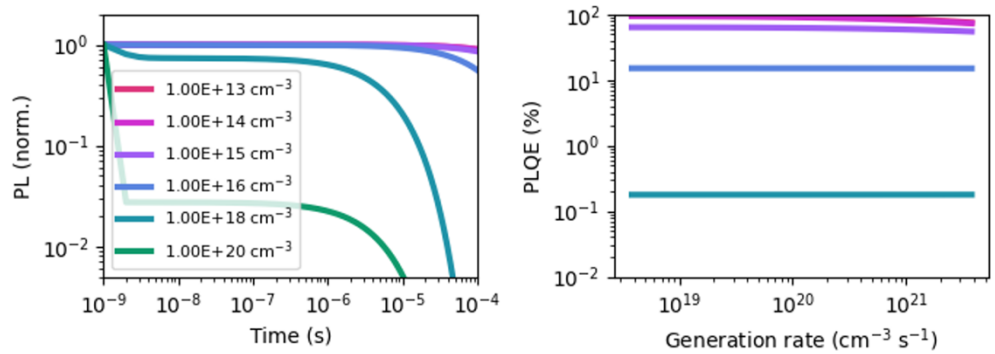


Figure 6.5. Simulations of TRPL decays produced by 4 kHz pulsed excitation generating 10^{14} carriers cm^{-3} $pulse^{-1}$, and PLQE values at continuous excitation generating 4 x 10^{18} – 4 x 10^{21} carriers cm^{-3} s^{-1}, upon variation of trap density for a) a deep electron trap, b) a deep hole trap, c) a shallow electron trap, and d) a shallow hole trap.

Finally, the inhomogeneous distribution of traps throughout the cross-section of the perovskite film was considered. As previously discussed in section 2.4, the density of traps is normally expected to be higher at the interfaces of the perovskite film. This is particularly plausible in lead-tin perovskites, where Sn^{2+} oxidation is expected to create Sn^{2+} vacancies/undercoordinated halide sites at the perovskite surface.[25,26] To model this, a separate trap density $N_{T,surface}$ was defined for the top segment of the film (with a thickness of ~45 nm, for the 20-segment simulation used here). Figure 6.6a shows the effect of this surface trap density on TRPL and PLQE for equal electron and hole mobilities of 1 cm^2 V^{-1} s^{-1}, demonstrating that a thin slice of more defective material can significantly accelerate non-radiative recombination. Figure 6.6b reveals that the impact of an increased surface trap density (10^{17} cm^{-3}) depends strongly on the electron and hole mobilities. If mobilities are very low, the impact of surface traps on TRPL is reduced as the speed of free charge carrier diffusion towards the surface is reduced.

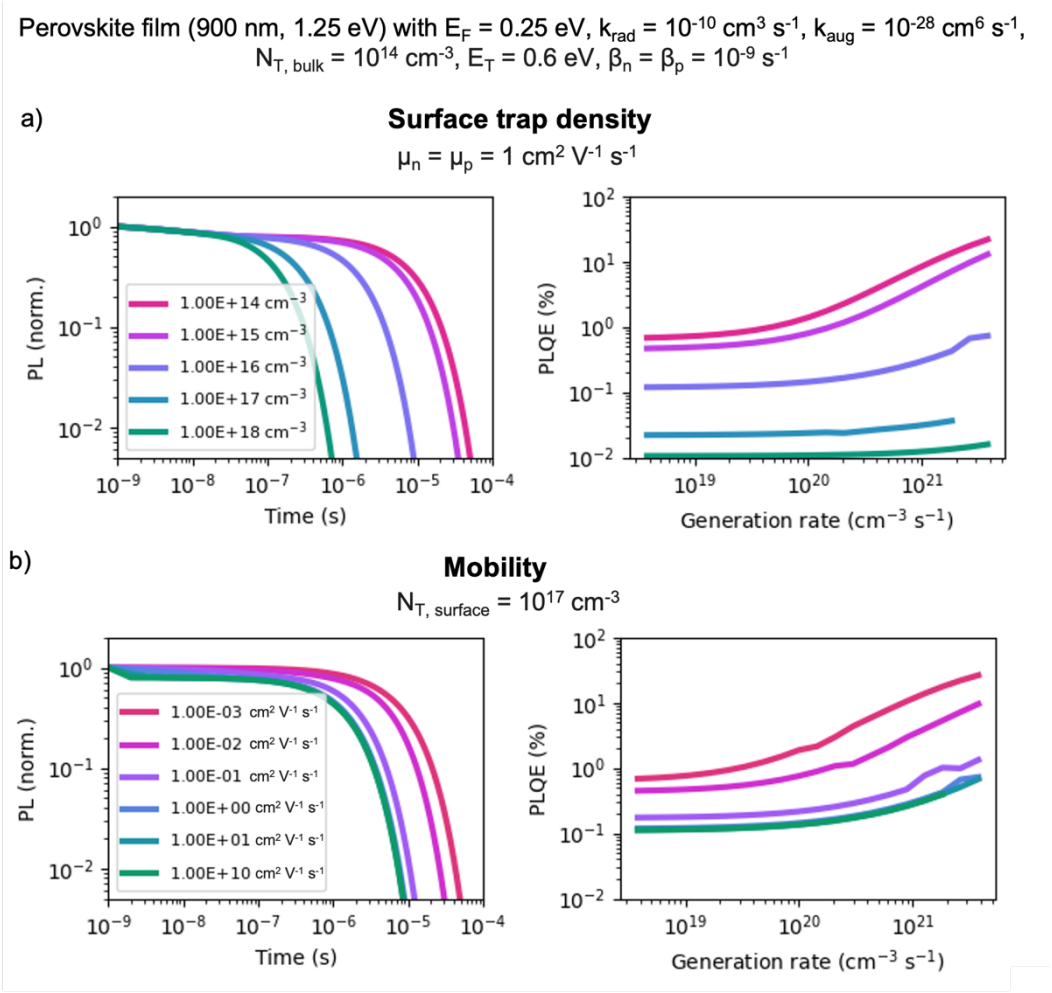


Figure 6.6. Simulations of TRPL decays produced by 4 kHz pulsed excitation generating 10^{14} carriers cm^{-3} pulse^{-1}, and PLQE values at continuous excitation generating 4 x 10^{18} – 4 x 10^{21} carriers cm^{-3} s^{-1}, upon variation of a) surface trap density and b) electron and hole mobility with a surface trap density of 10^{17} cm^{-3}, for samples illuminated from the substrate side (opposite to the surface).

The effect of the rate of pulsed excitation on the shape of the TRPL decay was also investigated. Considering the potential existence of shallow traps and asymmetric capture coefficients, it seems possible for the population of free and trapped charge carriers created by photoexcitation to not decay to its initial values during the duration between pulses. Such a mechanism was previously also modelled by others.[13,14] Investigating the effect of the rate of pulsed excitation on the shape of the TRPL decay (Figure 6.7) reveals a small difference between pulse rates of 1-1000 kHz. This difference is most pronounced in the first 10-100ns

of the decay. To account for this in a recombination model, the densities of free and trapped charge carriers obtained at the end of the calculated TRPL decay were compared to those at the beginning. If charge carrier densities were found to not decay to their original values at the end of the TRPL measurement window, the ODEs were solved again with the new initial carrier condition given by the carrier densities at the end of the decay.

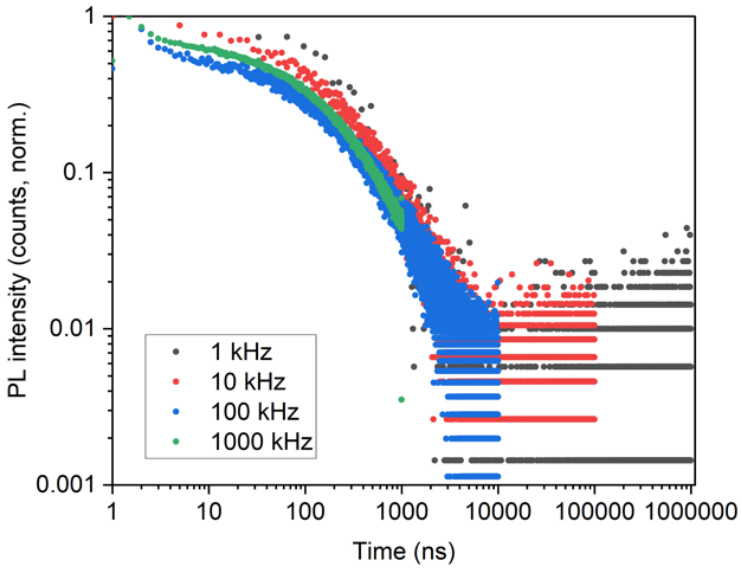


Figure 6.7. TRPL decays produced by pulsed excitation generating 2.3 x 10^{14} carriers cm^{-3} $pulse^{-1}$, at various pulse rates.

These simulations suggest that the radiative recombination coefficient trap (surface) density, trap depth, symmetry of capture coefficients, and mobility can all significantly affect TRPL and PLQE measurements at the excitation conditions used here. Due to the number of free parameters involved, it not possible to judge which of these recombination modes should be used to fit and extract parameters from the experimental data without quantitative model comparison. A model with more parameters may result in a better fit simply because it contains more degrees of freedom, not because it more accurately described the real physics of the system. Using some quantitative basis to compare models is hence essential to ensure that extracted parameter values are valid.

I next show how two different recombination models can be compared in how well they describe the measured TRPL & PLQE dataset. A wide range of possible recombination models can be compared using the same technique, but only two simple models were selected here as a proof-of-concept. Both models take into account Auger and radiative band-to-band recombination. However, Model 1 allows trap-assisted SRH recombination to occur via one trap (with free parameters of trap depth, density, and hole and electron capture coefficients), whilst Model 2 allows for this to occur via two different traps with different parameters (Table 6.1).

Table 6.1 Formulation of two different possible recombination models, outlining which recombination processes are allowed in each model. Full mathematical formulations of the charge carrier kinetics for each recombination process are detailed in section 3.5.

Model	Rate of change of free electron density	Parameters varied
1	$\frac{dn}{dt} = G - R_{aug} - R_{rad} - R_{trap1,bulk} - R_{trap1,surf}$	k_{rad}, μ_n, $N_{T1,bulk}$, $N_{T1,surface}$, E_{T1}, β_{n1}, β_{p1}
2	$\frac{dn}{dt} = G - R_{aug} - R_{rad} - R_{trap1,bulk} - R_{trap1,surf} - R_{trap2,bulk} - R_{trap2,surf}$	k_{rad}, μ_n, $N_{T1,bulk}$, $N_{T1,surface}$, E_{T1}, β_{n1}, β_{p1}, $N_{T2,bulk}$, $N_{T2,surface}$, E_{T2}, β_{n2}, β_{p2}

6.4 Bayesian Inference & Model Selection

The model used to extract material parameters from data strongly affects the results of the inference, so to substantiate extracted parameters, it is important to obtain evidence for the validity of the model. However, this cannot necessarily be inferred from the quality of the fit of the modelled to the experimental data. Models with a higher number of free parameters are in general more likely to produce a good fit to experimental data, because the flexibility

of the model can 'conceal' any potential physical incorrectness of the model. This is exemplified in the use of bi- and even tri-exponential decay models to produce 'good' fits to transient PL measurements of MHP films, despite lack of proven physical relevance.[12,27]

Here, to quantitatively assess which of the above recombination models best explains the available TRPL and PLQE data, Bayesian inference was performed on a joint TRPL and PLQE dataset using Nested Sampling.[28,29] The workflow is illustrated in Figure 6.8. This method enables the computation of the Bayes factor, providing a quantitative approach to selecting the most appropriate model.

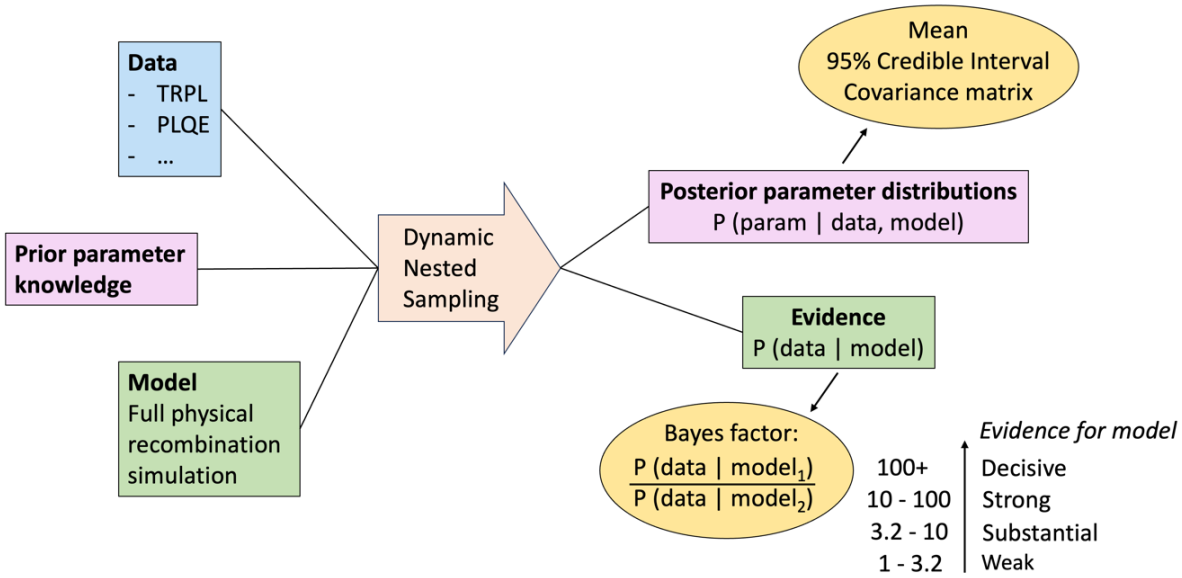


Figure 6.8. Nested Sampling workflow.

A joint TRPL and PLQE dataset was fit using Nested Sampling and the models in Table 6.2. The parameters varied are shown in Table 6.1, and the prior distributions provided for all free parameters are shown in Figure 6.10. The Auger recombination coefficient was set to be constant at 10^{-28} cm^6 s^{-1}, and E_F was set at 0.3 eV. The maximum likelihood, which represents one possible indicator of the goodness of fit, was 1.5 x 10^8 for model 1 (containing one type of trap) and 3.3 x 10^8 for model 2 (containing two different types of traps, one

electron and one hole trap). Whilst model 2 was hence found to have a slightly higher maximum likelihood/quality of fit than model 1, it also contains 5 more free parameters.

Table 6.2 Fitting results for each model.

	Model	**Max. Likelihood**	**Evidence**
1	1 trap, bulk & surface	1.5×10^{8}	$2.1 \times 10^{-17} \pm 1.0 \times 10^{-17}$
2	2 traps, bulk & surface	3.3×10^{8}	$1.3 \times 10^{-13} \pm 6.2 \times 10^{-14}$

To compare the performance of Model 2 to Model 1, the Bayes factor was used, which for this case was calculated to be 6×10^{3} as shown in equation 6.1. This result represents 'decisive' evidence in favour of using Model 2 instead of Model 1.[16,30]

$$BF = \frac{Evidence_2}{Evidence_1} \cdot \frac{P(Model_2)}{P(Model_1)} = \frac{1.3 \times 10^{-13}}{2.1 \times 10^{-17}} \cdot \frac{1}{1} = 6 \times 10^{6} \quad (6.1)$$

Having selected Model 2 as the preferred model, it was next used to extract recombination parameters from the TRPL and PLQE dataset. As the calculations for the posterior distributions were already performed in the same step as the evidence determination, they could be directly plotted and analysed. Figure 6.9 shows the fit lines produced by random sampling from the output posterior distributions of each variable, which highlight that the distribution of fits is quite wide. This is attributed to the Nested Sampling technique used here, which generally resolves the posterior distributions less well than other approaches. A way to improve this in the future would be to add additional samples after the initial run through so-called 'Dynamic Nested Sampling', easily implemented in the 'dynesty' python package already used here.[29,31]

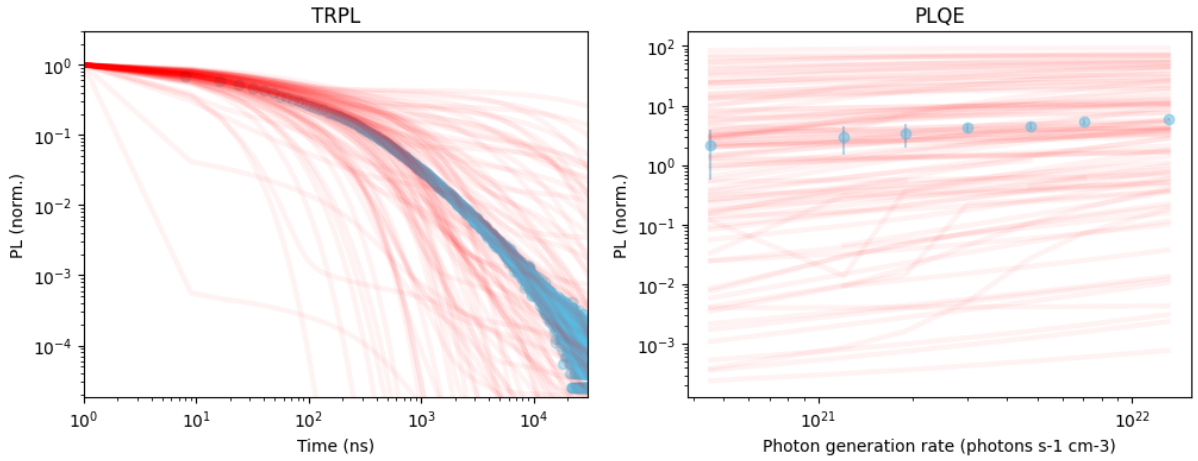


Figure 6.9. Fits for the selected model. 100 sets of parameters are sampled from the posterior distributions and used to generate the fit lines shown in red. Data is shown in light blue.

The output posterior distributions for each free parameter, shown in Figure 6.10, exemplify how Bayesian inference can provide useful additional information. If a posterior distribution is very similar to the prior, this normally suggests that it did not significant affect the fit to the data. In this case, the distributions for the hole trap parameters are significantly narrower, suggesting that this trap had a stronger effect on the shape of the modelled PLQEs and TRPL decays than the electron trap. For some parameters, such as the surface density of electron traps, the fitting was only able to establish an upper boundary for its value. In this case, this is likely because trap density below a certain value no longer significantly affects the modelled PLQE and TRPL.

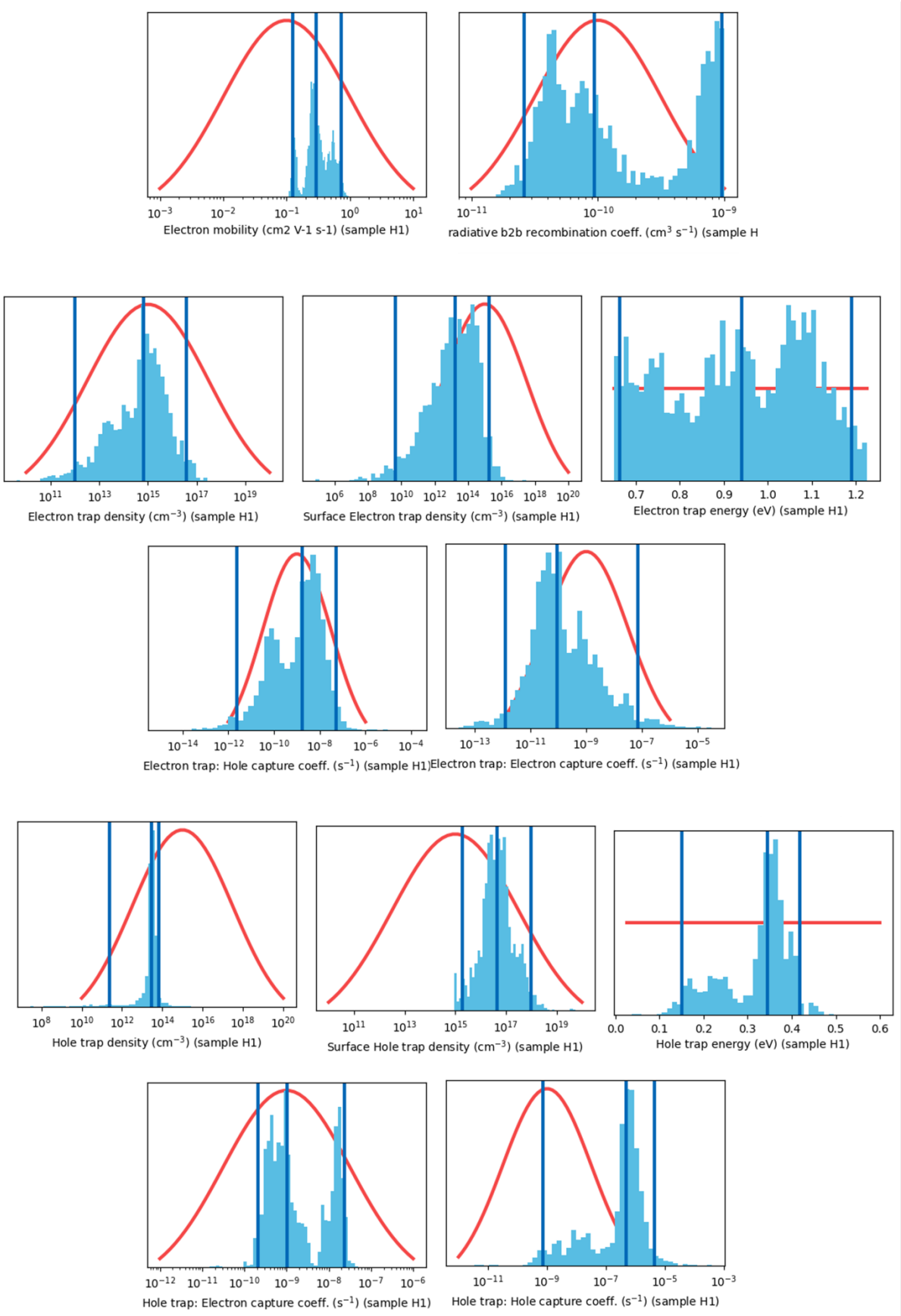


Figure 6.10. Histograms of posteriors calculated by performing nested sampling on the data shown in Figure 6.9 for the selected model. Mean, Q1 and Q3 of the posterior distribution are plotted in dark blue. Prior distributions are shown in red.

Overall, the output posteriors provide useful information about the material. However, further verification, comparison to a larger number of models, and improved resolution of the posterior distributions is necessary to place stronger confidence in the extracted values.

6.5 Conclusion & outlook on modelling recombination in perovskites

In perovskites, recombination kinetics may vary significantly between compositions and material systems. This means that complex models can be necessary to extract information. This chapter used TRPL and PLQE simulations to demonstrate the significance of carefully reassessing the applicability of commonly used models, as a large number of parameters is theoretically able to affect the PLQE and TRPL decays in non-standard ways. Significant evidence was presented to suggest that commonly used recombination models are insufficient to explain the TRPL and PLQE trends currently observed in the lead-tin perovskite samples presented here. The use of an incorrect model may seriously hamper accurate interpretation of these measurements, which is essential to assessing the impacts of modifications such as passivation strategies on material properties. In this chapter, a methodology for quantitative model comparison was applied to determine that when comparing a one- and a two-trap model, a two-trap model more appropriately described the recombination dynamics in the perovskite material presented here.

In this way, this chapter presents a proof of concept of the need for explicit model comparison. To properly prove the suitability of a particular recombination model, many more models containing a more exhaustive list of possible relevant mechanisms should be compared. Such analysis would be further strengthened by application to a wide range of perovskite compositions and including a wider range of characterization techniques (such as TRMC, for example).

Ultimately, the accuracy of extracting parameters through modelling will always be limited by the inability of the model to describe the highly complex 'real' nature of the system. However, the quantitative model comparison demonstrated here is a useful tool to ensure the best possible recombination model (based on the available knowledge and computational resources) is applied. Enabling more correct quantification of recombination parameters in MHPs should help researchers better understand the effects of their interventions on material quality and avoid misinterpretation of data.

6.6 Works Cited

1. Zhang, X., Turiansky, M. E., Shen, J.-X. & Van De Walle, C. G. Defect tolerance in halide perovskites: A first-principles perspective. *Journal of Applied Physics* **131**, 090901 (2022).
2. Lin, R. *et al.* All-perovskite tandem solar cells with improved grain surface passivation. *Nature* **603**, 73–78 (2022).
3. Hu, S. *et al.* Optimized carrier extraction at interfaces for 23.6% efficient tin–lead perovskite solar cells. *Energy Environ. Sci.* **15**, 2096–2107 (2022).
4. Mahmud, M. A. *et al.* Double-Sided Surface Passivation of 3D Perovskite Film for High-Efficiency Mixed-Dimensional Perovskite Solar Cells. *Adv. Funct. Mater.* **30**, 1907962 (2020).
5. Kirchartz, T., Márquez, J. A., Stolterfoht, M. & Unold, T. Photoluminescence-Based Characterization of Halide Perovskites for Photovoltaics. *Adv. Energy Mater.* **10**, 1904134 (2020).
6. de Mello, J. C., Wittmann, H. F. & Friend, R. H. An improved experimental determination of external photoluminescence quantum efficiency. *Adv. Mater.* **9**, 230–232 (1997).
7. Lim, J. *et al.* Long-range charge carrier mobility in metal halide perovskite thin-films and single crystals via transient photo-conductivity. *Nat Commun* **13**, 4201 (2022).
8. Pasanen, H. P. *et al.* Monitoring Charge Carrier Diffusion across a Perovskite Film with Transient Absorption Spectroscopy. *J. Phys. Chem. Lett.* **11**, 445–450 (2020).
9. Savenije, T. J., Guo, D., Caselli, V. M. & Hutter, E. M. Quantifying Charge-Carrier Mobilities and Recombination Rates in Metal Halide Perovskites from Time-Resolved Microwave Photoconductivity Measurements. *Advanced Energy Materials* **10**, 1903788 (2020).
10. deQuilettes, D. W. *et al.* Charge-Carrier Recombination in Halide Perovskites: Focus Review. *Chem. Rev.* **119**, 11007–11019 (2019).

11. Yuan, Y. *et al.* Shallow Defects and Ultralong Photoluminescence Decay Times up to 280 µs in Triple-Cation Perovskites (2023).
12. Taddei, M. *et al.* Interpreting Halide Perovskite Semiconductor Photoluminescence Kinetics. *ACS Energy Lett.* **9**, 2508–2516 (2024).
13. Trimpl, M. J. *et al.* Charge-Carrier Trapping and Radiative Recombination in Metal Halide Perovskite Semiconductors. *Adv Funct Materials* **30**, 2004312 (2020).
14. Kiligaridis, A. *et al.* Are Shockley-Read-Hall and ABC models valid for lead halide perovskites? *Nat Commun* **12**, 3329 (2021).
15. Pan, J. *et al.* Operando dynamics of trapped carriers in perovskite solar cells observed via infrared optical activation spectroscopy. *Nat Commun* **14**, 8000 (2023).
16. Kass, R. E. & Raftery, A. E. Bayes Factors. *Journal of the American Statistical Association* **90**, 773–795 (1995).
17. Krückemeier, L., Liu, Z., Krogmeier, B., Rau, U. & Kirchartz, T. Consistent Interpretation of Electrical and Optical Transients in Halide Perovskite Layers and Solar Cells. *Advanced Energy Materials* **11**, 2102290 (2021).
18. Bisquert, J. Interpretation of the Recombination Lifetime in Halide Perovskite Devices by Correlated Techniques. *J. Phys. Chem. Lett.* **13**, 7320–7335 (2022).
19. Stoumpos, C. C., Malliakas, C. D. & Kanatzidis, M. G. Semiconducting Tin and Lead Iodide Perovskites with Organic Cations: Phase Transitions, High Mobilities, and Near-Infrared Photoluminescent Properties. *Inorg. Chem.* **52**, 9019–9038 (2013).
20. Thiesbrummel, J. *et al.* Universal Current Losses in Perovskite Solar Cells Due to Mobile Ions. *Adv. Energy Mater.* 2101447 (2021) doi:10.1002/aenm.202101447.
21. Savill, K. J. *et al.* Impact of Tin Fluoride Additive on the Properties of Mixed Tin-Lead Iodide Perovskite Semiconductors. *Adv. Funct. Mater.* **30**, 2005594 (2020).
22. Krückemeier, L., Krogmeier, B., Liu, Z., Rau, U. & Kirchartz, T. Understanding Transient Photoluminescence in Halide Perovskite Layer Stacks and Solar Cells. *Advanced Energy Materials* **11**, 2003489 (2021).
23. Huang, K. & Rhys, A. Theory of light absorption and non-radiative transitions in f-centres. *Proceedings of the Royal Society of London. Series A.* **204**, 406–423 (1950).
24. Das, B., Aguilera, I., Rau, U. & Kirchartz, T. What is a deep defect? Combining Shockley-Read-Hall statistics with multiphonon recombination theory. *Phys. Rev. Materials* **4**, 024602 (2020).
25. Mundt, L. E. *et al.* Surface-Activated Corrosion in Tin–Lead Halide Perovskite Solar Cells. *ACS Energy Lett.* **5**, 3344–3351 (2020).
26. Hu, S., Smith, J. A., Snaith, H. J. & Wakamiya, A. Prospects for Tin-Containing Halide Perovskite Photovoltaics. *Precision Chemistry* **1**, 69–82 (2023).
27. Chen, X., Kamat, P. V., Janáky, C. & Samu, G. F. Charge Transfer Kinetics in Halide Perovskites: On the Constraints of Time-Resolved Spectroscopy Measurements. *ACS Energy Lett.* **9**, 3187–3203 (2024).
28. Sergey Koposov *et al.* joshspeagle/dynesty: v2.1.4. Zenodo (2024).
29. Speagle, J. S. dynesty: a dynamic nested sampling package for estimating Bayesian posteriors and evidences. *Monthly Notices of the Royal Astronomical Society* **493**, 3132–3158 (2020).

30. Jeffreys, H. Some Tests of Significance, Treated by the Theory of Probability. *Math. Proc. Camb. Phil. Soc.* **31**, 203–222 (1935).
31. Higson, E., Handley, W., Hobson, M. & Lasenby, A. Dynamic nested sampling: an improved algorithm for parameter estimation and evidence calculation. *Stat Comput* **29**, 891–913 (2019).

7 Outlook

This thesis aimed to further the understanding of the properties of lead-tin perovskite materials by experiment and characterization. A wide range of characterization data was analysed to create a comprehensive understanding of the changes these materials undergo during stressing, or upon the inclusion of extrinsic impurities. This work exemplified that the interpretation and extraction of useful information from material characterization data is rarely straightforward. Simulations proved highly useful in aiding such interpretations, owing to the pre-established understanding of the relevant physics in the studied systems.

Chapter 4 aimed to explain why lead-tin perovskites solar cells rapidly degrade under operating conditions. The investigation revealed that the commonly used PEDOT:PSS HTL causes rapid device degradation by worsening the impact of mobile-ion induced field screening on PCE during aging. The use of an alternative HTL largely mitigates this degradation mode, but uncovers that the reaction between PEDOT:PSS and the perovskite was counteracting a p-doping mechanism which also severely degrades PCE during stressing. The work highlights the need to counteract both of these degradation mechanisms to achieve stable narrow bandgap lead-tin perovskite devices.

In Chapter 5, the effect of the inclusion of small amounts of Bi^{3+} and Sb^{3+} impurities in the lead-tin perovskite material was explored. The impact of such dopants on defect chemistry on the atomic level was predicted by DFT calculations, and the changes in material properties brought about by these changes was experimentally confirmed. The work demonstrated how very small impurity concentrations can strongly affect film quality and proposed a simple pathway to precursor purification.

In Chapter 6, simulations were used to highlight the need for quantitative evaluation of the recombination models used to fit TRPL and PLQE data. It was demonstrated how

Bayesian inference and nested sampling could be used to compare two candidate models. This proof-of-concept model comparison identified a two-trap as the most suitable model for the combined TRPL and PLQE dataset used, which was subsequently used to extract relevant recombination parameters. This chapter demonstrates that it is important to explicitly evaluate the model used for interpreting measurements in each new material system.

The results obtained in this thesis contribute to the fundamental understanding of these material systems, and to the ongoing development of all-perovskite multi-junction photovoltaics.

8 Appendix

A.1 Material parameters used for simulations

Table A.1.1. *IonMonger J-V simulation parameters.*

Parameter	Symbol	Unit	Value	Comment
HTL (PEDOT:PSS)				
Thickness	d	nm	30	From cross-sectional SEM
VB offset	Vb^{HLT}	eV	0.1	near match
Dielectric Permittivity	ϵ_r^{HTL}	-	2.46	[3]
VB density of states	g_{VB}^{HTL}	cm^{-3}	1×10^{20}	[4]
Hole mobility	μ_p^{HTL}	$cm^2\ V^{-1}\ s^{-1}$	1.5×10^{-2}	[5]
Doping density	p_0^{HTL}	cm^{-3}	5×10^{19}	Heavily p-doped[5]
Surface recombination velocity: electrons	S_n^{HTL}	$cm\ s^{-1}$	var	Informed from TRPL, tweaked to fit measured V_{oc}
HTL (PTAA)				
Thickness	d	nm	5	[6]
VB offset	χ^{HLT}	eV	0.1	[7]
Dielectric Permittivity	ϵ_r^{HTL}	-	3.5	[7]
VB density of states	g_{VB}^{HTL}	cm^{-3}	1×10^{20}	[7] Symmetric densities of state
Hole mobility	μ_p^{HTL}	$cm^2\ V^{-1}\ s^{-1}$	4×10^{-5}	[7]
Shallow uniform acceptor density	p_0^{HTL}	cm^{-3}	5×10^{16}	[7] Slightly p-doped
Surface recombination velocity: Electrons	S_n^{HTL}	$cm\ s^{-1}$	var	Informed from TRPL, tweaked to fit measured V_{oc}
Perovskite				
Thickness	d	nm	660	From cross-sectional SEM
Bandgap	E_g^{AL}	eV	1.25	EQE data

Dielectric Permitivity	ϵ_r^{AL}	-	40	[5]
CB effective density of states	g_{CB}^{AL}	cm^{-3}	8.1×10^{18}	[5]
VB density of states	g_{VB}^{AL}	cm^{-3}	5.8×10^{18}	[5]
Electron mobility	μ_e^{AL}	$cm^2\ V^{-1}\ s^{-1}$	3.2	[5] raised slightly to fit data
Hole mobility	μ_p^{AL}	$cm^2\ V^{-1}\ s^{-1}$	3.2	[5] raised slightly to fit data
Lifetime	τ^{AL}	ns	var	Informed from TRPL
ETL (PCBM)				
Thickness	d	nm	20	From cross-sectional SEM
Offset	χ^{ELT}	eV	0.1	
Dielectric Permittivity	ϵ_r^{ETL}	-	5	[8]
CB effective density of states	g_{CB}^{ETL}	cm^{-3}	1×10^{20}	[8]
Electron mobility	μ_e^{ETL}	$cm^2\ V^{-1}\ s^{-1}$	2×10^{-3}	[8]
Shallow uniform donor density	n_0^{ETL}	cm^{-3}	5×10^{16}	[8]
Surface recombination velocity: holes	S_p^{ETL}	$cm\ s^{-1}$	var	Informed from TRPL, tweaked to fit measured V_{oc}

***Table A.1.2**. SCAPS J-V simulation parameters.*

Parameter	**Symbol**	**Unit**	**Value**	**Comment**
HTL (PEDOT:PSS)				
Thickness	d	nm	30	From cross-sectional SEM
Bandgap	E_g^{HTL}	eV	2.6	[2]
Electron Affinity	χ^{HLT}	eV	2.54	Near QFLS = V_{oc} match
Dielectric Permittivity	ϵ_r^{HTL}	-	2.46	[3]
CB effective density of states	g_{CB}^{HTL}	cm^{-3}	1×10^{20}	[4]
VB density of states	g_{VB}^{HTL}	cm^{-3}	1×10^{20}	Symmetric DOS

Electron mobility	μ_e^{HTL}	$cm^2\ V^{-1}\ s^{-1}$	1.5×10^{-2}	[5]
Hole mobility	μ_p^{HTL}	$cm^2\ V^{-1}\ s^{-1}$	1.5×10^{-2}	[5]
Shallow uniform donor density	n_0^{HTL}	cm^{-3}	1×10^{5}	Low value (p-doped)
Shallow uniform acceptor density	p_0^{HTL}	cm^{-3}	5×10^{19}	Heavily p-doped[5]
HTL / Perovskite Interface (PEDOT:PSS)				
Surface recombination velocity: electrons	S_n^{HTL}	$cm\ s^{-1}$	1000	Informed from TRPL, tweaked to fit measured V_{oc}
Surface recombination velocity: Holes	S_p^{HTL}	$cm\ s^{-1}$	1000	Informed from TRPL, tweaked to fit measured V_{oc}
HTL (PTAA)				
Thickness	d	nm	5	[6]
Bandgap	E_g^{HTL}	eV	3	[7]
Electron Affinity	χ^{HLT}	eV	2.14	[7]
Dielectric Permittivity	ϵ_r^{HTL}	-	3.5	[7]
CB effective density of states	g_{CB}^{HTL}	cm^{-3}	1×10^{20}	[7]
VB density of states	g_{VB}^{HTL}	cm^{-3}	1×10^{20}	[7] Symmetric DOS
Electron mobility	μ_e^{HTL}	$cm^2\ V^{-1}\ s^{-1}$	1×10^{-5}	[7]
Hole mobility	μ_p^{HTL}	$cm^2\ V^{-1}\ s^{-1}$	1×10^{-5}	[7]
Shallow uniform donor density	n_0^{HTL}	cm^{-3}	1×10^{5}	Low value (p-doped)
Shallow uniform acceptor density	p_0^{HTL}	cm^{-3}	5×10^{16}	[7] Slightly p-doped
HTL / Perovskite Interface (PTAA)				
Surface recombination velocity: electrons	S_n^{HTL}	$cm\ s^{-1}$	1000	Informed from TRPL, tweaked to fit measured V_{oc}
Surface recombination velocity: Holes	S_p^{HTL}	$cm\ s^{-1}$	1000	Informed from TRPL, tweaked to fit measured V_{oc}
Perovskite				

Thickness	d	nm	660	From cross-sectional SEM
Bandgap	E_g^{AL}	eV	1.25	EQE data
Electron Affinity	χ^{AL}	eV	3.90	[5]
Dielectric Permitivity	ϵ_r^{AL}	-	40	[5]
CB effective density of states	g_{CB}^{AL}	cm^{-3}	2.2×10^{18}	[5]
VB density of states	g_{VB}^{AL}	cm^{-3}	2.2×10^{18}	[5]
Electron mobility	μ_e^{AL}	$cm^2\ V^{-1}\ s^{-1}$	5	[5] raised slightly to fit data
Hole mobility	μ_p^{AL}	$cm^2\ V^{-1}\ s^{-1}$	5	[5] raised slightly to fit data
Shallow uniform donor density	n_0^{AL}	cm^{-3}	1×10^{10}	[5]
Shallow uniform acceptor density	p_0^{AL}	cm^{-3}	1×10^{14}	Measured background carrier density
Neutral defect density lifetime	τ^{AL}	ns	2.5×10^{3}	Informed from TRPL
Single acceptor defect density	T_d^-	cm^{-3}	1×10^{14}	Same density as acceptor density
Electron/hole capture cross section for single acceptor defect	σ_n	cm^{-2}	1×10^{-17}	Tweaked for longer lifetime than neutral defects
Perovskite / ETL Interface				
Surface recombination velocity: electrons	S_n^{ETL}	$cm\ s^{-1}$	1000	Informed from TRPL, tweaked to fit measured V_{oc}
Surface recombination velocity: holes	S_p^{ETL}	$cm\ s^{-1}$	1000	Informed from TRPL, tweaked to fit measured V_{oc}
ETL (PCBM)				
Thickness	d	nm	20	From cross-sectional SEM
Bandgap	E_g^{ETL}	eV	2	[8]
Electron Affinity	χ^{ELT}	eV	3.9	[8]
Dielectric Permittivity	ϵ_r^{ETL}	-	5	[8]
CB effective density of states	g_{CB}^{ETL}	cm^{-3}	1×10^{20}	[8]
VB density of states	g_{VB}^{ETL}	cm^{-3}	1×10^{20}	[8]

Electron mobility	μ_e^{ETL}	$cm^2\ V^{-1}\ s^{-1}$	2×10^{-3}	[8]
Hole mobility	μ_p^{ETL}	$cm^2\ V^{-1}\ s^{-1}$	2×10^{-3}	[8]
Shallow uniform donor density	n_0^{ETL}	cm^{-3}	1×10^5	[8]
Shallow uniform acceptor density	p_0^{ETL}	cm^{-3}	1×10^5	[8]